GFZ
Helmholtz-Zentrum
POTSDAM

Universität Potsdam

Development of geophysical methods to characterize methane hydrate reservoirs on a laboratory scale

Kumulative Dissertation
zur Erlangung des akademischen Grades
"doctor rerum naturalium"
(Dr. rer. nat.)
in der Wissenschaftsdisziplin Geophysik

eingereicht an der
Mathematisch-Naturwissenschaftlichen Fakultät
der Universität Potsdam

von
Mike Priegnitz

Potsdam, November 2015

Published online at the
Institutional Repository of the University of Potsdam:
URN urn:nbn:de:kobv:517-opus4-89321
http://nbn-resolving.de/urn:nbn:de:kobv:517-opus4-89321

Eidesstattliche Erklärung

Hiermit erkläre ich an Eides statt, dass ich die vorliegende Arbeit selbstständig verfasst und keine anderen als die angegebenen Hilfsmittel verwendet habe und die Arbeit in keinem anderen Prüfungsverfahren eingereicht wurde. Die beigelegte digitale Fassung entspricht der vorliegenden schriftlichen Fassung.

Ort, Datum	Mike Priegnitz

A people without knowledge of their past history,
origin and culture
is like a tree without roots

- Marcus Garvey -

List of publications and contributions

Peer-reviewed articles

Spangenberg, E.; Deusner, C.; Schicks, J.; **Priegnitz, M.**; Heeschen, K.; Bigalke, N.; Kossel, E.; Abendroth, S.; Thaler, J.: *Studies on the performance of CH_4-CO_2 hydrate conversion on a laboratory scale* - in preparation.

Spangenberg, E.; Seyberth, K.; Heeschen, K.; **Priegnitz, M.**; Schicks, J.: *A "Quick look" method to assess the dependencies of rock physical sediment properties on the saturation with pore filling hydrate.* - in preparation.

Heeschen, K.; Abendroth, S.; **Priegnitz, M.**; Spangenberg, E.; Thaler, J.; Schicks, J. (2015): *Gas production from methane hydrate - simulating the multistage depressurization test in Mallik, Canada.* - submitted to Environmental Science & Technology.

Priegnitz, M.; Thaler, J.; Spangenberg, E.; Schicks, J.; Schrötter, J.; Abendroth, S. (2015): *Characterizing electrical properties and permeability changes of hydrate bearing sediments using ERT data.* - Geophysical Journal International, 202, 3, p. 1599-1612.

Spangenberg, E.; **Priegnitz, M.**; Heeschen, K.; Schicks, J. (2014): *Are Laboratory-Formed Hydrate-Bearing Systems Analogous to Those in Nature?* - Journal of Chemical and Engineering Data, 60, 2, p. 258-268.

Priegnitz, M.; Thaler, J.; Spangenberg, E.; Rücker, C.; Schicks, J. (2013): *A cylindrical electrical resistivity tomography array for three-dimensional monitoring of hydrate formation and dissociation.* - Review of Scientific Instruments, 84, p. 104502.

Schicks, J.; Spangenberg, E.; Giese, R.; Luzi-Helbing, M.; **Priegnitz, M.**; Beeskow-Strauch, B. (2013): *A Counter-Current Heat-Exchange Reactor for the Thermal Stimulation of Hydrate-Bearing Sediments.* - Energies, 6, 6, p. 3002-3016.

Conference contributions

Priegnitz, M.; Thaler, J.; Spangenberg, E.; Schicks, J.; Abendroth, S. (2015): *Three dimensional monitoring of hydrate formation and dissociation using a cylindrical electrical resistivity tomography array*, PhD-Day, Helmholtz Centre Potsdam GFZ German Research Centre for Geosciences, Germany.

Deusner, C.; Kossel, E.; Bigalke, N.; Schicks, J.; Spangenberg, E.; **Priegnitz, M.**; Heeschen, K.; Abendroth, S.; Thaler, J.; Haeckel, M. (2014): *Hydraulic and Mechanical Effects from Gas Hydrate Conversion and Secondary Gas Hydrate Formation during Injection of CO_2 into CH_4-Hydrate-Bearing Sediments* - Abstracts, AGU 2014 Fall Meeting (San Francisco, USA).

Schicks, J.; Spangenberg, E.; **Priegnitz, M.**; Heeschen, K.; Thaler, J.; Abendroth, S. (2014): *Laboratory investigations on hydrate formation and dissociation in sediments - analogies and differences to natural systems* - Abstracts, AGU 2014 Fall Meeting (San Francisco, USA 2014).

Priegnitz, M.; Spangenberg, E.; Thaler, J.; Schicks, J. (2014): *Three dimensional monitoring of hydrate formation and dissociation using a cylindrical electrical resistivity tomography array* - Proceedings, 8th International Conference on Gas Hydrates (Beijing, China 2014).

Schicks, J.; Spangenberg, E.; Giese, R.; Heeschen, K.; **Priegnitz, M.**; Luzi-Helbing, M.; Thaler, J.; Abendroth, S.; Klump, J.; Kück, J.; Töpfer, M. (2014): *Methane production from hydrate-bearing sediments via thermal stimulation using a countercurrent heat-exchange reactor* - Proceedings, 8th International Conference on Gas Hydrates - ICGH8 (Beijing, China 2014).

Spangenberg, E.; **Priegnitz, M.**; Heeschen, K.; Schicks, J. (2014): *How close are laboratory formed pore-filling hydrate systems to nature?* - Proceedings, 8th International Conference on Gas Hydrates (Beijing, China 2014).

Priegnitz, M.; Thaler, J.; Spangenberg, E.; Schicks, J.; Abendroth, S. (2014): *Spatial resolution of gas hydrate and permeability changes from ERT data in LARS simulating the Mallik gas hydrate production test*, (Geophysical Research Abstracts, Vol. 16, EGU2014-3880, 2014), General Assembly European Geosciences Union (Vienna, Austria 2014).

Heeschen, K.; Spangenberg, E.; Schicks, J.; **Priegnitz, M.**; Giese, R.; Luzi-Helbing, M. (2014): *Simulating the gas hydrate production test at Mallik using the pilot scale pressure reservoir LARS*, (Geophysical Research Abstracts, Vol. 16, EGU2014-3823,

2014), General Assembly European Geosciences Union (Vienna, Austria 2014).

Schicks, J.; Spangenberg, E.; Giese, R.; Heeschen, K.; **Priegnitz, M.**; Luzi-Helbing, M.; Thaler, J.; Abendroth, S.; Klump, J. (2014): *Heat production in depth up to 2500m via in situ combustion of methane using a counter-current heat-exchange reactor*, (Geophysical Research Abstracts, Vol. 16, EGU2014-3790, 2014), General Assembly European Geosciences Union (Vienna, Austria 2014).

Priegnitz, M.; Thaler, J.; Spangenberg, E.; Schicks, J.; Abendroth, S. (2014): *Spatial resolution of gas hydrate and permeability changes from ERT data in LARS simulating the Mallik gas hydrate production test*, PhD-Day, Helmholtz Centre Potsdam GFZ German Research Centre for Geosciences, Germany.

Priegnitz, M.; Spangenberg, E.; Thaler, J.; Schicks, J.; Reichardt, A. (2013): *3D monitoring of hydrate formation and dissociation using a cylindrical ERT*, (Geophysical Research Abstracts Vol. 15, EGU2013-1867, 2013), General Assembly European Geosciences Union (Vienna, Austria 2013).

Beeskow-Strauch, B.; Spangenberg, E.; Schicks, J.; Giese, R.; Luzi-Helbing, M.; **Priegnitz, M.**; Klump, J.; Thaler, J.; Abendroth, S. (2013): *The big fat LARS - a LArge Reservoir Simulator for hydrate formation and gas production*, (Geophysical Research Abstracts Vol. 15, EGU2013-2055, 2013), General Assembly European Geosciences Union (EGU) (Vienna, Austria 2013).

Priegnitz, M.; Spangenberg, E.; Thaler, J.; Schicks, J.; Reichardt, A. (2013): *3D monitoring of hydrate formation and dissociation using a cylindrical ERT*, PhD-Day, Helmholtz Centre Potsdam GFZ German Research Centre for Geosciences, Germany.

Danksagung

Mein erster Dank gilt Dr. Judith Schicks für die Ermöglichung der vorliegenden Arbeit und der guten Betreuung. Immer ein offenes Ohr habend und viel bürokratische Arbeit von mir fern haltend hatte sie sehr großen Anteil daran, dass ich mich stets auf das Wesentliche konzentrieren konnte. Weiterhin danke ich Herrn Prof. Dr. Michael Weber für die Übernahme der Erstgutachterschaft.

Meinen Büromitbewohnerinnen Dr. Manja Luzi-Helbing, Dr. Bettina Beeskow-Strauch und Dr. Katja Heeschen danke ich für die sehr freundliche und hilfsbereite Atmosphäre. Es soll ja Menschen geben, die morgens ungern ins Büro gehen; glücklicherweise zählte ich nicht dazu. I enjoyed!

Für die Hilfe aus seiner kleinen Spa-Oase in sämtlichen Programmier-Belangen danke ich Jan Thaler. Außerdem danke ich Ronny Giese und Alexander Reichardt für die unermüdliche Hilfsbereitschaft und gute Laune, die sie stets versprühten. Selbst wenn mal technische Probleme auftraten, schafften sie es mit einer unvergleichbaren 'Pack-an' Mentalität immer, dass ich mit einem Lächeln im Gesicht zu Werke ging.

Sehr vieles wäre wohl nicht möglich gewesen oder in weniger erfolgreiche Richtungen verlaufen ohne die Hilfe von Dr. Erik Spangenberg. Seine stetige Hilfsbereitschaft, Zugänglichkeit und herzliche Art haben großen Anteil daran, dass schwerwiegende Probleme in den vergangenen Jahren erfolgreich umschifft werden konnten. Ganz großes Dankeschön dafür!

Ich denke, die vergangenen Jahre in der Arbeitsgruppe Gashydrate am GfZ lassen sich am besten mit den Worten "Ist die Zeit schnell vergangen..." beschreiben - geht immer schnell wenn's schön ist...

Zu guter Letzt gilt mein besonderer Dank meiner Familie, deren Rücksicht, Unterstützung und Hilfestellung mir stets den Rücken stärkten.

Zusammenfassung

Gashydrate sind kristalline Feststoffe bestehend aus Wasser und Gasmolekülen. Sie sind stabil bei erhöhten Drücken und niedrigen Temperaturen. Natürliche Hydratvorkommen treten daher an Kontinentalhängen, in Permafrostböden und in tiefen Seen sowie Binnenmeeren auf. Bei der Hydratbildung orientieren sich die Wassermoleküle neu und bilden sogenannte Käfigstrukturen, in die Gas eingelagert werden kann. Aufgrund des hohen Drucks bei der Hydratbildung können große Mengen an Gas in die Hydratstruktur eingebaut werden. Das Volumenverhältnis von Wasser zu Gas kann dabei bis zu 1:172 bei 0°C und Atmosphärendruck betragen. Natürliche Gashydrate enthalten hauptsächlich Methan. Da Methan sowohl ein Treibhausgas als auch ein Brenngas ist, stellen Gashydrate gleichermaßen eine potentielle Energieressource sowie eine mögliche Quelle für Treibhausgase dar.
Diese Arbeit untersucht die physikalischen Eigenschaften von Methanhydrat gesättigten Sedimentproben im Labormaßstab. Dazu wurde ein großer Reservoirsimulator (LARS) mit einer eigens entwickelten elektrischen Widerstandstomographie ausgerüstet, die das erste Mal an hydratgesättigten Sedimentproben unter kontrollierten Temperatur-, Druck-, und Hydratsättigungsbedingungen im Labormaßstab angewendet wurde. Üblicherweise ist der Porenraum von (marinen) Sedimenten mit elektrisch gut leitendem Salzwasser gefüllt. Da Hydrate einen elektrischen Isolator darstellen, ergeben sich große Kontraste hinsichtlich der elektrischen Eigenschaften im Porenraum während der Hydratbildung und -zersetzung. Durch wiederholte Messungen während der Hydraterzeugung ist es möglich die räumliche Widerstandsverteilung in LARS aufzuzeichnen. Diese Daten bilden in der Folge die Grundlage für eine neue Auswerteroutine, welche die räumliche Widerstandsverteilung in die räumliche Verteilung der Hydratsättigung überführt. Dadurch ist es möglich, die sich ändernde Hydratsättigung sowohl räumlich als auch zeitlich hoch aufgelöst während der gesamten Hydraterzeugungsphase zu verfolgen.
Diese Arbeit zeigt, dass die entwickelte Widerstandstomographie eine gute Datenqualität aufwies und selbst geringe Hydratsättigungen innerhalb der Sedimentprobe detektiert werden konnten. Bei der Umrechnung der Widerstandsverteilung in lokale Hydrat-Sättigungswerte wurden die besten Ergebnisse mit dem Archie$_{var-phi}$ Ansatz erzielt, der die zunehmende Hydratphase dem Sedimentgerüst zuschreibt, was einer Abnahme der Porosität gleichkommt. Die Widerstandsmessungen zeigten weiterhin, dass die schnelle Hydraterzeugung im Labor zur Ausbildung von kleinen Hydratkristallen führte, die dazu neigten, zu rekristalliesieren.
Es wurden weiterhin Hydrat-Abbauversuche durchgeführt, bei denen die Hydratphase über Druckerniedrigung in Anlehnung an den 2007/2008 Mallik Feldtest zersetzt wurde. Dabei konnte beobachtet werden, dass die Muster der Gas- und Wasserflussraten im Labor zum Teil gut nachgebildet werden konnten, jedoch auch aufbaubedingte Abweichungen auftraten.
In zwei weiteren Langzeitversuchen wurde die Realisierbarkeit und das Verhalten bei CO_2-CH_4-Hydrat Austauschversuchen in LARS untersucht. Das tomographische Messsystem wurde dabei genutzt um während der CH_4 Hydrat Aufbauphase die Hydratverteilung innerhalb der Sedimentprobe zu überwachen. Im Zuge der anschließenden CO_2-Injektion konnte mithilfe der Widerstandstomographie die sich

ausbreitende CO_2-Front überwacht und der Zeitpunkt des CO_2 Durchbruchs identifiziert werden.

Abstract

Gas hydrates are crystalline solids composed of water and gas molecules. They are stable at elevated pressure and low temperatures. Therefore, natural gas hydrate deposits occur at continental margins, permafrost areas, deep lakes, and deep inland seas. During hydrate formation, the water molecules rearrange to form cavities which host gas molecules. Due to the high pressure during hydrate formation, significant amounts of gas can be stored in hydrate structures. The water-gas ratio hereby can reach up to 1:172 at 0°C and atmospheric pressure. Natural gas hydrates predominantly contain methane. Because methane constitutes both a fuel and a greenhouse gas, gas hydrates are a potential energy resource as well as a potential source for greenhouse gas.

This study investigates the physical properties of methane hydrate bearing sediments on a laboratory scale. To do so, an electrical resistivity tomography (ERT) array was developed and mounted in a large reservoir simulator (LARS). For the first time, the ERT array was applied to hydrate saturated sediment samples under controlled temperature, pressure, and hydrate saturation conditions on a laboratory scale. Typically, the pore space of (marine) sediments is filled with electrically well conductive brine. Because hydrates constitute an electrical isolator, significant contrasts regarding the electrical properties of the pore space emerge during hydrate formation and dissociation. Frequent measurements during hydrate formation experiments permit the recordings of the spatial resistivity distribution inside LARS. Those data sets are used as input for a new data processing routine which transfers the spatial resistivity distribution into the spatial distribution of hydrate saturation. Thus, the changes of local hydrate saturation can be monitored with respect to space and time.

This study shows that the developed tomography yielded good data quality and resolved even small amounts of hydrate saturation inside the sediment sample. The conversion algorithm transforming the spatial resistivity distribution into local hydrate saturation values yielded the best results using the Archie$_{var-phi}$ relation. This approach considers the increasing hydrate phase as part of the sediment frame, metaphorically reducing the sample's porosity. In addition, the tomographical measurements showed that fast lab based hydrate formation processes cause small crystallites to form which tend to recrystallize.

Furthermore, hydrate dissociation experiments via depressurization were conducted in order to mimic the 2007/2008 Mallik field trial. It was observed that some patterns in gas and water flow could be reproduced, even though some setup related limitations arose.

In two additional long-term experiments the feasibility and performance of CO_2-CH_4 hydrate exchange reactions were studied in LARS. The tomographical system was used to monitor the spatial hydrate distribution during the hydrate formation stage. During the subsequent CO_2 injection, the tomographical array allowed to follow the CO_2 migration front inside the sediment sample and helped to identify the CO_2 breakthrough.

Contents

List of Figures

List of Tables

1. Introduction

1.1. Introduction on gas hydrates

Gas hydrates are ice-like crystalline solids composed of a three dimensional network of water molecules enclosing small (< 1 nm) guest molecules [Von Stackelberg et al. 1947].
First evidences on the recognition of gas hydrates date back to 1778, when Joseph Priestly performed experiments featuring water and SO_2 during winter having the window open [Sloan and Koh 2008]. The first documentation of gas hydrates was given by Sir Humphrey Davy in 1810, who performed experiments on the chlorine-water system [Faraday 1859]. The importance of gas hydrate research was boosted by the recognition of the modern natural gas industry who found that ice-like plugs can form in pipelines transporting pressurized natural hydrocarbon gases and constitute a significant danger for safe operation. Hammerschmidt [1934] discovered that those plugs were actually gas hydrates as they formed at temperatures above the freezing point of water. It was from this point that the research on gas hydrate systems moved into the focus of chemists and physicists. In the following decades, much original research has been done on the general composition and on the stability conditions of gas hydrates. It was found that hydrates of natural gases are generally stable at relatively high pressure and low temperature and that gas hydrates can contain several types of gases. In the 1960s the Russian scientist Yuri Makogon was the first to prove the existence of natural gas hydrates in permafrost areas of Siberia [Makogon 1966].

Today it is known that hydrates can form as long as all of the following requirements are fulfilled:

- presence of sufficient amounts of water,
- presence of sufficient amounts of gas,
- low temperatures,
- elevated pressure.

Under the stated conditions, the water molecules align in regular orientations and form cavities. Five different kind of cavities can be found in nature (Fig. 1.1): the pentagonal dodecahedron (5^{12}), the tetrakaidecahedron ($5^{12}6^2$), the hexakaidecahedron ($5^{12}6^4$), the irregular dodecahedron ($4^3 5^6 6^3$), and the icosahedron ($5^{12}6^8$) [Sloan and Koh 2008]. Those cavities (also referred to as *host*) get stabilized when they are filled with gas molecules, which shield attractive forces between the water molecules [Tse et al. 1993]. In naturally occurring gas hydrates those gas molecules

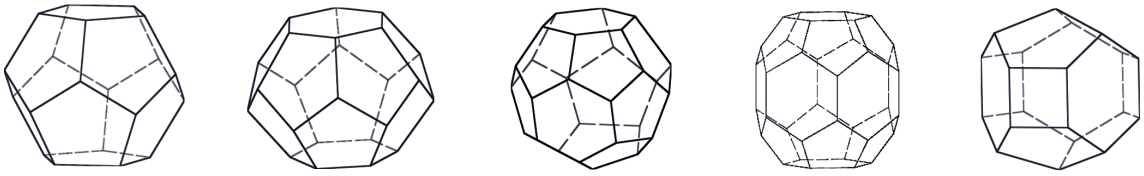

Figure 1.1.: Naturally occuring hydrate cavities: pentagonal dodecahedron (5^{12}), tetrakaidecahedron ($5^{12}6^2$), hexakaidecahedron ($5^{12}6^4$), icosahedron ($5^{12}6^8$), and irregular dodecahedron ($4^35^66^3$). Adapted from Luzi [2012].

(also referred to as *guest*) are mainly methane (CH_4), but higher hydrocarbons, carbon dioxide (CO_2), hydrogen sulfide (H_2S), and mixed gas hydrates can be found as well [Milkov et al. 2005]. Because the water lattice completely encloses the guest molecules, gas hydrates belong to the class of inclusion compounds or clathrates. Depending on the guest molecules, the formed cavities arrange in unit cells creating different crystal structures. So far, three different kinds of crystal structures were identified in natural hydrates: cubic structure one (sI, composed of 2 x 5^{12} and 6 x $5^{12}6^2$ cages), cubic structure two (sII, composed of 16 x 5^{12} and 8 x $5^{12}6^4$ cages), and hexagonal structure H (sH, composed of 3 x 5^{12}, 2 x $4^35^66^3$, and 1 x $5^{12}6^8$ cages) [McMullan and Jeffrey 1965; Mak and McMullan 1965; Ripmeester et al. 1987]. The type of structure formed depends primarily on the size of the guest molecule; i.e. methane fits into both the small and large cages of sI, whereas propane is too large to fit into the large cage of sI but can fit into the large cage of sII and therefore forms sII [Koh et al. 2011]. However, several large guest molecules can only be incorporated in sII and sH hydrate structures in the presence of a so called help-gas (e.g. CH_4) to stabilize the 5^{12} and $4^35^66^3$ cages [Giavarini and Hester 2011]. The most common guest molecules in nature and the corresponding hydrate structures are presented in Tab. 1.1.

Table 1.1.: Guest molecules commonly found in gas hydrates

Guest Molecules	Structural Formula	Hydrate Structure	Utilized Cavities
Methane	CH_4	sI	5^{12} and $5^{12}6^2$
Ethane	C_2H_6	sI	$5^{12}6^2$
Propane	C_3H_8	sII	$5^{12}6^4$
Butane[1]	C_4H_{10}	sII	$5^{12}6^4$
Methylcyclohexane	C_7H_{14}	sH	$5^{12}6^8$
Carbon Dioxide	CO_2	sI	5^{12} and $5^{12}6^2$
Hydrogen Sulfide	H_2S	sI	5^{12} and $5^{12}6^2$

[1] iso-butane and n-butan

Furthermore, the composition of mixed gas hydrates has a significant influence on the thermodynamic stability of gas hydrates. Compared to pure methane hydrate, the increasing concentration of higher hydrocarbons, carbon dioxide or hydrogen sulfide shifts the hydrate stability towards higher temperatures and lower pressures (Fig. 1.2).
Considering the clathrate geometry, enormous amounts of gas can be stored in hydrate structures. For a structure I methane hydrate, 1 m^3 of hydrate can contain up to 172 m^3 of free CH_4 gas at 0°C and atmospheric pressure [Kvenvolden 1993].

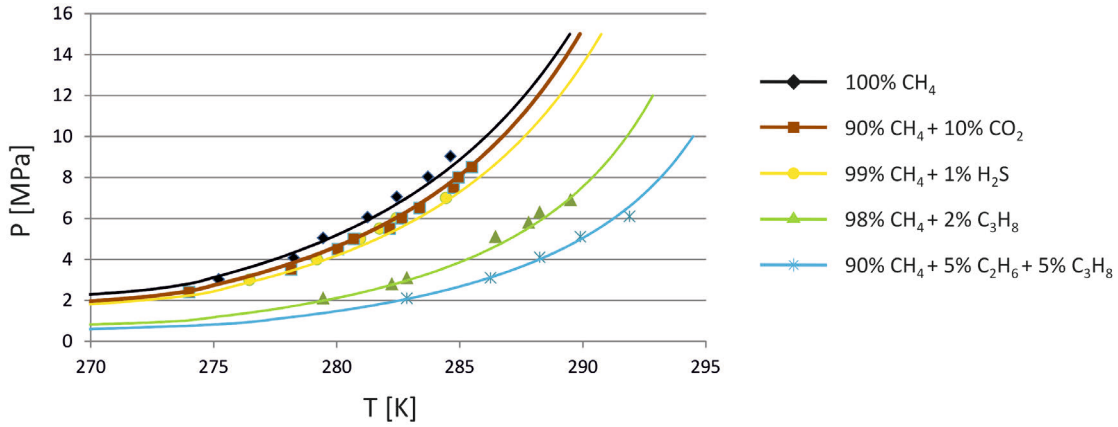

Figure 1.2.: Hydrate stability curves for different guest molecule compositions. Higher hydrocarbons, carbon dioxide, and hydrogen sulfide shift the stability curve to lower pressures or higher temperatures, respectively. Solid lines are modelled stability curves using CSMGem, symbols represent experimental data from Schicks and Luzi-Helbing [2015].

However, the crystallization process of hydrate formation is generally described as a two stage process (e.g. Max et al. [2006]):

1. Nucleation, the actual production of a solid material
2. Particle growth, which enlarges the formed solid crystals

The process of hydrate nucleation is a microscopic phenomenon and difficult to observe experimentally [Sloan and Koh 2008]. Two conceptual models of methane hydrate nucleation can be found describing hydrate nucleation from the liquid phase [Sloan and Koh 2008]. The *labile cluster* hypothesis of Christiansen and Sloan [1994] bases on the assumption of pure water existing without guest molecules but already including water molecules aligned to labile ring structures of pentamers and hexamers. As soon as guest molecules are dissolved in water, those ring structures start to form labile cluster around the guest molecules. Those cluster structures are considered to provide an early stage hydrate cage. Subsequently, the clusters agglomerate by sharing faces until they reach a critical size to permit crystall growth to initiate. On the contrary, the *nucleation at the interface* hypothesis of Kvamme [1996] suggests hydrate nucleation to be controlled by guest molecules in a vapour phase. Guest molecules adsorb on the water surface and get incorporated in firstly

partial, later complete hydrate cages. Additional clusters join until a critical size is achieved to permit crystal growth to initiate.
Subsequent to the successful formation of a solid hydrate nuclei, hydrate growth continues to increase the amount of formed hydrate. The process of hydrate growth is mainly controlled by the intrinsic growth kinetics, limitations due to mass transfer, and limitations due to heat transfer [Sloan and Koh 2008].

Once a solid hydrate structure is formed, it will remain stable as long as it is in thermal, mechanical, and chemical equilibrium with the environment. Disturbing only one of those three equilibria will immediately cause hydrate decomposition to initiate. The economic production of CH_4 is the main target for industrial hydrate research. Hence, the mechanisms required for safe and economic hydrate dissociation became of greater interest in the past two decades. A lot of efforts were made to identify proper dissociation techniques and to finally test them in a small number of field studies:

Thermal stimulation aims at disturbing the thermal equilibrium by rising the formation temperature above the stability temperature of the solid hydrate phase. The required heat to warm up the hydrate bearing sediment layer is provided by either injecting hot fluids into the borehole or by *in-situ* combustion. The injection of hot fluids was tested in the Mallik 2002 gas hydrate production research well program in the Mackenzie Delta, Canada [Dallimore et al. 2005]. Following the idea that a significant amount of heat was getting lost in the borehole on the way to the target layer, Schicks et al. [2011, 2013] developed a counter-current heat-exchange reactor to produce heat *in-situ* in the target zone.

Depressurization aims at reducing the reservoir pressure below the hydrate stability pressure to disturb the mechanical equilibrium. By placing a pump into the borehole and continuously producing formation fluids, the reservoir pressure can be decreased to initiate hydrate dissociation. This technique was tested on a field scale during the Mallik 2007/2008 research program [Wright et al. 2011b] as well as offshore Japan in a marine setting in 2013 [Yamamoto 2014].

Chemical stimulation aims at disturbing the chemical equilibrium by offering other guest molecules or by adding chemicals which shift the stability of gas hydrates. The most prominent example of guest molecule substitution is the idea of replacing hydrate bonded methane gas by carbon dioxide in order to sequestrate CO_2. A field trial was realized in 2012 at the Alaska North Slope to investigate the performance of the exchange reaction where a mixture of carbon dioxide and nitrogen was injected into a methane hydrate bearing formation [Lee and White 2014].

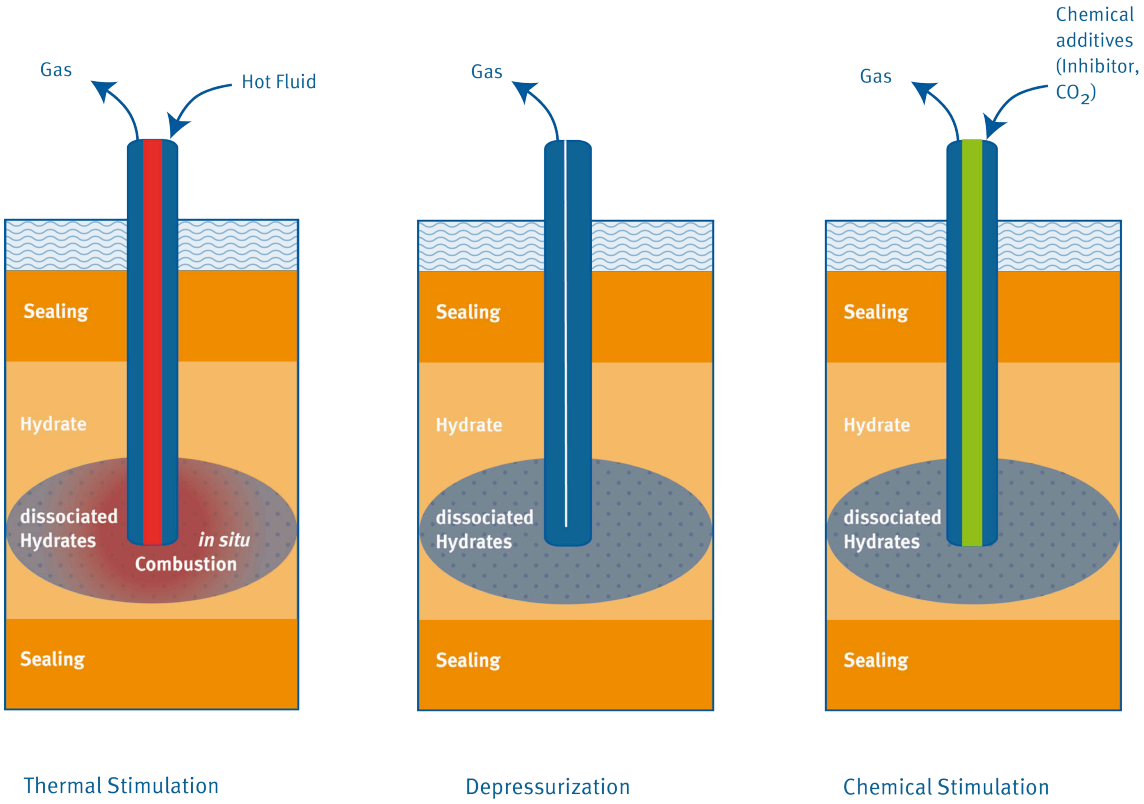

Figure 1.3.: The three basic techniques to disturb the equilibrium state of gas hydrate and initiate hydrate decomposition.

1.2. Natural gas hydrates and their global significance

Natural hydrate reservoirs

Natural gas hydrates occur in the subsurface, where the four requirements for hydrate formation are fulfilled. The pressure in the subsurface is provided by the overlaying geological layers (overburden) and increases with increasing depth. In the same manner the temperature increases with increasing depth, following a site specific geothermal gradient. The changes of pressure (P) and temperature (T) in the underground can create a window of PT conditions that permits hydrate formation in the subsurface. This PT window is often referred to as the gas hydrate stability zone (GHSZ).
Today it is known that many areas provide temperature and pressure conditions allowing for hydrate formation, but do not contain any hydrates at all. In most cases the reason is an insufficient gas supply [Giavarini and Hester 2011]. Methane trapped in natural gas hydrates is either of thermogenic or biogenic origin. Thermogenic gas is formed deep in the earth in the process of catagenesis [Giavarini and Hester 2011]. While they are not typical in hydrates, thermogenic gases are

more common in conventional natural gas reservoirs. The process of catagenesis is characterized by high temperatures (>450 K), producing relatively large amounts of ethane and higher hydrocarbons [Sloan and Koh 2008]. Because the required high temperatures correspond to large depths (>1000 m), thermogenic methane is not produced in the GHSZ. Due to diagenesis, compaction, and buoyancy, methane of thermogenic origin migrates upwards until it enters geological layers which provide temperature and pressure conditions allowing methane hydrates to form.
However, the methane in gas hydrates is dominantly generated by bacterial anaerobic degradation of organic matter in low-oxygen environments [Demirbas 2010], also referred to as biogenic methane production. Biogenic methane production in marine settings occurs in depths of tens to 1000 m below the seafloor [Sloan and Koh 2008]. Because the depth of biogenic methane production is comparably low, biogenic methane can be generated *in-situ* (in the GHSZ) and directly be consumed in hydrate formation.
As long as methane is not biogenically formed *in-situ*, it compulsorily has to migrate upwards until it enters the GHSZ to form hydrate. Depending on the methane concentration, methane can migrate either as a free gas phase (bubbles) or dissolved in the pore water. However, it is assumed that only hydrate formation close to faults (which act as pathways for fluids) and at the base of the GHSZ is driven by the presence of free gas [Waite et al. 2009]. The more common process of hydrate formation in sediments is rather assumed to utilize dissolved, aqueous phase methane [Buffett and Zatsepina 2000; Waite et al. 2009]. In that case, gas hydrate can only accumulate if the mass fraction of methane remains in excess to the local methane solubility when the methane-loaded water migrates through the sediment [Xu and Ruppel 1999].
On a global scale, the conditions required to allow for hydrate formation are fulfilled in marine sediments at active and passive continental margins, in permafrost areas, in deep inland seas, and in deep lakes [Sloan and Koh 2008]. Fig. 1.4 emphasizes the distribution of proven and inferred gas hydrate reservoirs.

It is unknown how much methane is globally bonded in hydrates. Over the last decades, numerous estimates tried to evaluate the global gas hydrate inventory. Milkov [2004] gave a great review of published estimates showing that the estimates varied be several orders of magnitude. The strong deviations among the different estimates arise from the different approaches and data each estimate is based on. The early estimates were derived from the assumptions of a homogeneous hydrate distribution, hydrate saturation, and sediment porosity with hydrate being present wherever the stability conditions of CH_4 hydrate were given (e.g. Trofimuk et al. [1973]: $\approx$3053 x 10^{15} m^3). Recent estimates rather base on complex models considering thermodynamical, biochemical, and geophysical data to reflect the current state of the art of gas hydrate research (e.g. Piñero et al. [2013]: $\approx$0.8 x 10^{15} m^3).

Environmental aspects of gas hydrates

Generally, gas hydrate deposits have to be considered as a vulnerable hydrocarbon reservoir because they are sensitive to temperature, pressure, and salinity changes.

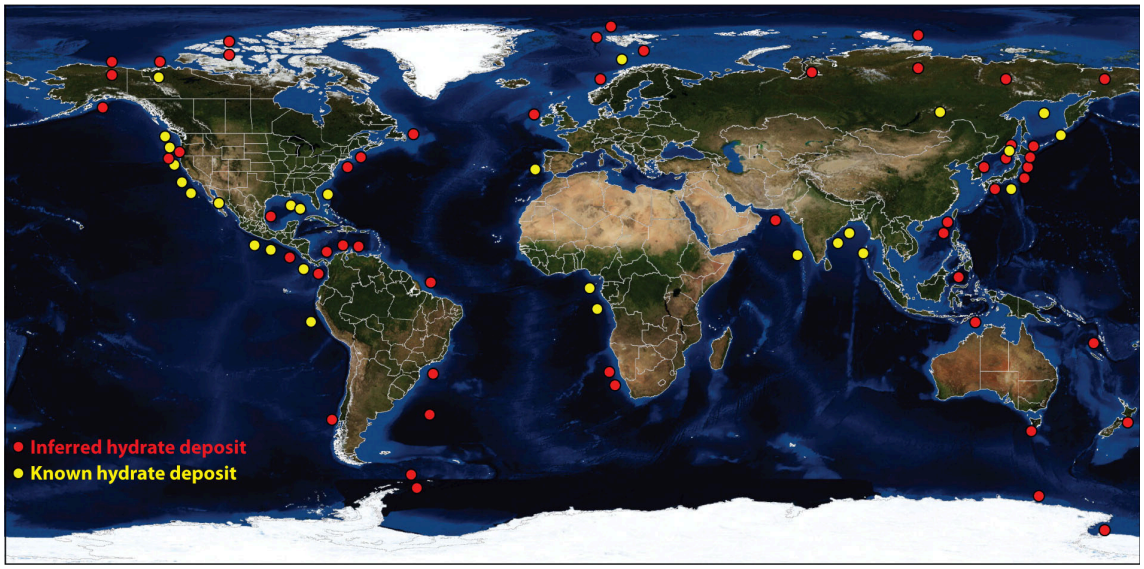

Figure 1.4.: The global distribution of recovered and inferred gas hydrate deposits (from: Hester and Brewer [2009]). Hydrate deposits can be clustered in marine reservoirs, permafrost reservoirs, and deep inland sea reservoirs.

In that context, the issue of slope failure related to gas hydrate systems in marine scenarios is one major topic of current gas hydrate research. The ongoing process of global warming can increase the ocean bottom temperature of specific areas in the future [Purkey and Johnson 2010], possibly shifting the GHSZ. In the context of paleo climate changes, small changes in the ocean bottom temperature shifted the gas hydrate stability zone (GHSZ) by several meters, causing severe methane release. At the end of the Paleocene up to 2 trillion tons of carbon were released into the atmosphere over 10.000 years. During that time, the ocean bottom temperature increased by 6°C, promoting further hydrate decomposition [Schweizer et al. 2007]. When it comes to the economic production of natural gas from hydrates, the decomposition of the solid hydrate phase is required. Especially in marine environments, where hydrates are commonly stable in unconsolidated sediment layers, removing a solid phase from the sediment's pore space may weaken the mechanical strength of the respective geological layer. Because marine gas hydrate deposits typically occur at continental margins, uncontrolled hydrate decomposition may cause slope failure, possibly leading to tsunamis. One the largest submarine mass flows, the Storegga slide offshore Norway, is strongly associated with the presence of gas hydrates and might have been caused by uncontrolled hydrate dissociation due to paleo-climate changes [Bünz et al. 2003; Mienert et al. 2005].
Yet another important fact is that methane is the second most important greenhouse gas after carbon dioxide (CO_2). According to the 2014 IPCC report, methane contributed 16% to the overall anthropogenic greenhouse gas emissions (7.8 ± 1.6 $GtCO_2$ eq/yr) in 2010 [Blanco et al. 2014]. In 2011, the total amount of atmospheric methane was 1803.2 ppb [Hartmann et al. 2013]. Although significant amounts of methane are assumed to be bound in hydrates, much methane from naturally dis-

sociated gas hydrate may never reach the atmosphere. It rather may be converted to carbon dioxide and sequestered by the hydro- and biosphere in the water column before reaching the atmosphere [Kvenvolden 1999]. The current main emissions of methane are mainly due to a wide range of anthropogenic activities such as the production and transport of fossil fuels, livestock, and rice cultivation, and the decay of organic waste in solid waste landfills [Blanco et al. 2014].

Hydrates as an energy resource

Ensuring continuous and safe flow in hydrocarbon streamlines (also referred to as *flow assurance*) was the major driving force for industrial gas hydrate research over the past decades. Ever since the amounts of methane bound in hydrates were perceived, the idea of recovering natural gas from hydrates became another aspect of industrial interest in gas hydrate deposits. With respect to the growing energy demand worldwide, gas hydrate deposits have become of increasing interest for various countries in the past decades. Demirbas [2010] even states that methane hydrates, together with renewable energy and hydrogen, are the most important alternative energy resources for the near future. Even though the primary product of gas hydrate production would be natural gas (mainly methane), which is a well known material in conventional oil and gas industry for many years, the economic development of gas hydrate deposits still raises fundamental questions.
From a natural gas market point of view, the landscape of availability and pricing of natural gas is a very dynamic system. The most prominent example is given by the United States of America and Canada. Importing natural gas for a long time, the exploitation and production of shale gas beginning in 2009 started to have a huge impact on the gas price in North America and the increased availability is about to make former import countries exporting countries of natural gas [Makholm 2015]. Due to the increased availability in North America, gas prices consequently "fell to much lower levels than had previously been thought possible" [Stern 2014] by 13.6% from 2009 to 2013 in the U.S., whereas prices in Europe doubled up from 5.00 USD to 10.55 USD in that timespan [Makholm 2015].
This example emphasizes that the exploitation of new or unconventional resources can significantly affect global markets as well as a single country's economy. For that reason, the countries pushing gas hydrate research today are mainly countries which have a vast energy demand, cannot access conventional hydrocarbon reservoirs on their own territories, and strongly rely on imports. The large amounts of hydrocarbons stored in gas hydrates, thus, constitute a very attractive potential resource.
Walsh et al. [2009] investigated the economic viability of gas production from natural hydrates and concluded that gas prices of 7.50 - 12.00 $CDN/Mscf would be required to make the production process economically efficient. However, those prices only give a rough impression and strongly depend on the hydrate reservoir type, the geological setting, additional infrastructure, and many more.
The greatest uncertainties evaluating gas hydrate reservoirs arise from unknown hydrate distribution and saturation. To evaluate the economic feasibility of a hydrate

reservoir, it is crucial to know how much hydrate is in there, how it is distributed, and how much can be produced. Those questions can only be answered having a tremendous understanding of the reservoir geology and its thermodynamic and physical properties.

1.3. Physical properties of hydrate bearing sediments

The presence of gas hydrate in the pore space of any geological layer can have a significant impact on its physical properties. The most affected physical properties are the electrical conductivity, seismic velocities, and the hydraulic permeability (e.g. Waite et al. [2009]; Shankar and Riedel [2011]).
The electrical conductivity σ, or its inverse electrical resistivity ρ, are commonly used parameters to characterize electrical charge transport within a given medium. Because most rock forming minerals are classed as insulators, the charge transport in natural sediments and rocks is predominantly provided by conductive pore water and a result of electrolytical conduction. To link the electrical properties of the rock with the electrical properties of the pore fill, the formation resistivity factor F is frequently used:

$$F = \frac{\rho_0}{\rho_w}, \tag{1.1}$$

where ρ_0 is the electrical resistivity of the water saturated rock and ρ_w is the electrical resistivity of the pore water.
The seismic velocities relate the elastic properties of a material to its density in terms of the speed of elastic waves passing through a body of that material. Two types of body waves can be distinguished: compressional (also referred to as P) and shear (also referred to as S) waves. Their propagation velocities V_p and V_s are related with the compressional modulus K, the shear modulus μ and the density ρ of the material as follows [Kirsch 2008]:

$$V_p = \sqrt{\frac{K + \frac{4}{3}\mu}{\rho}} \qquad\qquad V_s = \sqrt{\frac{\mu}{\rho}} \tag{1.2}$$

The seismic velocities are a common tool to classify materials or to assess properties of the pore fill.
The permeability characterizes the ability of a material to allow fluids to flow [Schön 2004]. The higher the permeability of a given medium, the easier a fluid can flow through that material. A detailed description of the relevant petrophysical parameters is given in the appendix (A).

Those properties are sensitive to the presence of gas hydrate because the solid hydrate phase constitutes an electrical insulator, can clog pore throats, and stiffens the host sediment, increasing the seismic velocities [Waite et al. 2009]. To what extent the physical properties are affected, depends on the amount and the distribution of hydrate within the sediment's pore space (also referred to as *growth habit*). In order to analyse the mentioned properties, four different types of growth habits have to be taken into account (see Fig. 1.5):

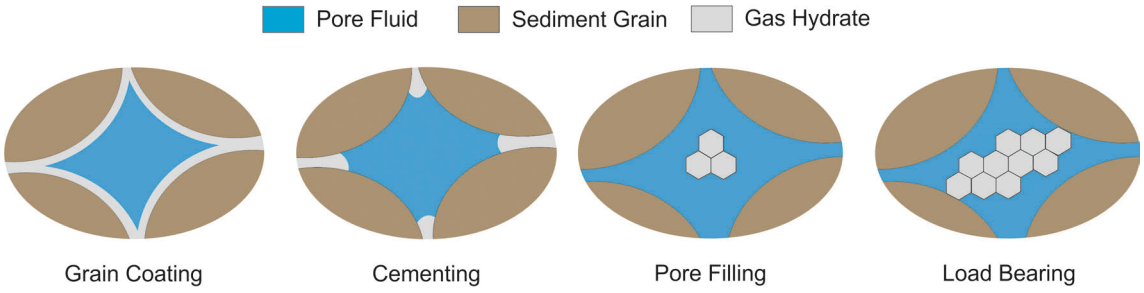

Figure 1.5.: The four different types of gas hydrate growth habits.

Pore Filling In a fully water saturated pore space, pore filling hydrates form from methane dissolved in water in the center of the pores without any contact to surrounding sediment grains. The solid hydrate phase is considered to be a part of the pore fill. The seismic velocities and the electrical resistivity only increase gradually with increasing hydrate saturation [Helgerud et al. 1999; Spangenberg and Kulenkampff 2006], whereas the permeability decreases [Kleinberg et al. 2003]. The interconnectivity of the pore space remains maintained.

Load Bearing As hydrate saturation increases, measurements of electric resistivity and seismic velocities indicate that pore filling hydrate transforms into frame building/load bearing hydrate for pore space saturations above 40% [Spangenberg and Kulenkampff 2006; Priest et al. 2009]. As the formed hydrate cluster grows, it will adjoin the surrounding sediment grains and increase the mechanical strength of the sediment layer. Hydrates are considered to be part of the sediment matrix, increasing the seismic velocities much steeper compared to the pore filling growth habit [Helgerud et al. 1999]. In the same manner, the interconnectivity of the pore space is getting decreased with increasing hydrate saturation, resulting in decreasing electric conductivity and hydraulic permeability.

Grain Coating Grain coating hydrate forms in sediments which are not completely water saturated. The required water phase is only provided by wetting water directly attached to the sediment grains. For initial water saturations less than ≈35%, hydrate tends to

form a shell around the grains which can clog pore throats and subsequently can cut of parts of the pore space from the interconnected pore network [Kumar et al. 2010]. With increasing grain coating hydrate saturation, the seismic velocities will quickly increase because the solid hydrate phase strengthens the hydrate bearing formation [Waite et al. 2009]. Grain coating hydrate decreases the hydraulic permeability - but to a lesser extent than for pore filling growth habits because larger flow paths exist in grain-coating hydrate [Dai et al. 2012]. The similar behaviour can be observed for the electrical resistivity, which increases with increasing grain coating hydrate saturation, but not as intensive as for pore filling hydrate [Spangenberg 2001].

Cementing

Cementing hydrate forms directly at grain contacts. Similar to grain coating hydrate the required water phase is provided by wetting water at sediment grains in the non-fully water saturated pore space. Already small degrees of cementing hydrate saturation significantly stiffen the sediment strength and rapidly increase the seismic velocities [Dai et al. 2012]. Being a special case of grain coating hydrate, cementing hydrate also decreases the hydraulic permeability and the electrical conductivity but to a lesser extent compared to pore filling hydrate.

Fig. 1.6 emphasizes how severe the physical properties of hydrate bearing sediments can change for the very same sediment and degree of hydrate saturation, but for different types of growth habits.

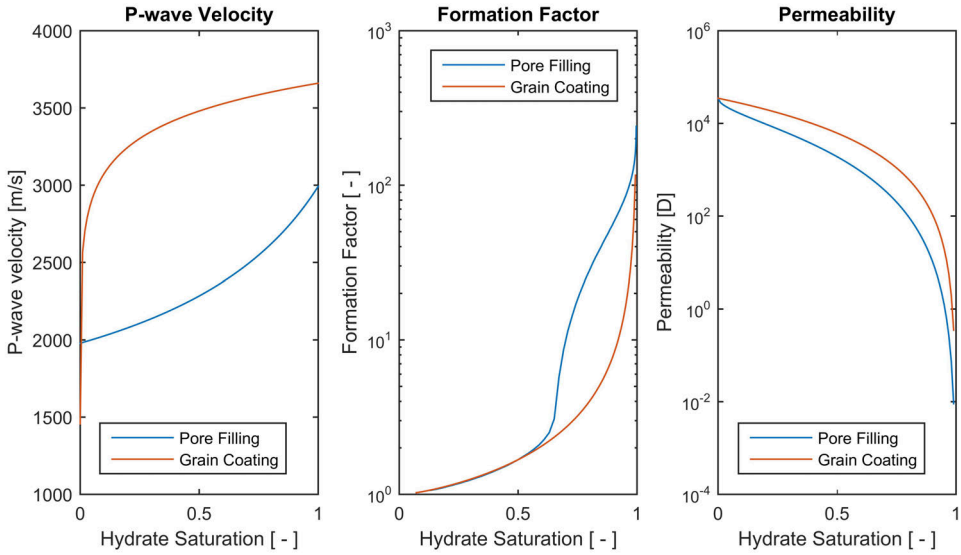

Figure 1.6.: Modelled changes of physical properties for different growth habits[2].

[2]P-wave velocities modelled after Dvorkin and Nur [1996] and Helgerud et al. [1999]; formation factor modelled after Spangenberg [2001]; permeability modelled after Kleinberg et al. [2003].

Because most gas hydrate deposits are linked to recent or paleo marine settings, it is commonly assumed that hydrate formation predominantly takes place in fully water saturated environments. Hence, the majority of naturally formed hydrates are considered to initially form pore filling hydrate [Buffett and Zatsepina 2000].

On a field scale, the changes of the seismic and electrical properties caused by the presence of gas hydrates are commonly used to explore and map gas hydrate deposits. The transition from sediments containing water and free gas to sediments containing water and hydrates is accompanied by a strong (negative) impedance contrast which causes significant seismic reflections (e.g. Berndt et al. [2004]). Those seismic reflections typically cross-cut sedimentary strata and follow the topography of the sea floor, which is why they are referred to as bottom simulating reflectors (BSR). Today a lot of efforts are made to deploy ship-based seismic surveys in order to explore and map gas hydrate deposits. Similar to seismic surveys, electric surveys can be deployed in order to identify high resistivity areas caused by the presence of electrically isolating gas hydrates (e.g. Schwalenberg et al. [2010]). It is important to realize that those remote sensing methods are extremely useful to identify and map gas hydrate deposits, but fail to provide volumetric estimates of the hydrate phase in the pore space.

Table 1.2.: Seismic and electrical properties of materials commonly considererd in gas hydrate reservoirs.

Material	P-Wave velocity [m/s]	S-Wave velocity [m/s]	Density [kg/m^3]	Resisitivity [Ωm]
Methane Gas	412[a]	0[a]	90[a]	$\rightarrow \infty$
Brine	1412[b]	0[b]	1005.1[b]	3.77[b]
Quartz	6040[c]	4120[c]	2650[c]	2x10^{14} [d]
Methane Hydrate (sI)	3766[e]	1957[e]	925[e]	≈2x10^{4}[f]
Ice	3769[e]	1942[e]	916.7[g]	≈4x10^{3}[f]

To investigate the physical properties of gas hydrate reservoirs on a laboratory scale, studies are commonly kept simple by considering one homogeneous sediment material. The most favoured sediment type is medium to coarse (quartz) sand because this type of sediment is highly permeable and considered to permit the most promising gas production rates in the case of economic gas production from hydrate bearing

[a]Data from Waite et al. [2009]
[b]Calculated for a Salinity of 3 wt% at 0°C and 0.1 MPa. Calculation after Mavko et al. [2003]
[c]Data from Helgerud et al. [1999]
[d]Data from Schön [2004]
[e]Calculated at 0°C and 0.1 MPa after Helgerud et al. [2009]
[f]Data from Du Frane et al. [2011]
[g]Data from Barrett [2003]

sediments. Table 1.2 presents the mechanical and electrical properties of the constituents in frequently considered quartz sand gas hydrate reservoir.

The different materials cover a wide range of each physical property. The huge contrasts among those properties allows to physically follow the process of both hydrate formation and dissociation. An example evolution for the changes of the electrical resistivity in marine environments is shown in Fig. 1.7. Initially, the sediment's

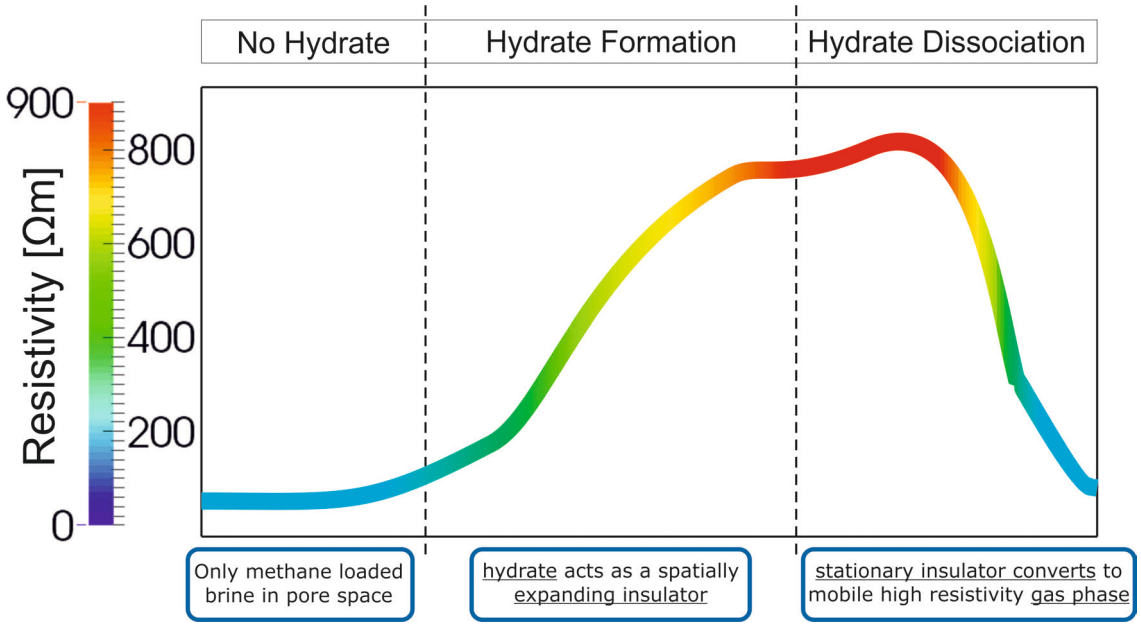

Figure 1.7.: Schematic resistivity evolution during hydrate formation from methane dissolved in brine and hydrate dissociation.

pore space is exclusively filled with methane loaded brine, which constitutes a very good electrical conductor. Hydrates act as an electrical insulator. Thus, increasing hydrate saturation during hydrate formation increases the electrical resistivity in the pore space.
Due to hydrate decomposition, free gas is released acting as an additional electrical insulator. The released gas phase expands into the pore network following the local pressure gradients and pushing well conductive pore water out of the pores. Subsequently, the onset of hydrate dissociation is marked by a small resistivity increase until the produced gas is replaced by well conductive pore water, decreasing the resistivity again. Because the elastic and seismic properties of the reservoir constituents show similar contrasts, seismic methods are frequently used to follow hydrate formation and dissociation experiments, as well.

For experimental purposes, it is important to realize that the general process of hydrate nucleation has to be understood as a stochastic process [Sloan and Koh 2008]. On a time scale, an induction period is frequently observed. During this period, the PT conditions are already within the stability field of gas hydrate, but no hydrate nucleation is observed. This time of metastability is suggested to be required by the

liquid and gas phases to organize themselves into orderly solid hydrate structures [Lederhos et al. 1996]. The site of hydrate nucleation might be determined more deterministic as long as hydrate formation is initiated in a multiphase (vapour-liquid, liquid-liquid) environment. In such settings hydrate nucleation initiates at the phase interface [Long and Sloan 1996].
Yet another important factor affecting hydrate formation is the type of sediment. Whereas it is assumed that the sediment mineralogy and surface texture only play a minor role, the grain and pore size distribution appear to be of increased importance for hydrate formation [Uchida et al. 2004]. The studies of Torres et al. [2008] and Sun et al. [2014] conclude that hydrate preferentially forms in coarse-grained sediments with large pores because the lower capillary pressures support hydrate nucleation and mass transport. On the contrary, Heeschen et al. [2014] report to increase the success rate of small scale hydrate formation experiments by decreasing the sediments grain size. Kang et al. [2009] therefore suggest that there is an optimum point of grain and pore diameter for the rate of hydrate formation.
However, for natural hydrate deposits which are supplied by methane dissolved in water, the site of initial hydrate nucleation is stochastic. The ability to predict where hydrate formation initiates and what the growth habit will be like is of eminent importance when it comes to the design of experimental setups to investigate the properties of gas hydrate bearing materials properly.

1.4. Structure and scope of this thesis

No matter whether gas hydrates are considered as a potential energy resource, a trigger for geo-hazards, or as a source of greenhouse gases, it is crucial to answer the question how much and where hydrate is located in any kind of reservoir. In that context, the main emphasis of this work is laid on the physical properties of hydrate bearing, sedimentary layers. In particular, the electrical, mechanical, and hydraulic properties of hydrate bearing sediments were studied on a laboratory scale. To do so, numerous experiments were carried out to investigate the physical properties of hydrate bearing sediment samples mimicking naturally occurring, marine hydrate deposits. A major focus in all experiments was laid on the technique of hydrate formation. The LArge Reservoir Simulator (LARS, [Schicks et al. 2011, 2013; Priegnitz et al. 2013]) was the primary experimental setup used throughout this thesis. The LARS setup hosts a 210 litre sediment sample, which was circulated with methane loaded brine. As reported by Spangenberg et al. [2005] hydrate formation will be initiated by migrating fluids which transport dissolved methane into the gas hydrate stability field, producing pore filling and load bearing hydrate, respectively.
During this work, four major research questions were addressed:

- Can the spatial hydrate distribution within LARS be resolved using remote sensing methods?

The spatial hydrate distribution in the early LARS experiments [Schicks et al. 2011, 2013] was unknown. Because the spatial hydrate distribution is one crucial

factor for proper reservoir characterization, the LARS setup was equipped with a 375 electrode **e**lectrical **r**esistivity **t**omography (ERT) array [Priegnitz et al. 2013]. This system was used to monitor the electrical properties of the sediment sample during hydrate formation and dissociation experiments.

- Can the spatial resistivity distribution be used to estimate and quantify the spatial hydrate distribution?

The frequently recorded ERT data sets should be used as input data for a data-processing routine aiming to convert the spatial resistivity distribution into a quantified spatial hydrate distribution.

- Are the results obtained in LARS comparable and transferable to natural gas hydrate deposits?

Whereas pore filling hydrate formation experiments last for several weeks, the formation process of naturally formed hydrate can last for 10^5 - 10^7 years [Rempel and Buffett 1997]. Even though particular attention was laid on the technique of hydrate formation in order to mimic natural hydrate formation as good as possible in LARS, the comparability of artificially formed hydrates to natural hydrates has to be questioned.

- How do gas flow patterns of hydrate dissociation experiments in LARS compare to field data?

Once the desired hydrate saturation is achieved in LARS, hydrate decomposition can be initiated in different ways (see chapter 1.1). It was desired to perform at least two hydrate dissociation experiments which were supposed to mimic the field tests performed in 2007/2008 at the Mallik test site in the Mackenzie Delta, Canada (see. e.g. Wright et al. [2011b]). Those experiments intended to investigate how the gas and water flow patterns in our LARS experiments compare to field data. Special focus was laid on the response of gas and water production for different pressure stages and conceptual models of different transport behaviours in the pore space.

The main body of this thesis consists of four publications which intend to address the questions above (see table 1.3). To investigate the formation of methane hydrates in LARS, an **e**lectrical **r**esistivity **t**omography (ERT) array was developed. The technical setup and the data quality of the ERT array are introduced in publication I. Publication II presents the experimental results obtained from the ERT system while monitoring several hydrate formation and dissociation experiments in LARS. In publication III the general appropriateness of comparing laboratory formed hydrate reservoirs to natural deposits is investigated. The production performance of released gas and water during depressurization experiments is presented in publication IV.

Table 1.3.: Overview of manuscripts published or submitted during this thesis.

Pub. Nr.	Title	Authors	Status
1	A cylindrical electrical resistivity tomography array for three-dimensional monitoring of hydrate formation and dissociation	**Mike Priegnitz**, Jan Thaler, Erik Spangenberg, Carsten Rücker, and Judith M. Schicks	published in: Rev. Sci. Instrum. (2013) 84, 104502 ; doi: 10.1063/1.4825372
2	Characterizing electrical properties and permeability changes of hydrate bearing sediments using ERT data	**Mike Priegnitz**, Jan Thaler, Erik Spangenberg, Judith M. Schicks, Jörg Schrötter, and Sven Abendroth	published in: Geophys. J. Int. (2015) 202 (3): pp 1599-1612. doi: 10.1093/gji/ggv245
3	Are Laboratory-Formed Hydrate-Bearing Systems Analogous to Those in Nature?	Erik Spangenberg, **Mike Priegnitz**, Katja Heeschen, and Judith M. Schicks	published in: J. Chem. Eng. Data (2015) 60 (2), pp 258-268; doi: 10.1021/je5005609
4	Gas production from methane hydrate - simulating the multistage depressurization test in Mallik, Canada	Katja U. Heeschen, Sven Abendroth, **Mike Priegnitz**, Erik Spangenberg, Jan Thaler, and Judith M. Schicks	submitted to: Environmental Science & Technology

2. Publication I: A cylindrical electrical resistivity tomography array for three-dimensional monitoring of hydrate formation and dissociation

Authors:

Mike Priegnitz, Jan Thaler, Erik Spangenberg, Carsten Rücker, and Judith M. Schicks

Published as:

Priegnitz, M., Thaler, J., Spangenberg, E., Rücker, C., Schicks, J. (2013): A cylindrical electrical resistivity tomography array for three-dimensional monitoring of hydrate formation and dissociation. - Review of Scientific Instruments, 84, p. 104502.

DOI: http://doi.org/10.1063/1.4825372

Reprinted with permission from AIP Publishing. Copyright 2013 AIP Publishing.

Contribution

I planned the research together with Dr. Erik Spangenberg and Jan Thaler. Dr. Carsten Rücker provided the inversion software which was implemented at GFZ by Jan Thaler and me. I carried out the measurements; data analysis was done together with Jan Thaler. Finally, I wrote the manuscript with help of Dr. Judith Schicks.

REVIEW OF SCIENTIFIC INSTRUMENTS **84**, 104502 (2013)

A cylindrical electrical resistivity tomography array for three-dimensional monitoring of hydrate formation and dissociation

Mike Priegnitz,[1,a)] Jan Thaler,[1] Erik Spangenberg,[1] Carsten Rücker,[2] and Judith M. Schicks[1]
[1]*Helmholtz Centre Potsdam, GFZ German Research Centre for Geosciences, Telegrafenberg, Potsdam 14473, Germany*
[2]*Institute of Applied Geosciences, Technical University Berlin, Berlin, Germany*

(Received 19 July 2013; accepted 3 October 2013; published online 29 October 2013)

The LArge Reservoir Simulator (LARS) was developed to investigate various processes during gas hydrate formation and dissociation under simulated *in situ* conditions of relatively high pressure and low temperature (close to natural conditions). To monitor the spatial hydrate distribution during hydrate formation and the mobility of the free gas phase generated during hydrate dissociation, a cylindrical Electrical Resistivity Tomography (ERT) array was implemented into LARS. The ERT contains 375 electrodes, arranged in 25 circular rings featuring 15 electrodes each. The electrodes were attached to a neoprene jacket surrounding the sediment sample. Circular (2D) dipole-dipole measurements are performed which can be extended with additional 3D cross measurements to provide supplemental data. The data quality is satisfactory, with the mean standard deviation due to permanent background noise and data scattering found to be in the order of 2.12%. The measured data are processed using the inversion software tool Boundless Electrical Resistivity Tomography to solve the inverse problem. Here, we use data recorded in LARS to demonstrate the data quality, sensitivity, and spatial resolution that can be obtained with this ERT array. © *2013 AIP Publishing LLC*. [http://dx.doi.org/10.1063/1.4825372]

I. INTRODUCTION

Gas hydrates are naturally occurring crystalline solids formed from water and small gas molecules (< 1 nm). The water molecules build a three-dimensional network of cavities via hydrogen bonds. Those cavities are occupied by "guest" gas molecules. Therefore, gas hydrates belong to a class of compounds known as clathrates or inclusion compounds.[1]

Natural gas hydrates form, as long as all of the following four conditions are fulfilled: (1) elevated pressure, (2) low temperature, (3) presence of sufficient amounts of water, (4) presence of sufficient amounts of gas. Due to the origin of natural gases, most gas hydrates feature methane as guest molecule but higher hydrocarbons and other constituents can be found as well (see, e.g., Sloan and Koh[1]). As the four formation conditions are fulfilled at all active and passive continental margins, deep inland seas, and permafrost areas, gas hydrates exist in quantities large enough to be considered as a potential energy resource.

In the framework of the German national gas hydrate project, SUGAR, the formation and dissociation of methane hydrates within the LArge Reservoir Simulator (LARS) were investigated. Methane hydrate has been formed successfully from methane saturated saline water under simulated *in situ* conditions while temperature and pressure profiles have been recorded. Production tests, using thermal stimulation or pressure reduction for the dissociation of hydrates were successfully performed (e.g., Schicks *et al.*[2,3]). However, there was no way to image the spatial distribution of hydrate crystals during hydrate formation and dissociation, nor could the free methane gas phase released during hydrate dissociation be tracked.

In geophysical aspects, the acoustic velocities and electric properties are more strongly affected by the presence of gas hydrates within some material than other properties.[4] On a laboratory and numerical basis, much work has been previously done to investigate and model both the formation and dissociation of gas hydrates in porous media. Klapproth *et al.*[5] investigated the formation of gas hydrates in gas saturated sediments by transformation of liquid water. They investigated quartz and mixtures of quartz and montmorillonite and kaolinite, respectively. The results show that each mineral play individual interaction with water and gas hydrate. Since the fraction of water was between 10% and 17%, the formed hydrate appears between the quartz grains like cement. Priest *et al.*[6] also interpreted from their measurements of seismic velocities on artificial hydrate-bearing sand samples and cementing effect of hydrates. On the other hand, Spangenberg[7] modelled the electrical resistivity of hydrate-bearing sediments assuming that hydrate forms as a non-cementing material in the pore space. The results of this modelling correspond very well with the experimental results where hydrates were formed from a methane saturated water phase in glass bead sediments.[8] Schicks *et al.*[9] performed experiments under simulated *in situ* conditions in a pressure cell. Under a microscope, they also observed hydrate formation in pore spaces without any contact to sediment grains.

Apparently, the role of formed hydrates differs and the results investigating hydrate formation strongly depend on the technical implementation. However, to mimic naturally

a)mikep@gfz-potsdam.de

occurring marine gas hydrate reservoirs, it seems to be reasonable to assume hydrate formation from the dissolved phase, where hydrates form uniformly distributed without preferred grain contact in the completely fluid saturated pore space.

Hydrate dissociation scenarios within porous media were simulated by Jang and Santamarina[10] with respect to gas recovery and residual gas saturations. Kwon *et al.*[11] modelled the P-T evolution along the phase boundary during hydrate dissociation and the effect of capillarity. They found that pore fluid pressure generation is proportional to the initial hydrate fraction and the sediment bulk stiffness but inversely proportional to the initial gas fraction and the gas solubility.

To better understand the mechanisms affecting hydrates to form and dissociate, tomographic imaging techniques are desirable. However, such tomographical systems to monitor the evolution of gas hydrates within sediments are not yet commonly established. On field scale, tomographical investigations have been done regarding the electromagnetic and seismic properties of hydrate bearing sediments. For example, Weitemeyer *et al.*[12] carried out a controlled source electromagnetic (CSEM) survey to detect gas hydrates at Hydrate Ridge, Oregon, USA. Bauer *et al.*[13] performed cross-well seismic tomography to investigate P-wave velocity, P-wave anisotropy, and P-wave attenuation in hydrate bearing sediments at the Mallik 5L-38 gas hydrate production research well.

On a laboratory scale, Kneafsey *et al.*[14] performed experiments in a pressure vessel on sand samples using X-ray computed tomography (CT) to monitor local density changes during the formation and dissociation of methane hydrates. They observed significant water migration and possible shifting of mineral grains in response to hydrate formation and dissociation, respectively. Since X-ray CT relies on density and the density of water and hydrate is very similar, X-ray CT cannot capture hydrate formation from the dissolved phase. Because this hydrate formation method is essential to mimic nature, suitable laboratory experiments need to be done together with a geophysical monitoring of the evolution of the hydrate content in porous sediment. However, to transform the monitored distribution and evolution of physical properties into the distribution and evolution of hydrate saturation, improved interpretation models are required.

Gas hydrate, like ice, is an electrical insulator. Similarly, hydrate formation, like ice formation, consumes water but excludes dissolved salt ions, meaning the electrical conductivity of the pore fluid increases with increasing hydrate saturation when using brine as a pore fluid. This builds up a high resistivity contrast between the forming hydrate crystals and the remaining fluid within the pore space.

During the hydrate dissociation process, the stationary electrically insulative gas hydrate converts into a mobile, high resistivity free gas phase and liquid water. Therefore, huge differences in the electrical properties within a specimen are expected during both the hydrate formation and dissociation processes, providing a strong signal that can be used for further geoelectrical analyses.

Commonly, multi-electrode geoelectrics are carried out using four electrodes. Two electrodes are used for current injection and two electrodes record the corresponding potential changes to gain information about the resistivity distribution within the investigated volume. This study presents a multi-electrode system composed of 375 electrodes to perform a cylindrical Electrical Resistivity Tomography (ERT) measurement to investigate the formation and dissociation of gas hydrates on a laboratory scale.

II. EXPERIMENTAL SETUP

In the framework of the SUGAR project, LARS is intended to provide experimental data relevant for testing innovative methods and approaches for producing methane from hydrate-bearing reservoirs. The ERT array was designed to provide an imaging capability while remaining compatible with existing LARS components and experimental conditions. Here, we briefly summarize the LARS system, then describe how the ERT is installed and operated.

A. LARS

To study the evolution of gas hydrates under simulated conditions close to natural conditions, a LARS has been developed (Fig. 1). A key aspect of this system is that hydrate is formed via the circulation of methane saturated water through the sediment. As highlighted in the Introduction, during the hydrate formation process, no free gas phase is present within the pressure vessel. This dissolved-phase hydrate formation technique fills the specimen pore space at rates in the order of $1\%-2\%$ per day.

Further details regarding LARS can be found in Schicks *et al.*[2]

Subsequent to the description of Schicks *et al.*,[2] the pressure vessel was modified to include steel mesh-plates and porous filter plates at the fluid in- and outlets of the pressure vessel (Fig. 2). The mesh-plates are directly in front of the inlet and outlet fluid capillaries to homogeneously distribute fluid over the entire cross sectional area of the pressure vessel. The porous filter plates are mounted on the specimen side of the mesh-plates and serve as a mechanically constraining fluid distributor. During both fluid injection and production, no pressure gradients should develop within the porous filter plates, as the fluid flow field only starts to change rapidly in the mesh-plates. Hence, a homogeneous fluid flow field within the sample is created.

Prior experiments considered temperature, pressure, and properties of the pore fluid, specifically the pore fluid's electrical conductivity. Frequent pore fluid sampling transferred the electrical conductivity increase into hydrate formed in LARS considering the salinity increase of the remaining water (Spangenberg and Kulenkampff[15]). This allowed the amount of hydrate formed to be calculated, but did not allow researchers to exactly localize and determine the spatial distribution of hydrate saturations within the sediment sample. Because we have an inhomogeneous temperature field during fluid circulation, hydrate formation rates are assumed to be higher in the colder parts of the sample compared to the warmer regions. To improve the determination of local changes regarding hydrate saturation, an ERT was

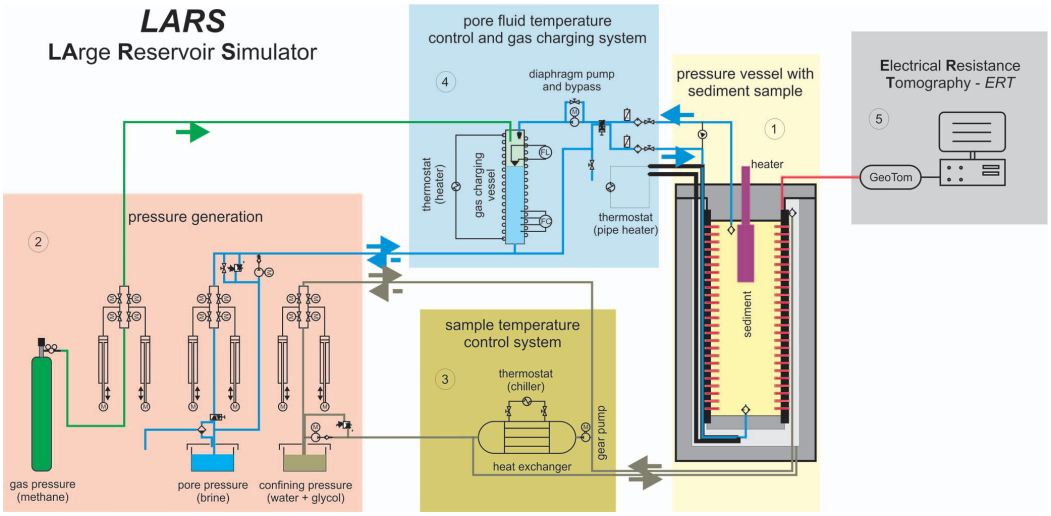

FIG. 1. Schematic of the five major components of LARS: (1) a pressure vessel (volume: 425 l) with a neoprene-jacketed sample and active cooling, (2) a pressure generating system to set up various confining and pore fluid pressure levels, (3) a sample temperature controlling system being able to apply *in situ* temperatures to the sample, (4) a pore fluid temperature control and gas charging system, (5) Electrical Resistivity Tomography (ERT).

implemented into the pressure vessel. The ERT serves as an imaging technique to monitor the spatial distribution of gas hydrates during hydrate formation. During hydrate dissociation, it might be possible to detect features related to gas release, as the produced free gas phase pushes pore fluid out of the pores, possibly increasing the bulk resistivity of the affected regions.

The ERT is attached to the neoprene jacket surrounding the sample material and now constitutes the fifth main component of LARS (5) (see Fig. 1). The ERT array contains 375 electrodes made of stainless steel, each with a sealing PEEK (Polyetheretherketon) casing, attached to the neoprene jacket (marked red in Fig. 1, shown separately in Fig. 3).

All electrodes had to be wired separately through the feed-throughs of the top closure of the pressure vessel of

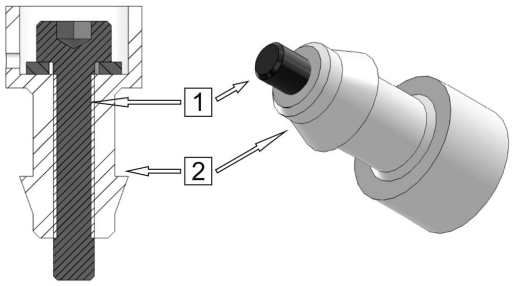

FIG. 3. Technical sketch of the electrodes. (1) Stainless steel M3×16 screw as electrode in (2) a self-sealing PEEK casing. Shown assembly is plugged into the neoprene jacket surrounding the sediment sample.

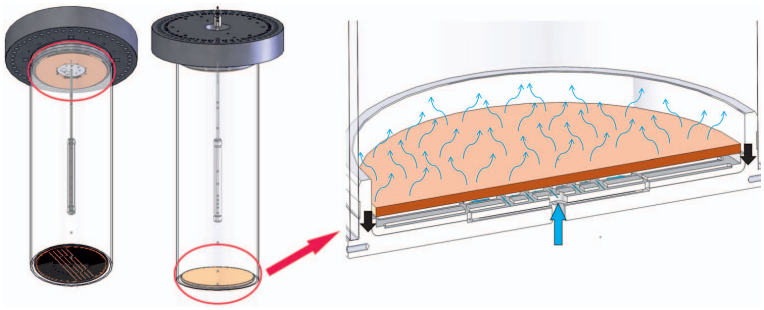

FIG. 2. Location and operation mode of the mesh- (gray) and porous filter plates (orange) in the pressure vessel of LARS.

LARS to provide further linkage to the data acquisition unit.

B. Inversion-boundless electrical resistivity tomography (BERT)

As the mathematical solution of an ERT always involves an inverse problem, the inversion software BERT[16] is used. In short, BERT uses a triple-grid inversion technique that is based on unstructured finite element meshes for forward calculation and parameter identification.[16] By using triangles (2D) and tetrahedrons (3D), BERT can follow arbitrary geometries. BERT is already well described and further details can be found, e.g., in Günther *et al.*[16]

C. Electrode layout

Common cylindrical electrode geometries feature electrode rings producing 2D slices. For multiple rings, the area between two slices gets interpolated during the inversion process. However, determining the optimum number of electrodes composing one ring and the total number of electrode rings is not trivial.

The data acquisition unit (see Sec. II E) limits the maximum number of ERT electrodes to 400. Since we defined to use BERT for data processing, the electrode layout was chosen to optimize the inversion quality in BERT. To find the best combination of the number of rings and the number of electrodes on each ring for 400 electrodes, four synthetic scenarios within LARS with a centred heat source were modelled and inverted:

Scenario I: Initial hydrate formation (increasing resistivity) in the boundary regions

Scenario II: Homogeneous hydrate saturation (high resistivity)

Scenario III: Initial hydrate dissociation at a centred heat source

Scenario IV: Advanced hydrate dissociation around a centred heat source.

Table I presents the inversion results with respect to the number of iterations, the relative root mean square deviation (rrms), and the χ^2 misfit (weighted data functional per data).

Generally, the best inversion results were obtained with the 40×10, 25×15, and 25×16 electrode geometries. Worrying about the mechanical stability of the neoprene jacket, the 40×10 geometry was eliminated. The next best model results were obtained with the 25×15 electrode geometry, and the 375 electrode design with 25 rings featuring 15 electrodes each was chosen (Fig. 4). Choosing 375 electrodes on the outer mantel instead of 400 also provides the future option of placing 25 electrodes at certain positions within the sediment sample.

D. Electrode configuration

Given our chosen electrode geometry, circular 2D slices are measured (Fig. 5(a)). A circular dipole-dipole configuration is chosen for practical reasons, as the required measurement time is $\approx$ 1/3 of that required for a Wenner configuration, and the penetration depth is much bigger. The measurement utilizes a fixed current injection dipole (electrodes A and B), while the potential measuring dipole (electrodes M and N) is shifted along the circular array (Fig. 5(b)). After six pairings of the M and N electrodes, providing 180° coverage (see Fig. 5(b)), the injection dipole is shifted by one electrode along the circular array and the potential measurements are repeated. This procedure is repeated until the injection dipole has covered 360° of the circular array, resulting in 90 individual measurements per 2D slice. Applying this measurement routine to all 25 circular 2D slices results in a total of 2250 individual measurements.

During data analysis, the volume between the measured 2D slices is inverted with respect to optimal model fitting. Besides the circular 2D dipole-dipole measurements, many other electrode configurations can be added to provide additional information. As the number of different electrode configurations is so large and their choice depends on the focus of investigation, other possible electrode configurations are not discussed at this point.

TABLE I. Inversion results for different synthetic LARS scenarios with respect to the electrode geometry (no. of rings × no. electrodes per ring); NaN – Not a Number (not definable, aborted).

	Electrode geometry	No. of iter.	rrms [%]	χ^2
Scenario I	10 × 40	7	1.95	2.35
	16 × 25	13	1.13	0.98
	15 × 25	12	1.08	0.89
	20 × 20	NaN	NaN	NaN
	25 × 15	5	0.99	0.89
	25 × 16	NaN	NaN	NaN
	40 × 10	5	0.87	0.72
Scenario II	10 × 40	NaN	NaN	NaN
	16 × 25	7	2.95	8.71
	15 × 25	7	2.56	6.53
	20 × 20	NaN	NaN	NaN
	25 × 15	11	1.17	1.36
	25 × 16	6	1.35	1.83
	40 × 10	5	0.96	0.92
Scenario III	10 × 40	9	2.74	7.63
	16 × 25	8	2.60	6.77
	15 × 25	7	2.66	7.07
	20 × 20	6	1.79	3.20
	25 × 15	7	1.21	1.48
	25 × 16	6	1.33	1.77
	40 × 10	7	0.87	0.75
Scenario IV	10 × 40	8	1.63	2.65
	16 × 25	10	1.10	1.19
	15 × 25	15	1.00	1.00
	20 × 20	10	1.02	1.05
	25 × 15	9	1.02	1.04
	25 × 16	9	1.00	1.00
	40 × 10	6	0.99	0.99

E. Data acquisition unit

Electrical measurements were performed using the high resolution multi-electrode multi-channel resistivity system

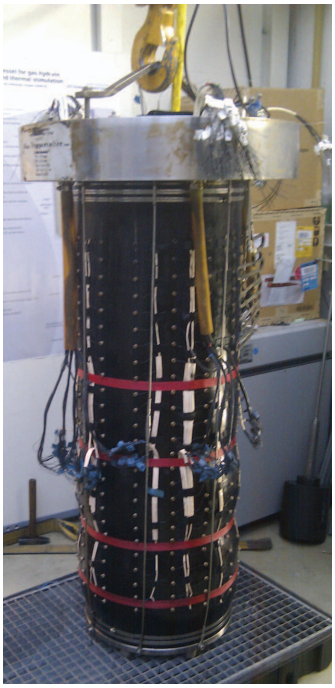

FIG. 4. Photograph of the specimen featuring the finalized 25 × 15 electrode geometry. An overhead crane connects via the yellow hook to the LARS top cap (silver) to support the specimen and lower it into the LARS pressure vessel. The vertical spacing between two neighbouring electrode rings is set to 45 mm and the horizontal spacing between two neighbouring electrodes is set to 100 mm.

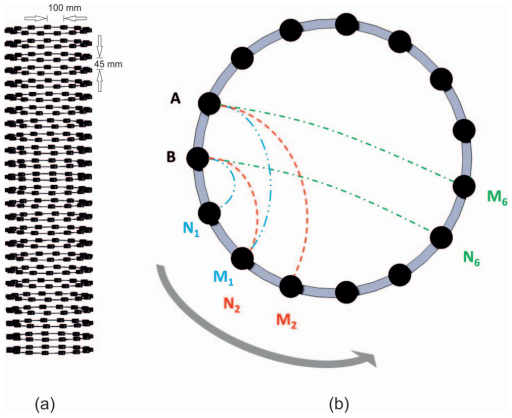

FIG. 5. Scheme of electrode configuration: (a) general electrode geometry with 25 electrode rings featuring 15 electrodes each, (b) circular dipole-dipole configuration with the current injection dipole at electrodes A and B, and the potential measuring dipole at electrodes M and N.

GeoTomMK8E1000 RES/IP/SP by GEOLOG 2000 (Augsburg, Germany). This unit supports a maximum of 400 electrodes and provides measurement resolutions down to 1 μV with an accuracy of 0.5%. Furthermore, frequencies between 1.042 Hz and 25 Hz and input currents from 0.001 mA up to 200 mA can be applied.

Individual electrode sequences can be programmed so that automatically scheduled measurements can be performed.

F. Measurement parameters

Prior to the electrical measurements, parameters such as applied frequency and input current have to be determined.

As no frequency-dependent effects regarding the electrical resistivity are expected for frequencies smaller than 30 kHz (shown by Pearson *et al.*[4] on tetrahydrofuran (THF)-hydrate saturated samples), the measurement frequency was set to the maximum value of 25 Hz to reduce the measurement time as much as possible. A complete measurement run at 25 Hz lasts approximately 35 min. Since the measured pore space hydrate formation rates are in the order of 1%–2% per day, we consider the measurements as steady state during the required measurement time. As mentioned above, the pore water salinity increases with increasing hydrate saturation within the pore space. Hence, the promoting effect of electrolysis at the electrodes for high pore fluid salinities (high hydrate saturation) has to be taken into consideration when choosing the magnitude of the input current. In water, electrolysis leads to the disintegration of water molecules into hydrogen and oxygen. The formation of gas bubbles at the electrodes, distorting the pore fluid properties and thus the ERT measurements, should be avoided. For measurements using a pore fluid with an initial salinity of 2.7 g/l, it has been found that an input current of 10 mA already causes small electrolysis effects at the electrodes for hydrate saturations greater than 70% (corresponding to a pore fluid conductivity of ≈12 mS/cm). Thus, for comparable initial salinities, the input current has to be 1 mA or smaller when high hydrate saturation is desired.

III. DATA QUALITY AND PRELIMINARY RESULTS

A. Data quality: Noise and reproducibility

To quantify the permanent noise effects during the measurements, a very simple scenario has been set up in LARS and measured repeatedly every 6 h for more than six days (26 measurements in total). This scenario utilizes a homogeneous sediment material and a predefined pore fluid of known salinity. The sediment sample was chosen to be medium to coarse quartz sand with a grain size distribution of ≈89% within the interval of 1000–500 μm. The pore fluid is distilled water with 3.68 g/l NaCl, resulting in a pore fluid conductivity of 6.5 mS/cm. The boundary conditions such as surrounding pressure (3 MPa) and temperature were kept constant (20 °C) during the noise measurements, so that no significant changes are expected during the measurements.

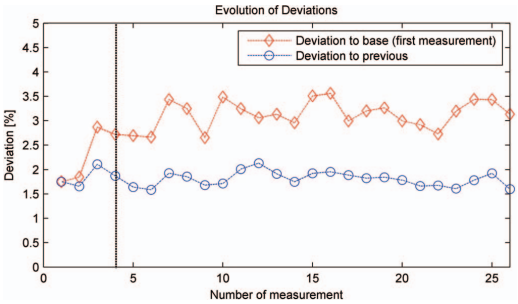

FIG. 6. Evolution of the deviations during the 26 noise measurements (6 h increment), blue line: deviation to the previous measurement, red line: deviation to the first measurement. The vertical dashed line marks the first 24 h it takes the system to reach thermal and chemical equilibrium at given pressure.

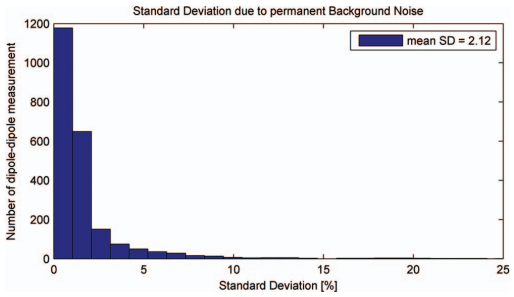

FIG. 7. Standard deviations of all 2250 dipole-dipole measurements determined with the 26 noise measurement runs.

The deviation evaluation (Fig. 6) for the noise measurements was estimated as follows: Every measurement run featured 2250 individual dipole-dipole measurements. For the blue line in Fig. 6, each dipole-dipole measurement was compared with its prior value and the deviation was determined. The 2250 deviation values thus obtained were summarized to a mean value and plotted against the measurement number. Hence, the blue line displays the mean deviation of every complete noise measurement to its prior value. The graph appears smooth and free of any trends, only fluctuating around 1.81%.

However, those deviations do not yield any information on the total trend of the deviation. The observed deviations of a noise measurement compared to its previous value could either be caused by a continuous divergence, e.g., in terms of a continuous deviation increase, or by a statistic distribution around a mean value. The red line in Fig. 6 compares the 2250 individual dipole-dipole measurements of all 26 noise measurements with the data from the very first measurement run. This comparison considers the temporal deviation to a base measurement and thus yields information on the total deviation trend. One observes that the red line in Fig. 6 fluctuates around some value between 2.5% and 3.5% and seems to hover around a mean value. This indicates that each dipole-dipole measurement appears to be statistically distributed around a mean value and one can assume the standard deviation for all 2250 individual measurements is caused by permanent background noise. Generally, the most deviation variations are observed within the first 3–4 noise measurements, corresponding to the first 18–24 h. After this period (marked by the vertical dashed line in Fig. 6), the deviations appear much more stable. Hence, it seems like it takes the entire system ≈24 h to reach thermal and chemical equilibrium at given pressure.

Fig. 7 presents the standard deviation of all 2250 individual dipole-dipole measurements made during the 26 noise measurement runs. One observes the standard deviation generally shows satisfactory values. 93.1% of the dipole-dipole measurements display deviations smaller than 5% and 87% of the total data show deviations even smaller than 3%. The mean standard deviation of all 2250 individual dipole-dipole measurements was found to be 2.12%.

The inverse problem of the data sets is solved during the inversion process. According to the basic equations for geoelectrical investigations formulated by Archie,[17] the electrical resistivity for fully saturated porous materials is given by

$$\rho_s = \frac{a}{\phi^m}\rho_{fl}, \tag{1}$$

where ρ_s denotes the formation resistivity of the sample material fully saturated by the fluid of resistivity ρ_{fl}, ϕ is the formation porosity, and a and m are empirical parameters. Note, that the inversion process is generally affected by numerous inversion parameters (starting model, regularization, etc.) and the inversion errors and deviations thus have to be considered separately.

As Eq. (1) is composed of constant parameters for a given sample material, the formation resistivity ρ_s is mainly influenced by the resistivity ρ_{fl} of the pore filling material. To estimate the possible influences of the sediment material on the pore fluid, four pore fluid specimens solutions were chemically analysed. Initially, all solutions featured only distilled water and ≈3.6 g of NaCl. One solution has been circulated through the LARS setup for several days, granting long term contact with the quartz sand described above. The remaining three solutions were prepared identically to the first, but separately in the laboratory and analysed without being in contact with the sediment at all. The results of the pore fluid analysis are given in Table II.

The results show the pore fluid composition is strongly influenced by the sediment contact. The ratio of Na to Ca, K, and Mg differs: it turned out that the relative concentration of Ca, K, and Mg increases due to the sediment contact.

TABLE II. Pore fluid analysis, comparison of circulated pore fluid (long term sediment contact) to similar prepared solutions without any sediment contact (three separate attempts to make exactly the fluid circulated through the specimen); values in mg/l.

	Na	Ca	K	Mg
Circulated pore fluid	1420	19	<20	2.9
Prepared solution I	1280	3.4	<10	0.64
Prepared solution II	1365	2.2	<10	0.44
Prepared solution III	1233	3.1	<10	0.50

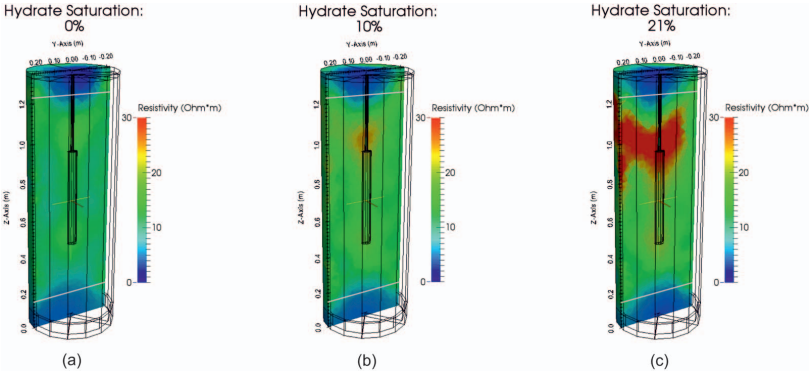

FIG. 8. Inversion results within LARS with a centred heat source for three states of hydrate formation. The horizontal gray lines mark the top and bottom bound of the electrode array. Data beyond these lines constitute an extrapolation of the inversion algorithm. (a) An almost homogeneous resistivity distribution exists at 0% hydrate saturation. (b) For 10% pore space hydrate saturation, no significant changes are observed as the formed hydrates are assumed to be widely spread within the reservoir and the resistivity increases homogeneously by ≈2 Ω m. Some localized hydrate formation near the top of the heat source can be seen, however. (c) The first widespread high resistivity accumulation is observed in the top area for 21% hydrate saturation.

This indicates mineral and thus ion exchange during sediment contact with the pore fluid, which may need to be considered depending on the aim of the experiment. However, for the ERT presented here, the ion exchange process does not result in measurable fluid conductivity changes and can be neglected.

B. Preliminary results

The ERT has been applied to a hydrate formation experiment within LARS. The water saturated quartz sand specimen described above was set to P-T-conditions deep in the stability field for methane hydrate (4 °C and 11.5 MPa). The circulating water was sprayed through the gas headspace in the gas-water-interface chamber to dissolve methane in the circulating water. To avoid hydrate formation in the gas-water-interface chamber, it is set to a temperature of 20 °C. The methane charged water enters the sample at a temperature slightly above hydrate stability to avoid clogging the fluid inlet. The water cools down as it migrates through the cold sediment. As the fluid temperature drops, the water cannot hold as much methane in the dissolved phase. Excess methane comes out of solution to form hydrate. As hydrate formation consumes water but excludes the salt ions, repeated electric conductivity measurements of the pore fluid can be used to estimate the actual degree of pore space hydrate saturation (see, e.g., Spangenberg and Kulenkampff[15]). The inversion results (Fig. 8) show the ERT is capable of monitoring the hydrate formation within the specimen.

As the fluid flow direction in this case is from top to bottom, the relative warm pore fluid enters the autoclave from the top. The top and bottom 14.5 cm of the neoprene jacket are not covered by electrodes and hence constitute an extrapolation region during the inversion process. The low resistivity areas at the top and bottom end faces can thus not be considered as actual measured phenomena. Moreover, the extrapolation of both areas is considered to be influenced by insufficient thermal insulation due to wiring and by massive metal influences from the top and bottom closures.

At the beginning of the experiment, the ERT results yield an almost homogeneous resistivity distribution in the order of ≈9 Ω m. Assuming Archie's[17] equation with a saturation exponent of 2 (Fig. 9, blue line), or the to date only available measured dependence of resistivity index I on saturation[15] (Fig. 9, black circles)

$$I = \frac{\rho_t}{\rho_0}, \tag{2}$$

where ρ_t is the true measured resistivity and ρ_0 is the resistivity at 100% water saturation, we cannot expect a strong resistivity increase in the ERT results at low hydrate saturations (see Fig. 9). At a homogeneous hydrate saturation of about 10%, the resistivity is expected to increase by a factor of about 1.2 (see Fig. 9) which matches the data (resistivity increase of ≈2 Ω m) very well. The majority of the formed hydrates at this stage can thus be assumed to be widely distributed within the reservoir. Interestingly, the first small block of elevated

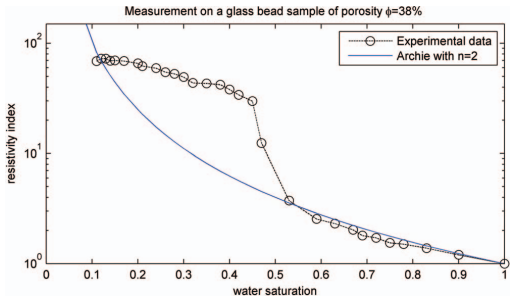

FIG. 9. Measured resistivity index evolution (black circles) versus water saturation compared to Archie's equation with a saturation exponent of 2 (blue line), modified after Spangenberg and Kulenkampff.[15]

resistivity appears to establish in the upper centre at the top of the thermal heat source. This could be either caused by additional nucleation points provided by the thermal heat source or by the enhanced thermal conductivity of the metal heat reactor, carrying the low temperatures fast into the specimen's centre. Since hydrate formation is considered a statistic process, further measurements are required to prove if this phenomenon is random or systematic. However, for hydrate saturations greater than 20%, we see areas in the ERT images where resistivity increased by a factor of about 2. From the small centre block, hydrate formation appears to expand to the boundary regions of the reservoir. The mentioned dependencies (Fig. 9) suggest for such areas local hydrate saturations between 30% and 40%.

Generally, active cooling from the surrounding is assumed to promote hydrate formation especially in the boundary regions, as the stability conditions are first fulfilled where the temperatures are lowest. Therefore, high resistivity methane hydrate accumulations are mainly expected in the boundary regions of the autoclave during the hydrate formation process.

IV. SUMMARY

The cylindrical ERT feature of LARS presented in this study constitutes a remote-sensing method of monitoring the gas hydrate evolution. The 375 electrode system yields satisfying, reproducible data quality, with a mean standard deviation of 2.12%. Measuring the resistivity distribution within the investigated volume can provide new insights into the spatial distribution of forming hydrate crystals.

Unlike X-ray CT, the ERT is capable of monitoring hydrate formation from the dissolved phase. Measurements can be performed under simulated *in situ* conditions, while relatively short measurement times of ≈35 min provide adequate time resolution. The spatial sensitivity of the ERT still needs to be quantified, but appears to be in the region of 5–10 cm.

ACKNOWLEDGMENTS

The German Federal Ministry of Economy and Technology provided funding for this work within the SUGAR project through Research Grant No. 03SX250E. Furthermore, the authors thank the staff of the GFZ workshops, Ronny Giese, and Alexander Reichardt for invaluable technical help and for the construction of the ERT system, as well as Christian Fuss for his support regarding the GeoTom.

[1] E. Sloan and C. Koh, *Clathrate Hydrates of Natural Gases*, Chemical Industries (CRC Press, 2008).

[2] J. M. Schicks, E. Spangenberg, R. Giese, B. Steinhauer, J. Klump, and M. Luzi, Energies **4**, 151 (2011).

[3] J. M. Schicks, E. Spangenberg, R. Giese, M. Luzi-Helbing, M. Priegnitz, and B. Beeskow-Strauch, Energies **6**, 3002 (2013).

[4] C. Pearson, J. Murphy, and R. Hermes, J. Geophys. Res., [Solid Earth] **91**, 14132, doi:10.1029/JB091iB14p14132 (1986).

[5] A. Klapproth, K. S. Techmer, S. A. Klapp, M. M. Murshed, and W. F. Kuhs, in *Proceedings of the 11th International Conference on the Physics and Chemistry of Ice, Bremerhaven, Germany, 23–28 July 2006* (Royal Society of Chemistry, 311, 2007), p. 321.

[6] J. A. Priest, A. I. Best, and C. R. I. Clayton, J. Geophys. Res., [Solid Earth] **110**, B04102, doi:10.1029/2004JB003259 (2005).

[7] E. Spangenberg, J. Geophys. Res., [Solid Earth] **106**, 6535, doi:10.1029/2000JB900434 (2001).

[8] E. Spangenberg, J. Kulenkampff, R. Naumann, and J. Erzinger, Geophys. Res. Lett. **32**, L24301–L24303, doi:10.1029/2005GL024107 (2005).

[9] J. M. Schicks, M. Luzi, J. Erzinger, and E. Spangenberg, in *Proceedings of the 11th International Conference on the Physics and Chemistry of Ice, Bremerhaven, Germany, 23–28 July 2006* (Royal Society of Chemistry, 311, 2007), p. 537.

[10] J. Jang and J. Santamarina, J. Geophys. Res. **116**, B08202, doi:10.1029/2010JB007841 (2011).

[11] T.-H. Kwon, G.-C. Cho, and J. C. Santamarina, Geochem., Geophys., Geosyst. **9**, Q03019, doi:10.1029/2007GC001920 (2008).

[12] K. A. Weitemeyer, S. Constable, and A. M. Tréhu, Geophys. J. Int. **187**, 45 (2011).

[13] K. Bauer, C. Haberland, R. G. Pratt, F. Hou, B. E. Medioli, and M. Weber, Geol. Surv. Canada, Bull. **585**, 21 (2005).

[14] T. J. Kneafsey, L. Tomutsa, G. J. Moridis, Y. Seol, B. M. Freifeld, C. E. Taylor, and A. Gupta, J. Pet. Sci. Eng. **56**, 108 (2007).

[15] E. Spangenberg and J. Kulenkampff, Geophys. Res. Lett. **33**, L24315, doi:10.1029/2006GL028188 (2006).

[16] T. Günther, C. Rücker, and K. Spitzer, Geophys. J. Int. **166**, 506 (2006).

[17] G. E. Archie, Trans. AIME **146**, 54 (1942).

3. Publication II: Characterizing electrical properties and permeability changes of hydrate bearing sediments using ERT data

Authors:

Mike Priegnitz, Jan Thaler, Erik Spangenberg, Judith M. Schicks, Jörg Schrötter, and Sven Abendroth

Published as:

Priegnitz, M., Thaler, J., Spangenberg, E., Schicks, J., Schrötter, J., Abendroth, S. (2015): Characterizing electrical properties and permeability changes of hydrate bearing sediments using ERT data. - Geophysical Journal International, 202, 3, p. 1599-1612.

DOI: http://doi.org/10.1093/gji/ggv245

Reprinted with permission from Oxford University Press. Copyright 2015 Oxford University Press.

Contribution

I planned the research together with Dr. Erik Spangenberg and Dr. Judith Schicks. Jörg Schrötter provided the temperature measurement system; the obtained temperature data was analysed by Jörg Schrötter and me. I designed the data processing routine which allowed to transform the electrical resistivity distribution into the spatial distribution of hydrate and permeability saturation, respectively. Together with Jan Thaler the data processing routine was implemented and applied. Sven Abendroth provided information for permeability analyses, which were carried out by me. Finally, I wrote the manuscript with helpful advices of all co-authors.

Geophysical Journal International

Geophys. J. Int. (2015) **202,** 1599–1612 doi: 10.1093/gji/ggv245
GJI Marine geosciences and applied geophysics

Characterizing electrical properties and permeability changes of hydrate bearing sediments using ERT data

Mike Priegnitz, Jan Thaler, Erik Spangenberg, Judith M. Schicks, Jörg Schrötter and Sven Abendroth

Helmholtz Centre Potsdam, GFZ German Research Centre for Geosciences, Potsdam, Germany. E-mail: mikep@gfz-potsdam.de

Accepted 2015 June 5. Received 2015 June 5; in original form 2015 March 9

SUMMARY

A LArge Reservoir Simulator (LARS) was equipped with an electrical resistivity tomography (ERT) array to monitor hydrate formation and dissociation experiments. During two hydrate formation experiments reaching 90 per cent bulk hydrate saturation, frequent measurements of the electrical properties within the sediment sample were performed. Subsequently, several common mixing rules, including two different interpretations of Archie's law, were tested to convert the obtained distribution of the electrical resistivity into the spatial distribution of local hydrate saturation. It turned out that the best results estimating values of local hydrate saturation were obtained using the Archie$_{var-phi}$ approach where the increasing hydrate phase is interpreted as part of the sediment grain framework reducing the sample's porosity. These values of local hydrate saturation were used to determine local permeabilities by applying the Carman-Kozeny relation. The formed hydrates were dissociated via depressurization. The decomposition onset as well as areas featuring hydrates and free gas were inferred from the ERT results. Supplemental consideration of temperature and pressure data granted information on discrete areas of hydrate dissociation.

Key words: Tomography; Electrical properties; Gas and hydrate systems; Permeability and porosity.

1 INTRODUCTION

Gas hydrates are ice-like crystalline solids composed of a 3-D network of water molecules enclosing small (<1 nm) guest molecules (Von Stackelberg *et al.* 1947). Naturally occurring gas hydrates predominantly contain methane (CH_4) as guest molecules, however, higher hydrocarbons and mixed hydrates can be found as well (Milkov *et al.* 2005). Since hydrates are stable wherever sufficient amounts of water, hydrate forming gas, elevated pressure, and low temperatures are present, natural gas hydrates occur at active and passive continental margins, permafrost areas and deep inland seas (Sloan & Koh 2008). Global estimates of methane encapsulated in gas hydrates vary by several orders of magnitude. Whereas Kvenvolden and Grantz (Kvenvolden & Grantz 1990) assumed 1×10^{15} m^3 of CH_4, Klauda & Sandler (2005) estimated that there is as much as 1.2×10^{17} m^3 of methane gas globally bound in gas hydrates. Thus, gas hydrate reservoirs have become of great interest during the last decades, as the amounts of hydrate-bonded carbon are considered to be a potential energy resource as well as a source of greenhouse gases.

Recent efforts aim at conducting field tests to produce methane from hydrate bearing sediments. Generally, gas hydrates can be decomposed by disturbing their thermal equilibrium (heating), mechanical equilibrium (depressurization) or chemical equilibrium (e.g. by injecting CO_2). All of these production techniques have been successfully tested on a field scale: in the winter of 2001/2002 the first ever gas production test directly from hydrate bearing sediments was carried out via thermal stimulation by injecting hot fluid in the hydrate bearing sediment layers at the Mallik test site in the Mackenzie Delta, Canada (e.g. Dallimore & Collett 2005). Later, the decomposition of hydrates via depressurization was carried out at the Mallik test site in 2007/2008 (e.g. Wright *et al.* 2011) and in the Nankai Trough, Japan in 2013 (Yamamoto 2014). The applicability of methane production via CO_2–CH_4 exchange was tested in 2012 at the Alaska North Slope, known as Ignik Sikumi #1 Gas Hydrate Field Trial (Lee & White 2014). Regardless of the decomposition technique, a proper reservoir characterization is required to successfully produce methane from hydrate bearing reservoirs. Therefore, imaging techniques are deployed to natural gas hydrate reservoirs to monitor essential reservoir parameters such as electrical or seismic properties on a field scale.

Bauer *et al.* (2005) performed a cross-well tomography at the Mallik 5L-38 gas hydrate production research well to monitor the elastic parameters such as seismic velocities, attenuation and anisotropy of the hydrate bearing sediment layers. Using marine controlled source electromagnetics, Schwalenberg *et al.* (2010) investigated the electromagnetic properties on active ocean-continent collision regions on the Hikurangi Margin, offshore New Zealand,

© The Authors 2015. Published by Oxford University Press on behalf of The Royal Astronomical Society.

to verify seismical and geochemical evidences for the presence of gas hydrates.

Reducing the complexity of field experiments, the mechanisms accompanying hydrate formation and dissociation still raise questions even on a pilot scale. The nucleation of hydrates strongly depends on the type of hydrate formation (at a gas–water interface or from the dissolved phase) and the sediment (Rydzy 2013). In addition, gas migration during hydrate decomposition depends on the specific spatial distribution of hydrates in the pore space and can significantly differ each time. To better understand how and where hydrates form and to detect the pathways of the produced free gas phase, imaging techniques are essential at all scales, field tests as well as laboratory experiments.

Ersland *et al.* (2009) monitored hydrate formation and subsequent CO_2 injection in a high pressure cell using a magnetic resonance imaging (MRI) technique. Analysing these MRI data they were able to determine the amount and the distribution of water, free gas and methane hydrates in Bentheim sandstone core plugs. Kneafsey *et al.* (2007) monitored local density changes in a pressure vessel during hydrate formation and dissociation using X-ray computed tomography (CT). They observed potential mineral grain shifting as a response to hydrate formation and dissociation and significant water migration. However, X-ray CT relies on density. Since the densities of (sea)water and hydrate are very similar, X-ray CT measurements are not sensitive to hydrate formation from a dissolved phase without a free gas phase. This problem can be avoided by adding relatively heavy salt ions to the pore water increasing the pore water's density (Rydzy 2013), though one has to keep in mind that dissolved salt ions reduce the CH_4 solubility, thus altering the hydrate equilibrium conditions. As it is assumed that hydrate formation from methane dissolved in water more closely explains the formation of natural, marine gas hydrates in sandy formations (Buffett & Zatsepina 2000), efforts are required to develop experiments allowing for geophysical monitoring of the formation of hydrates from dissolved CH_4 and their dissociation.

Therefore, a LArge Reservoir Simulator (LARS) has been developed in the framework of the German national gas hydrate project SUGAR (Schicks *et al.* 2011, 2013). This reservoir simulator permits the formation of gas hydrates from methane-loaded brine under simulated *in situ* conditions mimicking marine scenarios. LARS is equipped with a series of sensors: different types of instrumentation can be used allowing for live temperature monitoring within the sediment sample. A cylindrical electrical resistivity tomography (ERT) array composed of 375 electrodes is used to monitor the formation and dissociation of gas hydrates within LARS. A good ERT-resolution is granted by the large electrical contrasts in the pore space, as the present phases of non-conducting sediment, well conducting saline pore fluid, and poorly conducting hydrates cover a wide range of electrical properties. During the respective hydrate dissociation, the stationary high-resistive hydrate phase converts into an isolating but mobile free gas phase. Thus, significant changes of the sediment's electrical properties are expected throughout the entire hydrate evolution, suggesting the use of an ERT array.

This study presents data of three hydrate formation experiments. In particular we focus on the ERT and temperature data of two hydrate formation experiments filling ≈90 per cent of the sediment's pore space (LARS RUNs 2 and 4) and the subsequent hydrate dissociation experiments. The latter simulated the 2008 Mallik production test, where the pressure was reduced in several steps. Furthermore, we show how local hydrate saturation and permeability changes during hydrate formation can be estimated using a data processing routine based on commonly applied models.

Table 1. Summary of relevant parameters used for the ERT measurements.

Electrode configuration:	Circular dipole–dipole
Stacking	10 x
Input current	1 mA
Frequency	25 Hz
Measurement interval	4 h
Measurement duration	25–30 min

2 LARS, ERT AND EXPERIMENTAL PARAMETERS

To investigate the formation and dissociation of gas hydrates under simulated *in situ* conditions, a LARS has been developed. Within the LARS, hydrate is formed from methane-loaded saline water circulating through a 210 litre sediment sample. Thus, no free gas phase is present in the sediment sample until hydrate dissociation is initiated. So far, hydrate dissociation in LARS has been initiated by depressurization or thermal stimulation, using an implemented counter-current heat-exchange reactor. For a detailed description of both, LARS and the heat reactor, see Schicks *et al.* (2011, 2013).

A cylindrical ERT array has been installed in LARS to acquire new knowledge on the spatial distribution of hydrate growth in the sediment sample. The ERT features 375 electrodes arranged in 25 circular rings with 15 electrodes in each ring. The tomographical array installed in LARS and its data quality are described elsewhere (Priegnitz *et al.* 2013). As ERT measurements always provide an inverse problem, the measured data has been processed using the inversion software Boundless Electrical Resistivity Tomography BERT (Günther *et al.* 2006). Table 1 lists the relevant parameters used for the ERT measurements.

We performed three hydrate formation experiments in LARS filling as much as 89.5 per cent (LARS RUN 2), 50 per cent (LARS RUN 3) and 90 per cent (LARS RUN 4) of the sample's pore space, respectively. The sediment sample used for the experiments LARS RUNs 2 and 3 was a medium to coarse quartz sand with a narrow grain size distribution of ≈89 per cent within the interval of 500–1000 µm. The corresponding initial porosity was 35 per cent. The respective permeability at ambient conditions was determined to be 673 ± 11 *D*. LARS RUN 4 featured a slightly coarser quartz sediment sample with 98.5 per cent of the sand being in the interval 500–1000 µm. The corresponding porosity and permeability were determined to be 39.2 per cent and 2030 *D* ± 23 *D*. The pore fluid in all three experiments was a 3.68 g l^{-1} NaCl-water solution with an initial conductivity of ≈6.5 mS cm^{-1}. The saline pore fluid was loaded with CH_4 in a gas-water interface chamber and injected into the sediment sample. To avoid clogging by hydrates at the fluid inlet, the methane-loaded saline water entered the sample at a temperature 3–4 °C above the hydrate stability temperature for a given pressure. This small temperature shift still allowed methane concentrations close to saturation in the pore fluid (Spangenberg *et al.* 2015). Inside the sediment sample hydrate stability conditions were achieved by active cooling of the sample's surrounding (T_{conf} = 4 °C). The rapid temperature drop decreased the methane solubility of the pore fluid. The resulting supersaturation (excess methane) was available for hydrate formation. Waite & Spangenberg (2013) showed that the degree of excess methane is in the order of 40 per cent of the initial methane concentration. After migrating through the sediment sample, the pore fluid was reloaded with CH_4 and entered the sample again. The pore pressure was held constant at 11 MPa throughout the hydrate formation experiments. By circulating the methane-loaded

pore fluid through the sediment sample we were able to achieve hydrate saturation rates of up to ≈2 per cent per day.

The LARS RUN 4 experiment was destined to examine the hydrate formation and dissociation patterns observed in LARS RUN 2 with a different sediment material as well as a different temperature sensing technique and to ideally proof the reproducibility of our experiments. During LARS RUNs 2 and 3, the temperature within the sediment sample was measured using 14 spatially distributed PT100 temperature sensors. PT100 sensors generally yield very accurate temperature data, though they cover very little area. Prior to LARS RUN 4 the spatially distributed PT100 sensors were replaced by a distributed-temperature-sensing (DTS) coil. A total length of ≈11 m DTS coil meandered throughout the specimen allowing increased spatial coverage. However, the installed DTS system yielded averaged temperature values for 0.5 m intervals, reducing the spatial sensitivity.

The injection of relatively warm methane-loaded pore fluid produced an inhomogeneous temperature field in the sediment sample. Because the electrical resistivity varies with temperature, the most accurate results were obtained by stopping the circulation to produce a homogeneous temperature field for the ERT measurements. Hence, methane saturated pore fluid was continuously circulated for five days, increasing the specimen's hydrate saturation by approximately 10 per cent (referred to as injection period). After this period circulation was stopped to ensure thermal equilibrium within the sediment sample. ERT measurements were performed every four hours throughout the entire hydrate formation experiments, providing data for both thermal equilibrium and non-equilibrium states.

3 ESTIMATING LOCAL HYDRATE SATURATION AND PERMEABILITIES

The inverted resistivity data obtained from ERT measurements serve as an indirect measure of the hydrate content in the pore space. Since the solid hydrate phase is directly related to the electrical and hydraulic properties of the pore space, the resistivity distribution can be converted into the distribution of hydrate saturation S_H and permeability K.

3.1 Hydrate saturation

The bulk hydrate saturation during the hydrate formation experiments has been determined by frequent pore fluid sampling. During hydrate formation only fresh water is consumed, while dissolved salt ions accumulate in the residual pore fluid, increasing the electrical conductivity. Following Spangenberg & Kulenkampff (2006), the variations of pore fluid conductivity can be converted into the mass of produced methane hydrate and hydrate pore space saturation as follows: The NaCl concentration of the pore fluid is linked to the electrical conductivity by

$$c = \frac{\sigma}{\Lambda_{\mathrm{eq}}} \tag{1}$$

where c is the NaCl concentration, σ is the measured electrical conductivity of the pore fluid and Λ_{eq} is the equivalent conductivity. Considering the mass fraction of a solution with an initial NaCl concentration c_0, the mass of water consumed in hydrate formation at a certain time t can be calculated using

$$m_{w-h}(t) = m_{w_0}\left(1 - \frac{c_0}{c(t)}\right) \tag{2}$$

where m_{w-h} is the mass of water consumed in hydrate formation at a given time t, m_{w_0} is the mass of water present at the very beginning of the experiment, and c_0 and $c(t)$ are the NaCl concentrations at the beginning of the experiment and at time t, respectively. Based on the methane hydrate composition $CH_4 \bullet 5.9H_2O$ (Stern *et al.* 2003) and the density of methane hydrate ρ_{hydrate}, the mass of produced hydrate m_{hydrate} can be determined from the water consumption m_{w-h}. Additionally considering the sample's pore volume V_{pore} allows to calculate the bulk hydrate saturation

$$S_{\mathrm{hydrate}} = \frac{m_{\mathrm{hydrate}}}{V_{\mathrm{pore}} * \rho_{\mathrm{hydrate}}} \tag{3}$$

For all LARS RUNs, these bulk hydrate saturation values served as a reference baseline to verify the saturations gained from the ERT data.

Converting the electrical resistivity distribution obtained from the ERT data into the distribution of hydrate saturation requires an eligible relation considering the electrical properties of the present phases. During hydrate formation, the pore space is filled with two coexisting phases: the pore fluid of high electrical conductivity and hydrates, which can be considered to be an electrical insulator. Commonly, Archie's equations (Archie 1942) are used to determine the effective electrical properties in a multiphase system where the majority of the electrical charge transport is sustained by the pore fluid. Though we tested several mixing rules (Garnett-Maxwell 1904; Lichtenecker 1926; Landauer 1952; Waff 1974), we decided to use Archie's equations for two reasons: (1) the obtained results in our experimental setup should remain comparable to other published data sets which typically used Archie's equations; and (2) we found that applying Archie's equations yielded the most comprehensible results.

Thereby, we investigate Archie's equation in two different terms:

(i) Archie$_{var-phi}$ interprets the increasing hydrate phase as part of the (also non-conductive) sediment grain framework resulting in a decreasing porosity while hydrate saturation increases. The pore space, however, is completely fluid-saturated at all stages of hydrate saturation and the first Archie equation is used:

$$\rho = \frac{a}{(\Delta\phi)^m}\rho_{\mathrm{fl}} \tag{4}$$

where ρ is the bulk resistivity for a sample fully saturated with a fluid of resistivity ρ_{fl}. a and m are empirical parameters and were set to 1 and 1.5, respectively, according to the effective medium theory (Sen *et al.* 1981). $\Delta\phi$ is the varying porosity $\phi - \phi S_H$, depending on the degree of hydrate saturation S_H.

(ii) Archie$_{var-sat}$ interprets the increasing hydrate phase as a decrease of fluid saturation in the pore space. Thus, the porosity remains constant whereas the water saturation varies with different amounts of pore filling hydrate and the second Archie equation is used:

$$\rho = \frac{a}{\phi^m S^n}\rho_{\mathrm{fl}} \tag{5}$$

with

$$S = \frac{\phi - \phi S_H}{\phi} = 1 - S_H \tag{6}$$

where S is the pore water saturation depending on the degree of hydrate saturation and n is an empirical parameter (saturation exponent) set to 1.9386 (Pearson *et al.* 1983).

As the two Archie equations account for different parameters, the corresponding resistivities governing the degree of hydrate saturation differ as well. Fig. 1 shows the modelled resistivity evolution for

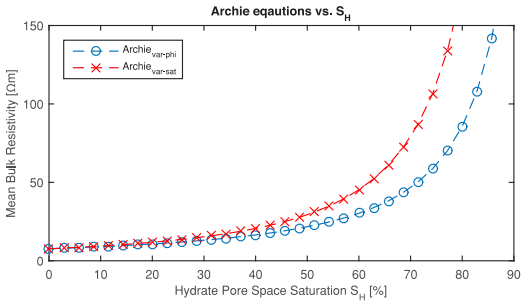

Figure 1. Modelled resistivity evolution of the two Archie interpretations Archie$_{var-phi}$ and Archie$_{var-sat}$ during hydrate saturation.

both Archie approaches within the experimentally covered hydrate saturation interval of 0–90 per cent.

To apply both Archie equations to the ERT data, we established the following data processing routine: In a first step, the inversion created a mesh dividing the sample volume into a total of 41 840 volume cells. Subsequently the inversion algorithm yielded resistivity data for a temperature of $T_M = 4$ °C for every single volume cell. Since the electrical resistivity varies with temperature the resistivity value of each cell was corrected against temperature to its reference value at $T_{\mathrm{Ref}} = 20$ °C. Rearranging both Archie approaches (eqs 4 and 5) for S_H, we were able to apply those relations to every single volume cell to estimate the local hydrate saturation.

The two Archie approaches were applied to the measured ERT data. Because the most significant differences among those mixing laws were expected at bulk hydrate saturation degrees of >50 per cent (see Fig. 1), we compared the results applying the different relations to the LARS RUN 2 data set of $S_H \approx 90$ per cent, which equals the highest saturation value in this experiment. (Fig. 2).

Both Archie approaches yielded comprehensible results. However, Archie$_{var-phi}$ generated a maximum local hydrate saturation value of 94.2 per cent, whereas Archie$_{var-sat}$ produced 88.9 per cent. At all stages of bulk hydrate saturation, Archie$_{var-phi}$ resulted in higher saturation values compared to those obtained with Archie$_{var-sat}$, with a difference always smaller than 10 per cent. As the maximum local hydrate saturation value generated by Archie$_{var-sat}$ was smaller than the reference bulk hydrate saturation obtained from pore fluid sampling, we considered Archie$_{var-phi}$ to yield the best results.

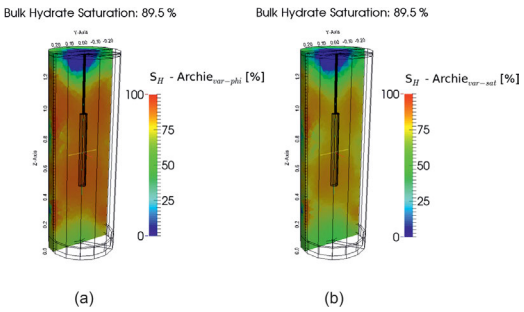

Figure 2. Application of the two Archie approaches to the final saturation stage of $S_H \approx 90$ per cent. Hydrate distribution obtained by applying (a) Archie$_{var-phi}$ and (b) Archie$_{var-sat}$.

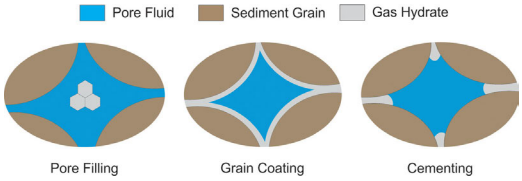

Figure 3. Illustration of pore filling, grain coating and cementing hydrate.

3.2 Permeability

The permeability as a material's hydraulic property is hard to capture using non-hydraulic measurement techniques. Generally, fluid flow is controlled by the interconnected pore space. In hydrate bearing sediments hydrate can affect both, the geometry of pores (pore-filling) and the interconnectivity of the sediments pore space, as hydrates formed at grain contacts might clog pore throats (grain coating, cementing) (Fig. 3).

Nevertheless, numerous approaches have been established to link the permeability to flow-affecting petrophysical parameters such as pore space geometry. The University of Tokyo introduced a very simple but effective relation to evaluate the permeability of a hydrate bearing sediment layer (Minagawa *et al.* 2005):

$$K(S_H) = K_0(1 - S_H)^N \tag{7}$$

with S_H being the fractional degree of hydrate saturation, K_0 the initial permeability at $S_H = 0$ and N being constant. Apart from S_H the only parameter affecting the permeability is the exponent N. Reported values for N range from 2.5 to 15 (Minagawa *et al.* 2005; Delli & Grozic 2013). It has been shown that values of N have to be chosen carefully to match experimental data and strongly depend on the investigated sediment. Since we do not have any experimental permeability data of the LARS sediment for the different stages of hydrate saturation, we are not able to identify a reasonable value for N, necessitating an alternative relation.

Another common approach relating the hydraulic permeability to petropysical parameters is the Carman-Kozeny (CK) relation (Carman 1956). CK originally relates the permeability to a geometric factor B, the porosity ϕ, the tortuosity τ and the specific surface area S (Mavko *et al.* 2003):

$$K = \frac{B\phi^3}{\tau^2 S^2}. \tag{8}$$

The CK relation can also directly be related to the degree of hydrate saturation (Kleinberg *et al.* 2003):

$$K(S_H) = K_0 \frac{(1 - S_H)^{n+2}}{(1 + \sqrt{S_H})^2} \tag{9}$$

where n is the saturation exponent with $n = 0.7S_H + 0.3$ (Spangenberg 2001; Delli & Grozic 2013). It should be noted that eq. (9) is only valid for pore filling hydrate formation, but not for hydrates coating the sediment grains or clogging pore throats (Fig. 3) (Kleinberg *et al.* 2003). Because the sediment's pore space in our experiments is completely water saturated at all times throughout hydrate formation and hydrates are formed from methane dissolved in the pore water, we assume to mimic the formation of natural, marine gas hydrates. Recent studies (Konno *et al.* 2015; Santamarina *et al.* 2015) carried out on natural sediment cores obtained from a methane hydrate reservoir in the Eastern Nankai Trough indicated from permeability and velocity measurements that natural, marine hydrates form and accumulate in the centre of the pores, justifying the assumption made by eq. (9).

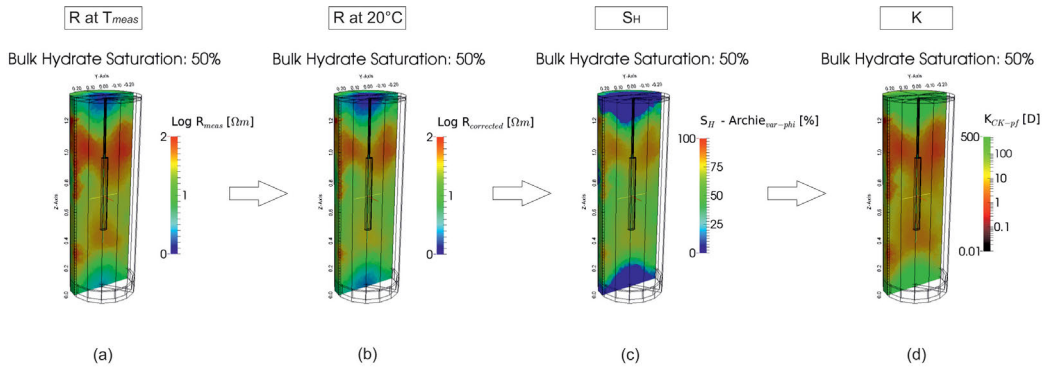

Figure 4. Illustration of the applied workflow to obtain the distribution of hydrate saturation and local permeability for a single measurement. (a) The inversion yielded the resistivity distribution at a temperature of 4 °C. (b) For comparability, the initial resistivity values got corrected against temperature to their reference value at 20 °C. (c) Those reference values were used to estimate local hydrate saturations S_H using Archie. (d) The determined S_H values were used as input data to estimate local permeability values.

Since the highly permeable sediment volume is very large, we unfortunately were not able to experimentally determine the initial permeability K_0 because the pressure gradients within the sediment were in the error range for the installed pressure sensors at low and intermediate bulk hydrate saturations. In a first order approximation, we therefore derived the initial permeability K_0 by applying empirical approaches considering the sample's grain size distribution (Hazen 1893; Terzaghi 1955). As the resulting permeability values covered several orders of magnitude, we chose to determine the sediment's K_0 at ambient pressure and temperature by conducting a Darcy fluid flow experiment. The resulting permeability was $K_0 = 673 \pm 11$ *D*. Since the experiments in LARS were run at a differential pressure of 4 MPa, the sediment's pore space experienced compaction and grains possibly cracked. Taking this into account, we set the initial permeability to $K_0 = 500$ *D*.

Regarding the data structure, the permeability value of each volume cell was determined using the (previously obtained) S_H value of the respective volume cell (see Section 3.1) in eq. (9). The described workflow is illustrated in Fig. 4.

4 RESULTS

4.1 Hydrate formation

During LARS RUN 2, a maximum bulk hydrate saturation of ≈90 per cent was reached at a constant pore pressure of 11 MPa. The fourteen temperature sensors (11 operating, 3 broken) were spatially distributed in the sediment sample to allow for the identification of the spatial extend of the hydrate stability zone within the specimen. The positioning of the PT100 sensors is shown in Fig. 5. We started the experiment by circulating the methane-loaded saline pore fluid from top to bottom.

Fig. 5 shows the temperature profiles of the sensors T1–T4 for the first four weeks of the hydrate formation experiment with the dashed line marking the hydrate stability temperature of 13.3 °C at given pressure. The Roman numbers mark the pore fluid injection periods. As long as no fluid was injected, the reservoir's base-temperature was defined by the confining temperature ($T_{\text{conf}} = 4$ °C). The methane-loaded brine entered from the top of the sample at a temperature slightly above hydrate stability conditions (≈16 °C)

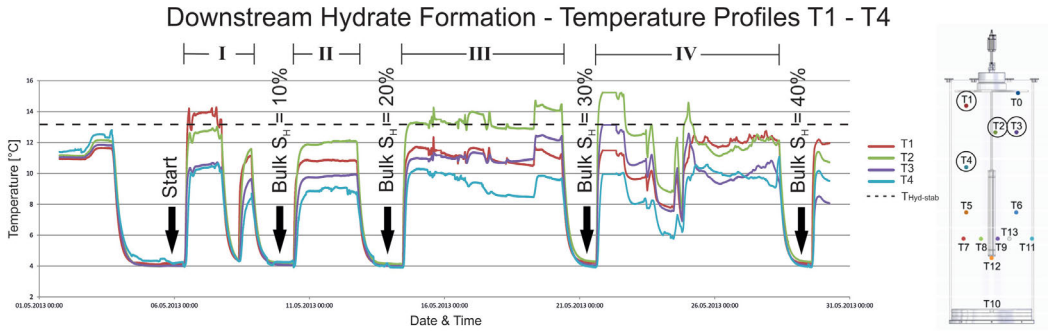

Figure 5. Temperature profiles of the sensors T1–T4 during hydrate formation from downward fluid flow with a sketch of LARS and the positions of the temperature sensors on the right. Roman numbers mark the intervals of pore fluid injection. The methane-loaded brine entered the sample at a temperature of ≈16 °C and was cooled down due to active cooling from the surrounding (4 °C). The hydrate stability temperature of 13.3 °C at 11 MPa is marked with the dashed line. The rapid temperature drops to 4 °C between two injection intervals were due to the stoppage of fluid circulation to let the sample thermally equilibrate for ERT data processing.

and cooled down until hydrate stability temperature was reached while circulated through the sediment due to the active cooling from the surrounding. During the first pore fluid injection period, the highest temperatures (≈14 °C) were recorded at sensor T1, as the injected pore fluid reached this sensor first. After each injection period, the fluid circulation was stopped to let the sediment sample equilibrate thermally. During the second injection period, the highest temperatures were recorded at sensor T2, indicating that the comparably warm pore fluid did not reach sensor T1 as much as before. The decrease in heat supply was caused by hydraulic constraints due to the formation of a solid hydrate phase at the very top of the reservoir around sensor T1. During the third and fourth injection period, sensor T1 displayed temperatures even lower than T3, suggesting continuous hydrate formation at T1 while T3 was located in the fluid path. The temperature sensor T4 almost continuously recorded the lowest temperatures, as the injected pore fluid was cooled down until it reached T4. Thus, the cooling from the surrounding exceeded the heat supply from the pore fluid. As the temperatures at T4 were always within the hydrate stability field, the majority of the supplied methane is assumed to be bound in hydrate before it could reach T4. Temperatures recorded at a sensor located in the centre of the sample (T2) where higher at all times and suggested that hydrates predominantly formed in the boundary regions of the sample, where cooling was strongest. Following the first injection period the temperatures recorded at T2 were continuously higher than those recorded in the boundary regions (T1, T3, T4), indicating an elevated heat supply from the injected pore fluid. Whereas the elevated driving forces (lowest temperature) close to the wall urged hydrate to form and to hydraulically constrain the fluid pathways, the centre of the sample still experienced sufficient heat supply to maintain pathways for the injected fluid.

Hydrate formation in the top boundary regions during downward fluid circulation could be confirmed by ERT measurements. Fig. 6 presents the evolution of spatial hydrate distribution and local permeability changes for the entire hydrate formation experiment applying the Archie$_{var-phi}$ and CK relation, respectively. It should be noted that the top and bottom 15 cm in the ERT-figures are not covered by electrodes and thus constitute an extrapolation of the inversion algorithm. At the very beginning of the experiment uniform hydrate saturations of 0–5 per cent were observed. During the following saturation stages, the majority of the hydrate phase formed in the upper 60–70 cm of the sediment sample. At a bulk hydrate saturation of 40 per cent calculated from the pore water conductivity measurements, hydrate began to form in lower regions of the sample while areas in the top of the reservoir showed hydrate saturations in the order of ≈80 per cent. To avoid hydraulic clogging at the top of the sample, the fluid circulation direction was switched from downwards to upwards. This led to an immediate increase of local hydrate saturation in the lower regions of the sample. Subsequently, hydrate formation advanced until almost the entire sample showed high saturation values. At the final saturation stage of 89.5 per cent the fluid pathways in the sediment were almost clogged and the fluid circulation was switched off.

Eq. (9) shows that the permeability is directly linked to the local hydrate pore space saturation. Accordingly, the changes of local permeability strongly correlate with the changes in local hydrate saturation. At the beginning of the hydrate formation experiment an almost homogeneously distributed permeability of 500 *D* was observed, which is just the predefined K_0. The subsequent hydrate formation in the upper part of the reservoir reduced the permeability in the respective areas. When we switched the pore fluid's flow direction at a bulk hydrate saturation of 40 per cent, permeabilities were in the order of 10^1 *D* in the upper part of the reservoir. The reversed fluid flow increased hydrate pore space saturation in the lower parts of the reservoir, further reducing the permeability of the affected area. At the final stage of $S_H = 89.5$ per cent the minimum permeability value generated by applying CK was $K_{\min} \approx 28.8$ *mD*.

During the LARS RUN 4 formation experiment we generally observed similar formation patterns. By slightly increasing the pore fluid injection velocity at the beginning of the experiment, the hydrate stability isotherm (again 13.3 °C at 11 MPa) was shifted towards the centre of the specimen, so that initial hydrate formation was observed much more centric as in LARS RUN 2. Because both experiments yielded very high bulk hydrate saturation values at the final stage, the final hydrate distribution for both experiments appeared very similar (Fig. 7).

4.2 Hydrate dissociation

During hydrate dissociation it is not possible to clearly identify all present phases by only measuring the electrical properties, since both, the emerging free gas phase and the remaining gas hydrates, are electrically isolating. The ERT only discriminates between areas of conductive and non-conductive pore space. Please note, that the ERT images recorded during hydrate dissociation therefore do not show the colour-coded hydrate saturation, but the electrical resistivity in a log scale. For a detailed interpretation, it is therefore necessary to include additional data such as temperature, pressure, and fluid flow.

The hydrates formed in LARS RUN 2 (see Fig. 6) were dissociated by pressure reduction in two stages: (1) simulating the 2008 production test in Mallik, Mackenzie Delta, Canada via depressurization in three steps (e.g. Wright *et al.* 2011) at 7.0 MPa–5.0 MPa–4.2 MPa (see Fig. 8) followed by (2) depressurization to atmospheric pressure (see Fig. 9). To simulate the Mallik production test, the surrounding temperature was set to 11 °C and reservoir pressure was initially set to 11.5 MPa (Uddin *et al.* 2011). Noteworthy, what had been an active cooling (4 °C) from the surrounding during hydrate formation turned into an active heating during hydrate dissociation.

The experiment started with *P–T* conditions deep within the hydrate stability field (at 11 °C $P_{\text{stab}} = 8$ MPa). The first pressure reduction to 7 MPa induced an immediate temperature decrease of ≈1.6 °C due to endothermic gas hydrate dissociation (Fig. 8). The resulting temperature of 9.4 °C already fell below the surrounding temperature and corresponded to the hydrate stability temperature at given pressure (7 MPa). After the second depressurization to 5 MPa (≈3 hr), the temperature profile of T0 clearly displayed temperatures outside the hydrate stability field ($T_{\text{stab}} = 6.1$ °C at P = 5 MPa) indicating complete hydrate dissociation at the top of the reservoir. Unfortunately, the ERT inversion results did not yield reliable information about this specific area as the top 15 cm of the sample are not covered by electrodes. All other temperature profiles dropped to the hydrate stability temperature at given pressure, suggesting that the front of hydrate decomposition was initiated at the top end face of the sediment sample. During the third pressure reduction (4.2 MPa) the temperature close to the neoprene jacket (T11) increased (Fig. 8). This temperature increase indicated that the endothermic process of hydrate dissociation could not compensate the heat supply from the surrounding (11 °C) anymore. Due to the decreased hydrate content hydrate decomposition declined. The ERT inversion results of the regions close to the neoprene jacket after 6 h showed areas of considerably lower resistivity. As both,

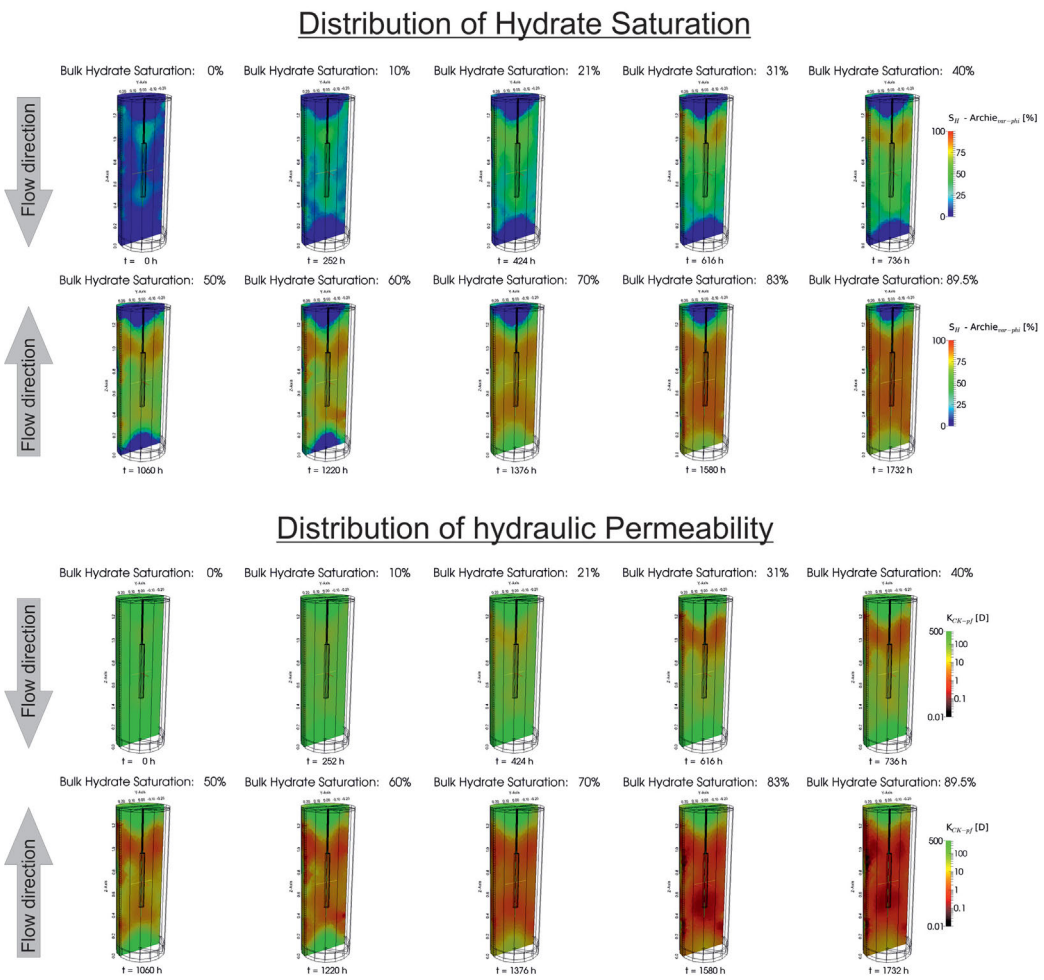

Figure 6. Results estimating the local hydrate saturation and permeability in the sediment sample applying Archie$_{var-phi}$ and CK to the ERT data. At a bulk hydrate saturation of 40 per cent, the pore fluid flow direction was switched to avoid clogging of the fluid flow paths as local hydrate saturations in the upper part of the reservoir reached 80 per cent. Generally, permeability decreases as hydrate saturation increases. At the stage of maximum bulk hydrate saturation, a minimum permeability value of $K_{\min} \approx 28.8$ mD was found.

hydrate and free gas, increase the electrical resistivity, the low resistivity values suggested completed hydrate dissociation and methane gas depletion in these regions (Fig. 8).

After 8 hr, the outlet was closed overnight. The reservoir temperature slowly adjusted to the surrounding temperature and the reservoir pressure increased to reach the hydrate equilibrium pressure of ≈8 MPa at 11 °C. Though the system was closed for 16 hours, the time was not enough for the reservoir to reach the equilibrium temperature of 11 °C. Due to the heat supply from the surrounding, hydrates continued to dissociate. Whereas the released gas phase increased the reservoir pressure, the endothermic nature of hydrate dissociation cooled the sample from the interior. Because hydrate dissociation continued as long as the PT conditions within the reservoir fell below the stability conditions of ≈8 MPa at 11 °C, the continuing cooling from the sample's interior delayed the temperature increase of the reservoir. The depressurization to atmospheric pressure was conducted from 24 hr onwards (Fig. 9).

The rapid pressure drop to 0.1 MPa set the entire sediment sample out of the hydrate stability field. This was followed by a significant temperature drop due to rapid hydrate dissociation, leading to temperatures below the freezing point in the centre of the sample. Both, the ERT inversion results and the corresponding temperature profiles of T4, T9 and T12 showed the formation of ice in the centre of the sample (Fig. 9). Subsequently, the temperatures at all sensors continuously increased to adjust with the surrounding temperature of 11 °C. After ≈35 hr all temperatures were above the freezing point, suggesting that only water and free gas remained in the pore space. Thus, the remaining high resistivity areas in the ERT inversion results were caused by free gas trapped in of the sediment sample.

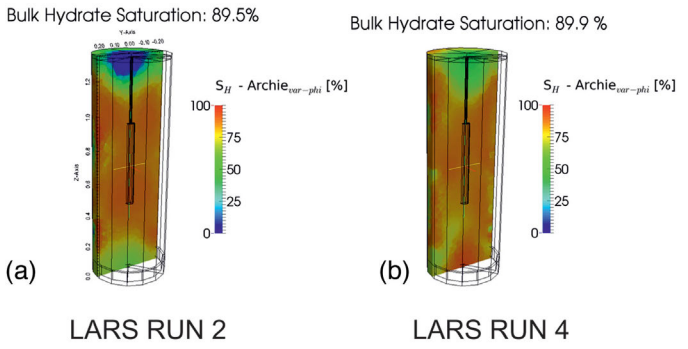

Figure 7. Final hydrate distributions at the end of the hydrate formation experiments of LARS RUNs 2 and 4.

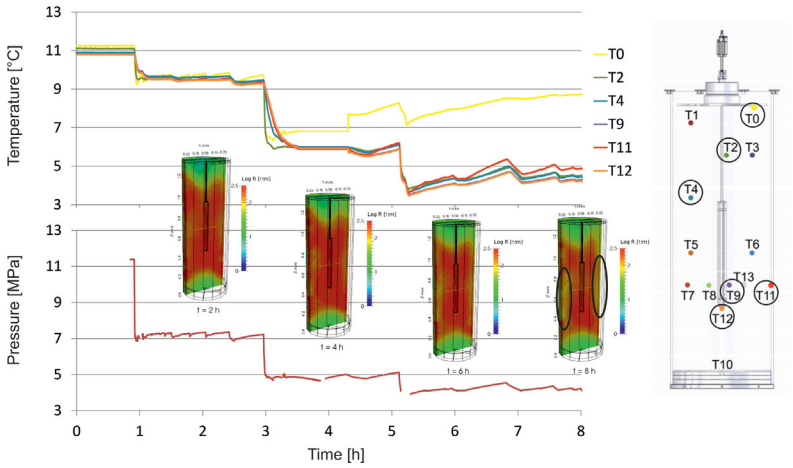

Figure 8. Overview of the first 8 hr of LARS RUN 2 depressurization. The conducted pressure levels are shown in the lower chart. The corresponding temperature profiles are shown in the upper chart and a sketch of LARS including the positions of the temperature sensors is given on the right. Depressurization was initialized by pressure reduction at the reservoir's top outlet. The temperature increase at T0 from the end of the first pressure step (≈2 hr) onwards indicates that hydrates at the very top were dissociated. From ≈4 hr onwards, the temperature at T11 starts to increase, indicating that the heat supply from the surrounding exceeded the energy loss caused by endothermic hydrate dissociation. The corresponding ERT inversion results also suggest hydrate dissociation in the boundary regions (black ellipses).

The hydrate phase formed during LARS RUN 4 was decomposed via depressurization as well, applying the same surrounding temperature (11 °C) and pressure levels as in LARS RUN 2 with an additional 3 MPa pressure level (Stage 1: 7.0 MPa–5.0 MPa–4.2 MPa–3 MPa; Stage 2: to P_{atm}). Because the experimental setup of LARS RUN 4 featured optical temperature measurements using a meandering DTS coil within the sediment sample, the number of temperature measurement points was significantly increased. However, as each data point provided by the DTS system constituted a mean temperature value for a 0.5 m interval it was necessary to evaluate the accuracy of the obtained DTS data. Therefore, three PT100 sensors were additionally placed on the cylindrical heat reactor in the centre of the sample. To investigate the comparability of both measurement techniques it was reasonable to evaluate the temperature data recorded during the decomposition experiments, as the various pressure drops induced much more significant temperature changes compared to those during the hydrate formation experiments. Fig. 10 presents the temperature data recorded at the PT100 sensor at the bottom of the heat exchange reactor (T0, blue) together with the DTS data obtained by the measurement interval corresponding to DTS point 19 (red) for the first 16 hr of the dissociation experiment. Because the measurement interval of DTS point 19 radial symmetrically surrounded the T0 sensor, the measured temperatures at those two points should be similar. With a recorded maximum deviation of 0.3 °C (in Fig. 10 at ≈3 hr) we considered the DTS data to give a good reflection of the temperature distribution within the sediment sample. Based on the obtained DTS data it was possible to extensively display the temperature evolution in the sediment sample during the LARS RUN 4 dissociation experiment.

At the first depressurization stage with the applied pressure levels of 7, 5, 4.2 and 3 MPa both the ERT and the temperature recordings yielded very similar dissociation patterns as observed in LARS RUN 2. Hydrate dissociation initiated at the top and in the boundary regions, where the pressure and temperature gradients were the highest. Subsequently, the dissociation front migrated towards the centre of the sample. Each pressure drop was accompanied by a

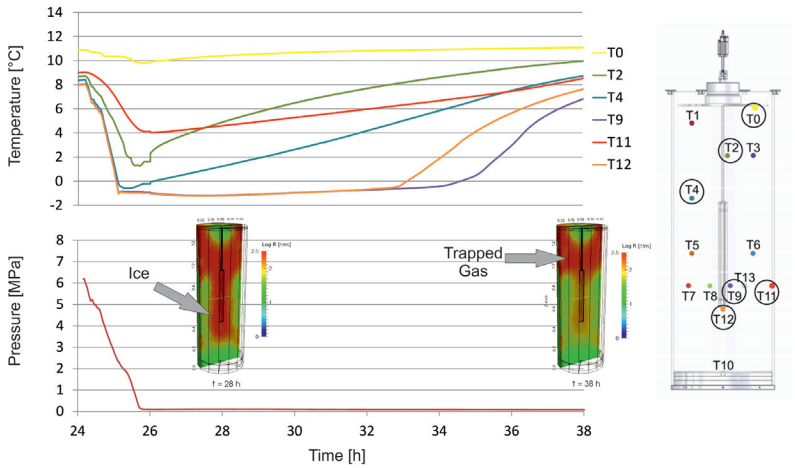

Figure 9. Continuation of LARS RUN 2 depressurization. During overnight valve closure, the reservoir pressure increased to the equilibrium pressure at 11 °C of 8 MPa. The depressurization was conducted to atmospheric pressure. Starting after ≈25 hr, the temperature profiles and ERT inversion results show that the centre of the sediment sample was frozen due to the rapid pressure drop accompanied by significant cooling. At this state, the boundary regions seem to be completely free hydrate and gas. At the final stage (38 hr), *P*–*T* conditions in the entire sediment sample were out of the hydrate stability field. The remaining high-resistivity areas in the ERT inversion results were caused by free gas which remained trapped in the upper parts of the sediment sample.

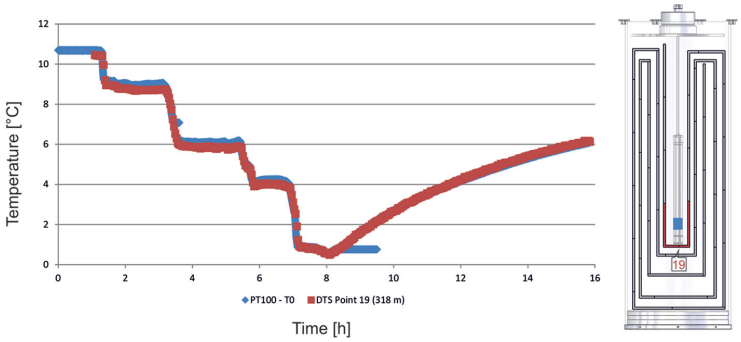

Figure 10. Comparison of the temperature data recorded by the PT100 sensor placed at the button on the heat exchange reactor (blue) in the centre of the sample and the DTS data obtained by the respective measurement interval of DTS point 19 (red).

temperature drop into the respective hydrate stability temperature. This can be seen, for example, on the temperature distribution of the 5 MPa pressure level in both LARS RUNs 2 (Fig. 8) and 4 (Fig. 11), having a hydrate stability temperature of ≈6.1 °C. Similar to the observations made in LARS RUN 2 the boundary regions of the sample appear to be almost completely free of any hydrate or free gas phase after 8 hr (Fig. 11). After the first 8 hours of the dissociation experiment the outlet was closed overnight again. During that time the temperature within the sediment sample started to adjust to the surrounding temperature of 11 °C, accompanied by a respective pressure increase. The LARS RUN 4 depressurization to atmospheric pressure was conducted from 27 hr onwards. Approximately three hours later, the endothermic nature of hydrate decomposition cooled the centre of the sample to temperatures below the freezing point again, resulting in ice formation in the respective areas (Fig. 12). After ≈36 hr all recorded temperatures were above the freezing point suggesting that all hydrates were dissociated and only water and free gas remained in the pore space.

5 DISCUSSION

5.1 Mixing laws

The choice of a proper mixing rule is a crucial point in our data processing routine. It turned out that the evaluation of proper mixing rule is a trial-and-error procedure. The suitability of a mixing rule not only depends on quantitatively matching the reference bulk saturation values, but also on qualitatively producing comprehensible hydrate distributions (e.g. in terms of saturation-heterogeneities). To test the different mixing rules it was necessary to apply them all to the measured ERT data and validate both their quantitative and qualitative appropriateness. In doing so the best results were obtained using Archie approaches. While Archie$_{var-phi}$ and Archie$_{var-sat}$ were very consistent, the highest local saturation values generated by Archie$_{var-sat}$ still fell below the bulk hydrate saturation obtained from pore fluid sampling.

During the hydrate formation experiments, the reference bulk hydrate saturation was determined by frequent pore fluid analysis (see

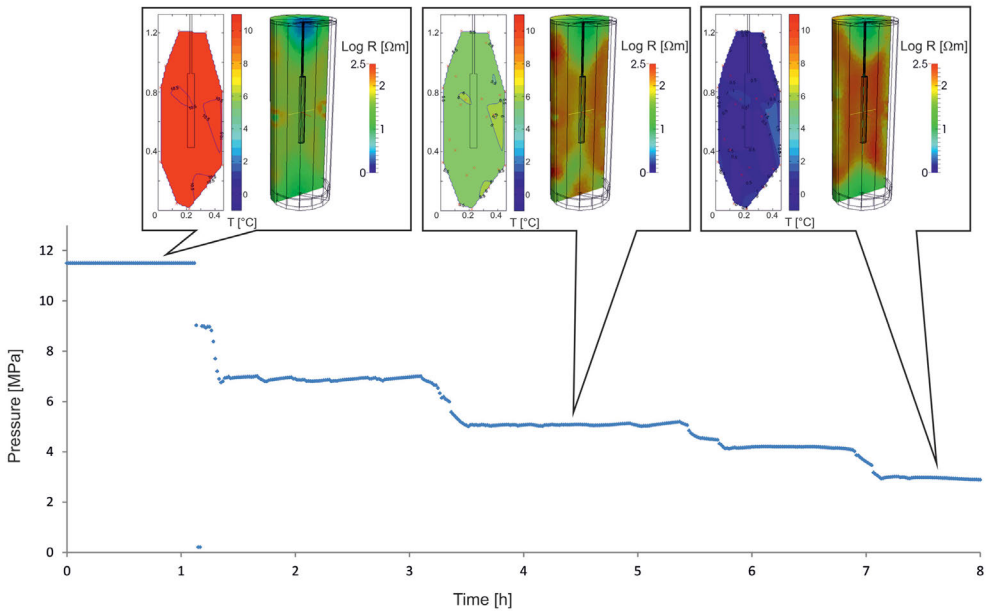

Figure 11. First 8 hr of LARS RUN 4 depressurization. The applied pressure drops to 7, 5, 4.2 and 3 MPa were accompanied by temperature drops to the respective stability temperature at given pressure (left in each balloon). Hydrate dissociation initiated at the top and the boundary regions of the sample. The latter appear to be methane-depleted after 8 hr.

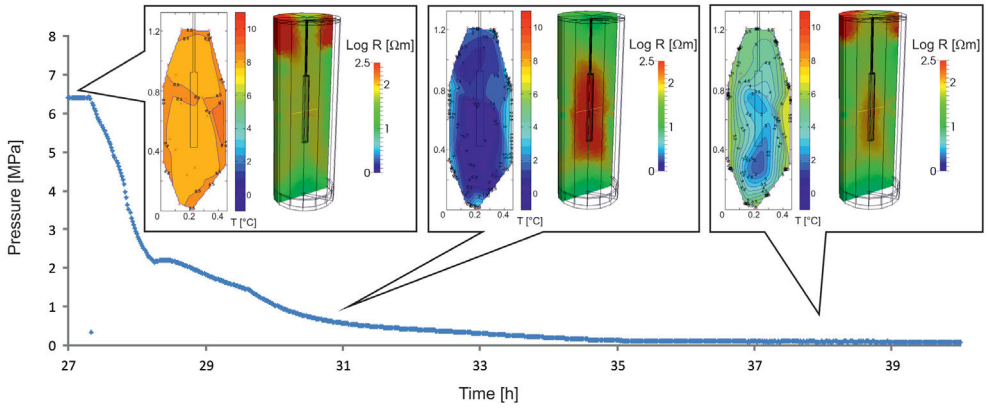

Figure 12. Continuation of LARS RUN 4 depressurization. During overnight valve closure, the reservoir temperature and pressure increased to adjust to the stability conditions at 11 °C. Due to the endothermic nature of hydrate decomposition, the depressurization to atmospheric pressure cooled parts of the sample to temperatures below freezing point again, resulting in ice formation.

paragraph 3.1). Since we applied Archie$_{var-phi}$ to the ERT data to determine local hydrate saturations, we could also determine values of bulk hydrate saturation from the ERT data. For this purpose the local hydrate content of all volume cells was summarized and related to the sediment's porosity. Comparing the bulk hydrate saturation values determined by pore fluid sampling and our ERT data processing routine was used to evaluate the quantitative eligibility of a mixing rule. Fig. 13 illustrates the evolution of the bulk hydrate saturation determined by applying Archie$_{var-phi}$ to the ERT data of LARS RUNs 2, 3 and 4 (solid lines) in relation to the reference values determined by pore fluid sampling (dashed line). It is evident that bulk saturations obtained by ERT data initially overestimated the reference bulk saturation by up to ≈10 per cent. Because the local saturation values were determined based on the measured resistivity distribution, the overestimated hydrate saturation had to be caused by increased resistivities obtained from the ERT. Closely looking on the initial hydrate distribution (0 per cent) in Fig. 6 shows that the majority of generated hydrate saturation is located right at the top and bottom of the implemented heat exchange reactor. Because the reactor was already fixed to the top cap of the pressure vessel

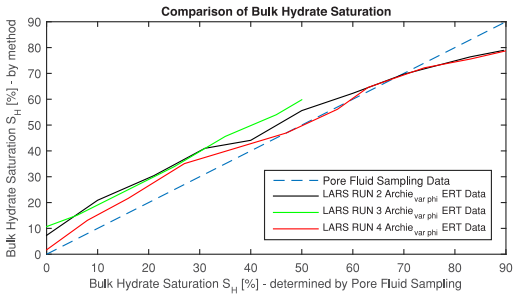

Figure 13. Comparison of bulk hydrate saturations determined by pore fluid sampling (blue dashed line) and bulk hydrate saturations obtained by applying Archie$_{var-phi}$ to the ERT data of LARS RUNs 2, 3 and 4 (solid black, green and red lines). The bulk hydrate saturation determined by pore fluid sampling is plotted on the *x*-axis and the bulk saturation determined for each method (pore fluid sampling and from ERT data) is plotted on the *y*-axis.

during the installation process, we therefore suggest that those areas experienced severe compaction during mounting. As a result, the porosity in the respective areas is suggested to be decreased, increasing the measured electrical resistivity and, thus, generated hydrate saturation in the ERT data.

For reference bulk saturation values exceeding 40 per cent, the bulk saturations obtained from ERT data of LARS RUNs 2 and 4 approximate the reference baseline. The LARS RUN 2 and 4 curves finally fell below the reference baseline at ≈70 per cent. Having such high degrees of bulk hydrate saturation, the possibility of hydrate forming hydraulic caps has to be considered. In such a case some water volume would be trapped and cut off from the circulation. The remaining water used for pore fluid sampling would subsequently overestimate the salinity within the sample, producing higher pore fluid sampling saturation values. In that case, the bulk saturation obtained from pore fluid sampling only yields an upper bound for a heterogeneous salinity distribution.

However, areas comprising a stable hydraulic sealing and trapping water should have been detectable in the ERT data, as the electrical properties in those areas would barely change over time. As visible in Fig. 6, such areas could not be identified. We assume that hydraulic caps might form during our hydrate formation experiments, but would last only for a relatively short time. The measured salinities during our formation experiments yielded an irregular increasing trend, giving evidences for the temporary existence of hydraulic sealings (Schicks *et al.* 2011). Spangenberg *et al.* (2015) emphasized that hydrates formed at high formation rates in LARS undergo recrystallization. If some areas were cut off from the circulation and, thus, from methane supply by solid hydrate caps, recrystallization is likely to re-establish the connection to the fluid circulation.

The underestimated saturation values obtained from the applied ERT data processing routine at high degrees of bulk hydrate saturation are therefore most likely caused by applying the Archie$_{var-phi}$ relation to the ERT resistivity data. Following eq. (4), a constant value for the exponent m (also referred to as cementation exponent) was used throughout all saturation stages. Because Archie$_{var-phi}$ interprets the increasing hydrate phase as part of the grain framework, a wide range of porosities are covered during our hydrate formation experiments. Since numerous studies considered m to be porosity dependent (e.g. Neustaedter 1968), efforts are required for future work to quantitatively determine appropriate Archie parameters throughout the entire range of bulk saturation achieved in our experiments. The same would be true for Archie$_{var-sat}$, because the saturation exponent might not be constant over the full saturation range, but depend on saturation (e.g. Spangenberg 2001; Spangenberg & Kulenkampff 2006).

However, since the saturation values determined by applying Archie$_{var-phi}$ qualitatively and quantitatively produced comprehensible results we consider them to follow the real distribution of local hydrate saturation, though the exact saturation values may differ by several percent.

5.2 Permeability

Based on the workflow presented in Fig. 4, local permeability changes could be estimated from the ERT data. The obtained resistivity distribution was converted into the spatial hydrate distribution, which served as input data for the CK relation (eq. 9). To evaluate the permeability estimates based on the ERT data, we averaged all local permeability values obtained during LARS RUNs 2 and 3 and compared them with modelled data derived from the CK equation (red dashed in Fig. 14). The LARS RUN 4 permeability data could not directly be related to the LARS RUNs 2 and 3 data sets since a different sediment sample with a much higher initial permeability K_0 was used. It is therefore not plotted in Fig. 14. The modelled permeability evolution of the CK relation yields a satisfactory fit for bulk hydrate saturations smaller 30 per cent. For bulk hydrate saturations exceeding 30 per cent, the permeability evolution obtained from the ERT data workflow increasingly overestimated the modelled permeability evolution. Unfortunately it was not possible to verify the estimated permeability distribution with measured values. Since the highly permeable sediment volume is very large, the pressure gradients within the sediment were in the error range for the installed pressure sensors at low and intermediate bulk hydrate saturations, so that it was not possible to directly measure the hydraulic bulk permeability during the experiments in LARS. Only one bulk permeability measurement could be carried out at the final stage of LARS RUN 2 ($S_H = 89.5$ per cent) with $k_{\min} = 5$ *mD* (green cross in Fig. 14). At this stage the obtained permeability overestimated the modelled CK relation by 2 orders of magnitude and the single measured data point by 3 orders of magnitude. Those deviations are most probably due to several reasons:

(i) The modified CK equation (eq. 9, red dash in Fig. 14) used in our workflow is a very simple equation which only considers

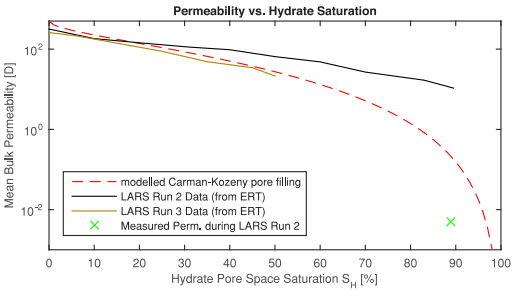

Figure 14. Comparison of modelled permeability (dashed line) and mean bulk permeabilities obtained during LARS RUNs 2 and 3 (solid brown and black lines) applying the introduced workflow.

the degree of hydrate saturation and neglects all sediment specific parameters. Subsequently, a homogeneous sediment sample as well as a homogeneous hydrate distribution are assumed, which is not the case in the LARS experiments (Fig. 6). Furthermore, deviations from ERT based S_H estimates consequently caused deviations in the permeability estimates, as S_H was the only input parameter in the CK relation.

(ii) Averaging anisotropic, heterogeneous data has to be carried out carefully. To pay tribute to direction-dependencies the single values can be interpreted as 'parallel connection' as well as 'series connection' requiring either the arithmetic or the harmonic mean. Furthermore the style of averaging significantly affects the resulting permeability evolution. For simplicity we averaged the obtained permeability data as a series connection by using arithmetic mean values. Using, for instance, harmonic mean values would cause the estimated permeability evolution to significantly underestimate the CK relation. Because the bulk hydrate saturation yielded by the ERT data workflow already underestimated the bulk saturation obtained from pore fluid sampling (see Fig. 13), this is most likely not the case.

(iii) The measured data point at $S_H = 89.5$ per cent constitutes the lower bound of the bulk permeability at this saturation stage. The experimentally obtained bulk permeability was determined by considering the differential pressure between the fluid inlet and outlet (at the sample's top and bottom). Thus, the experimentally measured permeability value was much more sensitive to plugging (due to sediment input and/or gas hydrate) in the capillaries, which generally reduces the measured permeability.

Though the estimated permeability values might show significant deviations, this information is valuable to qualitatively follow the permeability distribution during the formation experiments. Furthermore the obtained permeability distribution constitutes a helpful tool to adjust dissociation experiments.

5.3 ERT monitoring of hydrate formation and dissociation

Hydrate formation and dissociation were successfully monitored using ERT. The large contrasts in electrical properties between the coexisting pore filling phases granted hydrate localization even at low saturation.

During hydrate formation, ERT imaging and the recorded temperature profiles indicated that hydrate formed quickly within the sediment sample after reaching hydrate stability conditions. We modelled the temperature field within the sediment sample assuming an undisturbed fluid flow field (no hydrates present) using COMSOL Multiphysics (V. 4.3b) to identify the initial spatial extent of the hydrate stability field (Fig. 15). Fig. 15 shows the LARS RUN 2 resistivity distribution at a bulk hydrate saturation of 40 per cent (left) with the modelling results (right). The most significant resistivity increase occurred just after the injected pore fluid enters the hydrate stability field at a temperature of 13.3 °C. Evidently, the majority of the injected methane was consumed within hydrate formation as soon as it migrated into the hydrate stability field. The geometry and the spatial extent of the hydrate stability field thereby depend on the flow velocity and the temperature of the injected methane-loaded brine. However, by changing the flow velocity of the injected fluid and thus by shifting the hydrate stability temperature during the hydrate formation experiment of LARS RUN 4, the ERT and temperature recordings suggested that we have great

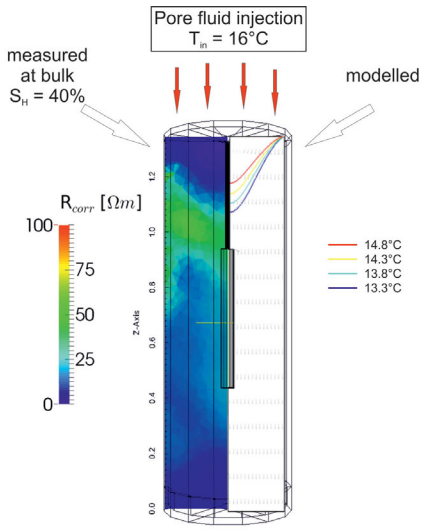

Figure 15. Comparison of measured resistivity distribution during LARS RUN 2 at a bulk hydrate saturation of 40 per cent (left) and the modelled temperature field resulting from active cooling from the surrounding (4 °C) and injection at the top end face of relatively warm pore fluid (≈16 °C). The isotherm of 13.3 °C marks the boundary of the hydrate stability field at 11 MPa.

control of the spatial extent of the hydrate stability field within the sediment sample.

Capturing the spatial distribution of remaining hydrates and free gas during hydrate dissociation is difficult. Both phases appear as electrically non-conductive, and therefore cannot be distinguished by only measuring the electrical properties of the pore filling. However, adding temperature and pressure data enables advanced interpretation of hydrate dissociation experiments in LARS.

Hydrate dissociation initialized at the top of the sediment sample, where the pressure gradient was highest. Subsequent hydrate dissociation was predominantly measured at the boundary regions of the sample, where the heat supply from the surrounding led to temperatures exceeding the hydrate stability temperature at given pressure. The ERT data identified the high-resistivity areas filled with hydrate and/or gas. We observed considerable resistivity increases in areas featuring active hydrate dissociation and, thus, gas release compared to areas exclusively filled with gas hydrate (Fig. 16). For pore filling hydrates, a water shell adsorbed at the sediment grain remains for $S_H < 1$ (Spangenberg 2001; Kuhs *et al.* 2014). The expanding free gas phase arising due to hydrate dissociation pushed this remaining pore water out of the pores, increasing the electrical resistivity. Thus, electrical measurements also enable to identify the onset of hydrate decomposition in the sediment's pore space.

6 SUMMARY AND CONCLUSION

The electrical properties of methane-hydrate bearing sediments were investigated during hydrate formation and dissociation experiments using an ERT array in the large reservoir simulator LARS. For the first time, it was possible to qualitatively visualize the occurring hydrate phase during hydrate formation experiments in LARS. The ERT measurements showed that hydrate formation started as soon

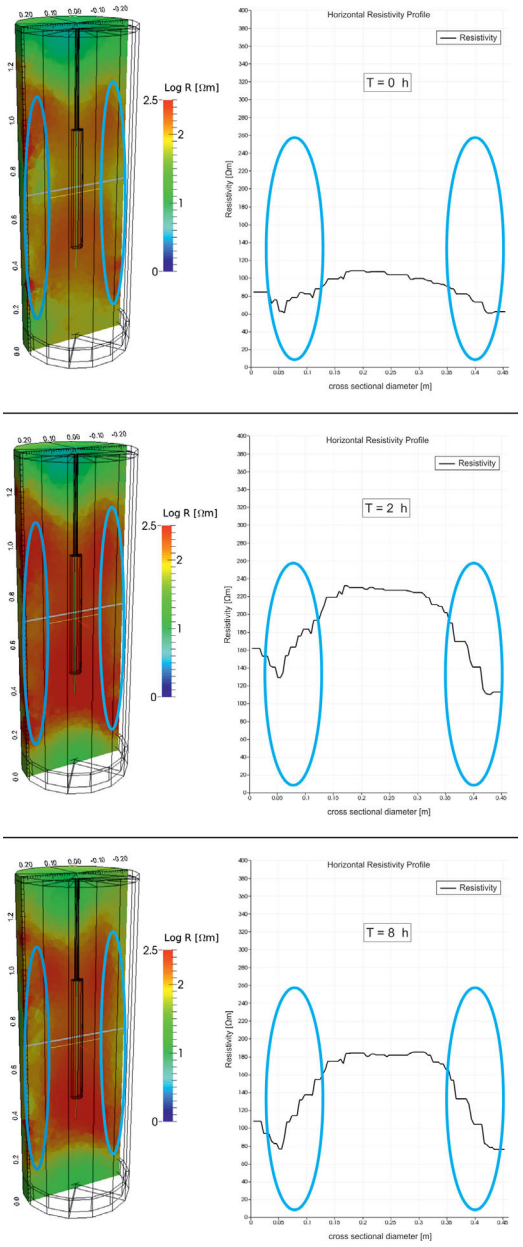

Figure 16. Horizontal resistivity profiles (grey line in left picture) for different states of hydrate dissociation. Top: initial resistivities before hydrate dissociation (only hydrate, no gas present). Middle: occurring hydrate dissociation. Emerging free gas phase increases resistivities along the profile (hydrate and gas present). Bottom: resistivities in the boundary region decrease again, indicating completed hydrate dissociation and advancing gas depletion (no hydrate, only gas present).

as the super saturated pore water entered the hydrate stability field in terms of *P–T* conditions. This leads to the conclusion that the residence time of dissolved methane in gas hydrate stability zones is short until it is consumed in hydrate formation.

Furthermore, we introduced a data processing routine which allowed the quantification of local changes of hydrate saturation and hydraulic permeability by measuring the electrical properties of the sediment sample. The spatial resistivity distribution obtained from the ERT data was converted into a quantitative spatial distribution of hydrate saturation by applying the Archie$_{var-phi}$ relation. The resulting information about the hydrate distribution can subsequently serve as input data for numerical simulations, for example, modelling production scenarios and history matching of experiments in LARS, or to adjust future dissociation experiments in LARS with respect to the obtained hydrate distribution.

The values of local hydrate saturation were used to estimate the local changes of hydraulic permeability within the sediment sample using the pore filling CK relation. The estimated permeability evolution yields helpful information in terms of understanding the changes of the sediment's hydraulic properties. Future plans involve additional experimental efforts to support the applied models with experimental permeability data.

During hydrate dissociation it could be shown that the gas and hydrate phases can qualitatively be monitored and tracked using ERT data. After setting the *P–T* conditions outside of the hydrate stability field, areas of increased electrical resistivity marked initialized hydrate decomposition, as the emerged free gas phase displaced remaining pore water of the respective areas. Supplemental temperature and pressure data allowed for advanced interpretation in terms of identifying areas of active hydrate dissociation as well as areas completely free of non-dissolved hydrocarbons.

The general alikeness of the data recorded during LARS RUNs 2 and 4 indicates that the results of our hydrate formation and dissociation experiments in LARS are reproducible.

ACKNOWLEDGEMENTS

The German Federal Ministry of Economy and Technology provided funding for this work within the SUGAR project through Research Grant 03SX250E.

Furthermore, the authors thank the staff of the GFZ workshops, Alexander Reichardt and Ronny Giese for invaluable technical help and for the construction of the ERT system.

REFERENCES

Archie, G.E., 1942. The electrical resistivity log as an aid in determining some reservoir characteristics, *Petroleum Transactions of AIME,* **146,** 54–62, doi:10.2118/942054-G.

Bauer, K., Haberland, C., Pratt, R., Hou, F., Mediali, B. & Weber, M., 2005. Ray-based cross-well tomography for P-wave velocity, anisotropy, and attenuation structure around the JAPEX/JNOC/GSC et al. Mallik 5L-38 gas hydrate production research well, *Geological Survey of Canada,* Bulletin 585, 21 p.

Buffett, B. & Zatsepina, O., 2000. Formation of gas hydrate from dissolved gas in natural porous media, *Mar. Geol.,* **164,** 69–77.

Carman, P., 1956. *Flow of Gases Through Porous Media,* Academic Press.

Dallimore, S.R. & Collett, T.S., 2005. Scientific results from the Mallik 2002 gas hydrate production research well program, Mackenzie Delta, Northwest Territories, Canada, *Geological Survey of Canada Ottawa,* Bulletin 585, doi:10.4095/220702.

Delli, M. & Grozic, J., 2013. Prediction Performance of Permeability Models in Gas-Hydrate-Bearing Sands, *SPE Journal, Society of Petroleum Engineers,* **18,** 274–284.

Ersland, G., Husebø, J., Graue, A. & Kvamme, B., 2009. Transport and storage of CO_2 in natural gas hydrate reservoirs, *Energy Procedia,* **1,** 3477–3484.

Garnett, J.C.M., 1904. Colours in metal glasses and in metallic films, *Phil. Trans. R. Soc. Lond., A.,* **203,** 385–420.

Günther, T., Rücker, C. & Spitzer, K., 2006. Three-dimensional modelling and inversion of dc resistivity data incorporating topography - II. Inversion, *Geophys. J. Int.,* **166,** 506–517.

Hazen, A., 1893. Some Physical Properties of Sands and Gravels with Special Reference to their Use in Filtration, *24th Annual Report, Massachusetts State Bureau of Health,* Publ. Doc. 34, 539–556.

Klauda, J.B. & Sandler, S.I., 2005. Global distribution of methane hydrate in ocean sediment, *Energy & Fuels,* **19,** 459–470.

Kleinberg, R.L., Flaum, C., Griffin, D.D., Brewer, P.G., Malby, G.E., Peltzer, E.T. & Yesinowski, J.P., 2003. Deep sea NMR: methane hydrate growth habit in porous media and its relationship to hydraulic permeability, deposit accumulation, and submarine slope stability, *J. geophys. Res.,* **108**(B10), 2508, doi:10.1029/2003JB002389.

Kneafsey, T.J., Tomutsa, L., Moridis, G.J., Seol, Y., Freifeld, B.M., Taylor, C.E. & Gupta, A., 2007. Methane hydrate formation and dissociation in a partially saturated core-scale sand sample, *Journal of Petroleum Science and Engineering,* **56,** 108–126.

Konno, Y. *et al.*, 2015. Permeability of sediment cores from methane hydrate deposit in the Eastern Nankai Trough, *Mar. Pet. Geol.,* doi:10.1016/j.marpetgeo.2015.02.020.

Kuhs, W.F. *et al.*, 2014. In-situ micro-structural studies of gas hydrate formation in sedimentary matrices, in *Proceedings of the 8th International Conference on Gas Hydrates ICGH 2014,* Beijing, China, pp. T1–122.

Kvenvolden, K.A. & Grantz, A., 1990. Gas hydrates of the Arctic Ocean region, in *The Geology of North America 50, The Arctic Ocean Region,* pp. 539–549, eds Grantz, A., Johnson, L. & Sweeney, J.F., Geological Society of America.

Landauer, R., 1952. The Electrical Resistance of Binary Metallic Mixtures, *J. Appl. Phys.,* **23,** 779–784.

Lee, W.S. & White, M., 2014. Guest molecule exchange kinetics for the 2012 Ignik Sikumi Gas Hydrate Field Trial, in *Offshore Technology Conference,* Houston, TX, USA.

Lichtenecker, K., 1926. Dielectric constant of artificial and natural mixtures, *Phys. Z,* **27,** 115–158.

Mavko, G., Mukerji, T. & Dvorkin, J.P., 2003. *The Rock Physics Handbook: Tools for Seismic Analysis of Porous Media,* Cambridge Univ. Press.

Milkov, A.V., Claypool, G.E., Lee, Y.-J. & Sassen, R., 2005. Gas hydrate systems at Hydrate Ridge offshore Oregon inferred from molecular and isotopic properties of hydrate-bound and void gases, *Geochim. Cosmochim. Acta,* **69,** 1007–1026.

Minagawa, H., Ohmura, R., Kamata, Y., Ebinuma, T., Narita, H. & Masuda, Y., 2005. Water permeability measurements of gas hydrate-bearing sediments, *Fifth International Conference on Gas Hydrates,* Trondheim, Norway, 1058.

Neustaedter, R., 1968. Log evaluation of deep Ellenburger gas zones, in *SPE Deep Drilling and Development Symposium,* Monahans, TX, USA.

Pearson, C.F., Halleck, P.M., McGuire, P.L., Hermes, R. & Mathews, M., 1983. Natural gas hydrate deposits: a review of in situ properties, *J. Phys. Chem.,* **87,** 4180–4185.

Priegnitz, M., Thaler, J., Spangenberg, E., Rücker, C. & Schicks, J.M., 2013. A cylindrical electrical resistivity tomography array for three-dimensional monitoring of hydrate formation and dissociation, *Rev. Sci. Instrum.,* **84,** 104502, doi:10.1063/1.4825372.

Rydzy, M.B., 2013. The effect of hydrate formation on the elastic properties of unconsolidated sediment, *PhD thesis,* Colorado School of Mines, Golden, CO.

Santamarina, J. *et al.*, 2015. Hydro-bio-geomechanical properties of hydrate-bearing sediments from Nankai Trough, *Mar. Pet. Geol.,* doi:10.1016/j.marpetgeo.2015.02.033.

Schicks, J.M., Spangenberg, E., Giese, R., Steinhauer, B., Klump, J. & Luzi, M., 2011. New approaches for the production of hydrocarbons from hydrate bearing sediments, *Energies,* **4,** 151–172.

Schicks, J.M., Spangenberg, E., Giese, R., Luzi-Helbing, M., Priegnitz, M. & Beeskow-Strauch, B., 2013. A counter-current heat-exchange reactor for the thermal stimulation of hydrate-bearing sediments, *Energies,* **6,** 3002–3016.

Schwalenberg, K., Haeckel, M., Poort, J. & Jegen, M., 2010. Evaluation of gas hydrate deposits in an active seep area using marine controlled source electromagnetics: results from Opouawe Bank, Hikurangi Margin, New Zealand, *Mar. Geol.,* **272,** 79–88.

Sen, P., Scala, C. & Cohen, M., 1981. A self-similar model for sedimentary rocks with application to the dielectric constant of fused glass beads, *Geophysics,* **46,** 781–795.

Sloan, E. & Koh, C., 2008. *Clathrate Hydrates of Natural Gases,* CRC Press.

Spangenberg, E., 2001. Modeling of the influence of gas hydrate content on the electrical properties of porous sediments, *J. geophys. Res.,* **106**(B4), 6535–6548.

Spangenberg, E. & Kulenkampff, J., 2006. Influence of methane hydrate content on electrical sediment properties, *Geophys. Res. Lett.,* **33,** L24315, doi:10.1029/2006GL028188.

Spangenberg, E., Priegnitz, M., Heeschen, K. & Schicks, J.M., 2015. Are Laboratory-Formed Hydrate-Bearing Systems Analogous to Those in Nature? *J. Chem. Eng. Data,* **60,** 258–268.

Stern, L.A., Kirby, S.H., Durham, W.B., Circone, S. & Waite, W.F., 2003. Laboratory synthesis of pure methane hydrate suitable for measurement of physical properties and decomposition behavior, in *Natural Gas Hydrate: Oceanic and Permafrost Environments,* pp. 323–348, ed. Max, M.D., Kluwer.

Terzaghi, K., 1955. *Influence of Geological Factors on the Engineering Properties of Sediments,* Harvard University.

Uddin, M., Wright, F. & Coombe, D., 2011. Numerical study of gas evolution and transport behaviours in natural gas-hydrate reservoirs, *J. Can. Pet. Technol.,* **50,** 70–88.

Von Stackelberg, M., Gotzen, O., Pietuchovsky, J., Wirtscher, O., Fruhbuss, H. & Meinhold, W., 1947. Struktur und Formel der Gashydrate, *Fortschr. der Mineralogie,* **26,** 122–124.

Waff, H.S., 1974. Theoretical considerations of electrical conductivity in a partially molten mantle and implications for geothermometry, *J. geophys. Res.,* **79,** 4003–4010.

Waite, W.F. & Spangenberg, E., 2013. Gas hydrate formation rates from dissolved-phase methane in porous laboratory specimens, *Geophys. Res. Lett.,* **40,** 4310–4315.

Wright, J.F., Uddin, M., Dallimore, S.R. & Coombe, D., 2011. Mechanisms of gas evolution and transport in a producing gas hydrate reservoir: an unconventional basis for successful history matching of observed production flow data, in *Proceedings of the 7th International Conference on Gas Hydrates ICGH 2011,* Edinburgh, Scotland.

Yamamoto, K., 2014. 2013 Methane hydrate offshore production test in the eastern Nankai Trough; a milestone on the path to real energy resource, in *Proceedings of the 8th International Conference on Gas Hydrates ICGH 2014,* Beijing, China, pp. T3–153.

4. Publication III: Are laboratory-formed hydrate-bearing systems analogous to those in nature?

Authors:

Erik Spangenberg, Mike Priegnitz, Katja Heeschen, and Judith M. Schicks

Published as:

Spangenberg, E., Priegnitz, M., Heeschen, K., Schicks, J. (2014): Are Laboratory-Formed Hydrate-Bearing Systems Analogous to Those in Nature? - Journal of Chemical and Engineering Data, 60, 2, p. 258-268.

DOI: http://doi.org/10.1021/je5005609

Reprinted with permission from ACS Publications. Copyright 2014 American Chemical Society.

Contribution

Dr. Erik Spangenberg carried out the research together with Dr. Katja Heeschen, Dr. Judith Schicks, and me. I provided the experimental data sets to identify the spatial hydrate distribution in LARS and to analyse possible recrystallization effects. Data interpretation was done by all authors. Finally, Dr. Erik Spangenberg wrote the manuscript.

Are laboratory-formed hydrate-bearing systems analog to nature?

Erik Spangenberg[*]*, Mike Priegnitz, Katja Heeschen, and Judith M. Schicks*

[*]Helmholtz Centre Potsdam GFZ German Research Centre for Geosciences, Telegrafenberg, 14473 Potsdam, GERMANY

KEYWORDS: methane hydrate; hydrate formation; hydrate reservoir; artificial hydrate samples

ABSTRACT: The intensive study of hydrate-bearing sandy sediments, a possible source of fossil energy for future generations, leads to an accumulation of information from field studies, laboratory studies, and modeling. This information is used to create conceptual models for hydrate deposit genesis helping to assess the value of laboratory experimental studies on artificially formed hydrate-bearing sediments. We present an experimental example on the simulation of hydrate formation from methane dissolved in water, which is assumed to be the most likely natural process for the genesis of highly concentrated hydrate in sandy sediments. Measurements of the concentration of dissolved methane, temperature, and electrical resistivity tomography are used to describe and characterize the hydrate formation process. It could be shown that the way in which hydrate forms in this laboratory experiment corresponds to the procedure assumed for natural scenarios. The main difference to nature is probably the high

crystal growth rate which seems to result in an increased water-hydrate interface and a subsequent "aging" or recrystallization process affecting certain physical properties.

1. INDRODUCTION

Gas hydrates are nonstoichiometric crystalline solids composed of low molecular weight gases that are encased in a lattice of hydrogen-bonded water molecules.[1] Hydrates are stable under conditions of elevated pressure and low temperature given appropriate gas concentrations and water supply. In natural environments, they preferentially occur as methane hydrate in seafloor sediments and beneath the permafrost in arctic regions.[2,3] Since a number of estimates suggest that large amounts of carbon are stored in naturally occurring methane hydrates,[4,5] these deposits have attracted interest as a possible future energy resource.[6,7,8] Hydrates occur primarily as massive solid bodies in association with gas venting,[9] as grain-displacing aggregations (nodules and veins) in poorly compacted fine-grained sediments,[10,11] and as pore-filling gas hydrates with hydrate saturations less than 10 % in fine-grained sediments and much higher saturations (50 % to 90 %) in coarser materials such as coarse silts and sands (see Boswell et al. and references therein).[12] An explanation for the different hydrate morphologies found in natural water saturated hydrate systems can be provided by particle-level force analysis. The hydrate morphology is governed by skeleton and capillary forces, which depend on the burial depth and grain size of the host sediment.[13] Although current estimates suggest that only 10 % or even less of the gas bound to methane hydrate can be found in sand/sandstone formations,[14] this type of reservoir is in the focus of exploration for hydrates as energy resource. The high permeability of sands compared to that of the fine-grained sediments is very likely the reason that hydrate can accumulate to

concentrations up to 90 % of the available pore volume.[14,15,16] Furthermore, if the hydrate is destabilized by pressure reduction, heating, or injection of chemicals, the pores become free and permeable to access further regions of the reservoir and to produce the released gas via the well bore with the existing technology of oil and gas industry. Reservoir delineation, general reservoir properties, and migration pathways can be identified using geophysical methods such as seismic or electromagnetic surveys.[17,18,19] These mapping technologies rely on the influence that hydrate exerts on the sediment physical properties relative to hydrate-free sediments.[20] The resistivity increases with increasing hydrate content due to the fact that hydrate as a non-conducting phase replaces the conductive pore water. Modelling results show that the way in which hydrate influences the electrical properties depends on the hydrate habit and the location where the hydrate forms in the pore space.[21] The influences of nodular, layered, cementing and non-cementing pore-filling hydrate habits on the electrical properties were studied in detail. For non-cementing pore-filling hydrate the model predicts a dependence of resistivity on hydrate saturation and grain-size. This influence on grain size becomes apparent for hydrate saturations higher than 60 %. This dependency results from the change of free water dominated conduction to bound water dominated conduction at higher hydrate concentrations and from the fact, that the bound water to free water ratio depends on grain-size. Laboratory experiments seem to show such an effect already for lower hydrate concentrations.[22] However, these models are not practical for the estimation of hydrate saturation from resistivity measurements. Hence, Archie's equation[23] is used to interpret electrical field measurements in coarse grained sediments, where the contribution from surface conductivity is negligible.[24]

For the seismic properties the situation is similar. Generally seismic velocities (p- and s-wave) increase with increasing hydrate content. How strong seismic velocities increase with hydrate

saturation depends on the location where the hydrate forms in the pores. Generally three habits are distinguished for pore space hydrate in sands (see Waite et al. and references therein):[20] (1) non-cementing pore-filling, (2) load bearing and (3) cementing hydrate, which can be subdivided into grain-contact cementation and grain-coating cementation. Non-cementing pore-filling hydrate grows freely in the pore space without contact to the sediment grains. At a certain hydrate saturation (25 % - 40 %),[25,26] it starts to build bridges between neighboring grains and becomes load-bearing and grain-supporting respectively. Another modeling approach avoids the consideration of different hydrate habits using the patchy saturation concept[27] to estimate the influence of hydrate saturation on physical rock properties.[13] Dai et al.[13] argue that in mature coarse grained hydrate systems Oswald ripening[28] of pore filling hydrate will result in "patchy hydrate saturation" where patches containing 100 % hydrate in the pores are embedded in a hydrate-free water saturated sand. For a detailed description of the modeling methodology see Dai et al.[13] and references therein.

However, there are a number of theoretical and semi-empirical models that relate physical properties to hydrate saturation while accounting for different hydrate pore habits (e.g. Dvorkin et al. and Chand et al.).[29,30] The application of the existing rock physical models on field data does not fully meet the requirements. Dai et al.[17] state: "More work should be done to further refine the existing rock models as we access data from offshore regions. Controlled laboratory experiments will also add value, provided care is taken to simulate in the experiments the environment of the naturally occurring hydrates." This expresses the demand of geophysical exploration on petrophysics. Tackling this problem requires a better understanding of the geological controls on hydrate formation in porous systems, which can only be achieved by

combining all sources of information: drilling, coring, logging, laboratory experiments, and modelling.

This paper aims to combine the increased knowledge available on hydrate bearing reservoirs from field studies, numerical studies on field scenarios, and conceptual models with laboratory measurements and observations on artificial hydrate-bearing sediment samples. The goal is an assessment of the value of laboratory studies with artificial samples to natural hydrate occurrences. Since concentrated hydrates in sands and coarse silts are moved into the focus of interest[14] and it is assumed that these reservoirs formed from dissolved-phase methane,[20,31] we will concentrate on formation mechanism of hydrate from dissolved-phase methane in artificial laboratory samples. This will allow us to outline the experience gained with this method during the past few years.

2. CONCEPTUAL MODELS

2.1. The formation of hydrate-bearing sandy reservoirs

At the Mallik 38 L, 2L and 5L research and production wells hydrate has been found down to a depth of about 1100 m.[16] Based on hydrate stability calculations, the depth of the methane hydrate zone (MHZ) coincides with the base of gas hydrate stability (BGHS – defined by temperature and pressure), thus, the migrating pore water must be methane saturated when entering the BGHS (Fig. 1A, green dotted arrow). Pore water with lower methane concentrations (dotted black arrow) would only become saturated at shallower depths leading to a shallower MHZ compared to the BGHS. Higher methane concentrations would then result in a free gas zone (FGZ) directly below the BGHS. At a certain depth the pore water would reach saturation (dotted black arrow; the dotted signature represents single phase flow). With further decreasing

depth a gas phase would evolve and migrate with the water as two-phase flow (dot-dashed black arrow; the dot-dash signature represents two phase flow). Despite very high gas hydrate saturations of up to 90 % in sands just above the BGHS (1107 m),[16] no free-gas-bearing sediment has been confirmed by well-log-analysis below the BGHS.[32]

In the Ulleung Basin the variation of methane solubility with depth is much stronger due to the high geothermal gradient (Fig. 1B). It even has a local minimum below the BGHS at a depth of about 2700 m. As before, the left green dotted arrow marks the maximum CH_4 concentration which does not exceed the solubility limit before the water migrates into the BGHS. In this situation the dotted green arrow strikes the solubility limit inside the stability field, slightly above the BGHS. Water with a methane concentration of about 0.15 mol/kg, migrates along the right green arrow. The water crosses the solubility curve below its local minimum and a free gas phase will evolve and migrate together with the water (the green dot-dashed arrow marks the range of two-phase flow). For methane concentrations in between both green arrows (0.13 mol/kg < C_{CH4} < 0.15 mol/kg) the upward migrating water crosses the solubility curve twice. For the first time at a depth below 2700 m the water becomes oversaturated and free gas will form and, for the second time, at a depth below the BGHS, where the water will start to dissolve the gas again. Theoretically, between the green arrows, the water could dissolve the available free gas completely and reach the BGHS as a methane-saturated single liquid phase. Depending on the relation between mass transport and dissolution kinetics, some free gas might reach the BGHS. In any case, a free gas zone (FGH) exists below the BGHS, although the top of the FGZ might be separated by a certain distance from the BGHS (black arrow between the green arrows). Right from the second green arrow a free gas zone exists directly beneath the BGHS (right black arrow). Ryu et al.[33] reported BSR's in some locations in the western deep water Ulleung Basin

characterized by a sharp velocity increase above and a strong velocity decrease below the BGHS. The observed velocity decrease is a strong argument for the existence of free gas underlying the hydrates. For a more general view on methane transport into the hydrate stability zone see Rempel and Buffett[34] and Xu and Ruppel.[35]

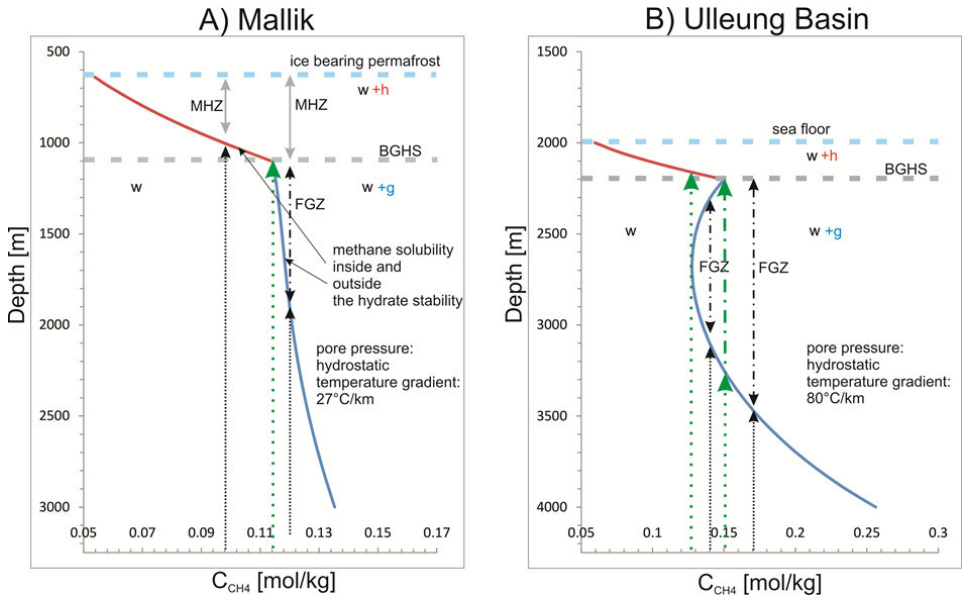

Figure 1. Solubility of methane in brine as a function of depth based on prevailing conditions at A) the Mallik test site and B) the Ulleung Basin (see text). The blue and red curves are the methane solubility curves in the absence (blue) and presence (red) of gas hydrate. They are based on equations published by Duan & Mao[36] and Sloan,[1] respectively. The arrows indicate advecting fluids with different methane concentrations, which become oversaturated when crossing the solubility curve (blue line) and migrate then as two phase system (dotted – liquid; dot-dashed – liquid + gas). FGZ: Free gas zone; MHZ: Methane hydrate zone; BGHS: Base of gas hydrate stability zone, w: water, h: hydrate, g: gas

Despite this conceptual model being rather simplified, it satisfies the derivation of different scenarios of methane transport into the MHZ and the resulting different hydrate formation mechanisms leading to different hydrate habits. To satisfy the high variability of natural systems, gas migration due to enhanced methane production, gas reservoirs, adsorption processes in clay-rich sediments or other chromatographic separation of gases would need to be taken into account to explain features such as the missing free gas zone directly below the BGHS at the Mallik test site. An under-saturation of methane is not to be expected at this site from the concentration-depth function only since there is a conventional natural gas reservoir at greater depth,[37] which is assumed to be the source for the formation of the gas hydrate reservoirs above.

If methane is produced outside the stability field and migrates into the zone of hydrate stability, we can distinguish the following scenarios:

2.2. Scenario 1: Dissolved phase methane transport into the MHZ

If the migrating methane-laden pore water is under-saturated when entering the BGHS, it advects into colder regions before the solubility in the presence of gas hydrates is exceeded, which in turn leads to the growth of pore filling hydrates directly from the dissolved phase. The bottom of the MHZ would be located above the BGHS. If the saturation limit for dissolved methane was reached directly at the BGHS (see green dashed line in Figure 1A), hydrate would start to form directly at the BGHS which is then the bottom of the MHZ.

Figure 1 shows that the change of methane solubility with depth is strongest directly at the BGHS and slowly decreases with decreasing depth into the MHZ. Once hydrate is formed, it can be assumed that the highest hydrate formation rate and concentration occur directly above the

bottom of the MHZ and both; rate and concentration, decreases with depth, since the change of solubility decreases (see explanation in section 3.3).

2.3. Scenario 2: Gas phase methane transport to the BGHS

If the methane concentration exceeds solubility before the pore water reaches the BGHS, methane gas bubbles will form in the pores. Small bubbles might be transported upward with the advecting pore water and grow due to the decreasing methane solubility and the decreasing pressure until they get trapped at grain surfaces and pore throats by capillary forces. They possibly form larger patches of gas filled pores before moving again, controlled by capillary effects involving interfacial tension, wettability of the solid surface, and the geometric structure of the interfaces.[38,39,40] Because the induction time for initial hydrate nucleation can be neglected on a geological time scale (see section 3.2 and 3.3) the free gas phase reaching the BGHS, will immediately form hydrate at the gas-water interface and start sealing the BGHS (Figure 2 and Figure 3). If there is a two- phase flow of methane gas and water towards the BGHS, the migrating water is generally methane saturated and hydrate will form from gaseous and dissolved methane.

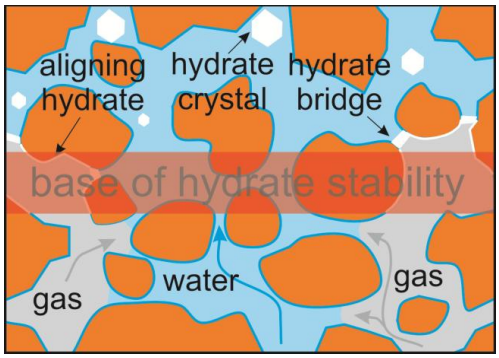

Figure 2. Sketch of a two phase flow of methane-laden pore water and free methane gas into the MHZ. Hydrate forms at the water-gas interface and from dissolved methane in the MHZ as it was observed in the laboratory experiments (see below).

2.4. Scenario 3: Depth shift of stability conditions due to sea level or climate changes

The formation of methane hydrate can also result from the shift of the BGHS towards greater depths where sediments have substantial accumulations of free methane gas. This might result from a pressure increase due to a sea level rise[41] or a temperature decrease e.g. in conjunction with a progression of permafrost.[42]

If a sediment layer containing a high concentration of free methane gas is shifted into the MHZ by one of the above described processes, hydrate formation from methane gas and pore water would occur throughout the gas-bearing sediment unit (Figure 3) and would not be restricted to the BGHS as in scenario 1. A high concentration of free gas in this scenario implies that the gas forms a continuous phase throughout the pore network over a large spatial area. The hydrate formation from methane gas and water would occur directly at the gas-water interface forming a "seal" that restricts the phase exchange to gas diffusion through the hydrate structure and temporary water leakage into the gas patch. Three phases would be present in the MHZ: liquid, gas, and gas hydrate.

In smaller isolated gas saturated patches the pressure will decrease when the gas is consumed in the hydrate formation process. Due to the pressure difference over the "hydrate seal", water may leak into the patch until the gas is consumed. The life span of such an isolated patch depends on the volume of entrapped gas. In addition to such isolated gas compartments, gas-bearing areas might exist which are still connected to the free gas zone below the BGHS, e.g., in

conduits. These areas may be fed with methane gas from greater depth and could build up considerable overpressure across the hydrate barrier. The overpressure might lead to fracture formation and further gas invasion into or through the MHZ. For a detailed description of these processes see Fauria and Rempel.[40]

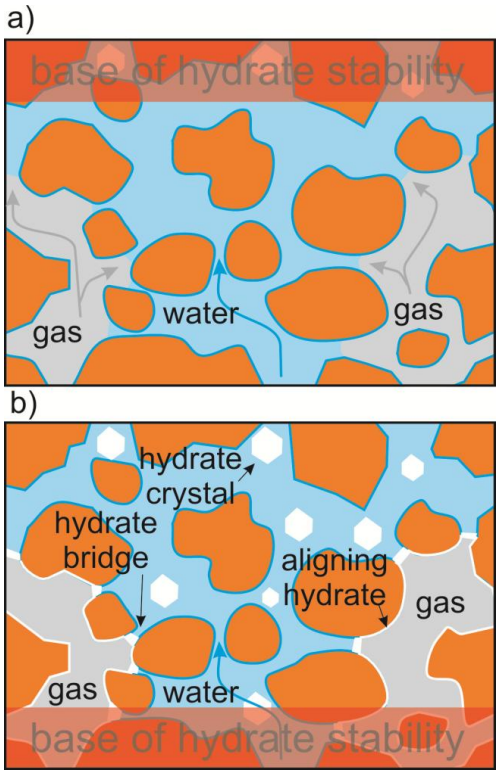

Figure 3. Free gas below the original BGHS (a) is shifted into the MHZ when the BGHS moves downwards (b). At the gas-water interface grain-bridging hydrate and grain-aligning hydrate is formed, where non-cementing pore-filling hydrate crystallizes from dissolved methane in the water filled pores and from microscopic gas bubbles.

The residual water trapped inside the gas zones would be depleted due to hydrate formation until the increasing salinity shifts the system to the three phase equilibrium.[4] The coexistence of

gas hydrate and water with free gas in the MHZ is used as an explanation for the "wipe-out zones" observed in seismic surveys.[43]

If a sediment layer is shifted into the MHZ with a concentration of free gas too low to form a continuous gas phase, the gas occurs as microscopic bubbles in the pores, and will be consumed in hydrate formation as it enters the stability field. Another important aspect is the formation of various forms of gas hydrates such as non-cementing pore-filling in the water saturated areas as well as grain-coating and grain-bridging hydrate in the gas compartments.

If the methane is formed by microbial activity inside the hydrate stability field, hydrate would form from methane dissolved in pore water. Microbial methane production generally is bound to organic rich fine-grained sediments where a certain amount of "supersaturation" with respect to hydrate stability may occur due to the fact that hydrate formation is inhibited in small pores.[44] The dissolved methane might diffuse into neighboring sandy sediments and form pore filling hydrate.[45]

3. EXPERIMENTAL RESULTS AND DISCUSSION

3.1. Laboratory observations regarding the specific habitus of gas hydrates from different formation scenarios

The visual observations from hydrate formation in laboratory studies (see Figure 4) support the following conception of the hydrate formation and growth process:

- Hydrate formation from gaseous methane is preferred at the gas-water interface (Figure 4: 1a-1c and 2a-2c). The specific shape of the gas-water interface results from the wetting properties, surface tension and the pore space structure (grain shape and grain size distribution).

- A hydrate film develops along the water-methane interface forming hydrate bridges in the pore throats between the grains and a shell of grain-aligning hydrate at the interface between the methane gas and the bound-water that wets the sediment grains (Figure 4: 1a-1c; also see Freer et al.[46]). However, the hydrate formation at the gas-water-grain interface leads to barriers that could trap gas and restrict methane transport to diffusion through the hydrate barrier. Small gas bubbles might be dissolved and feed the growth of the hydrate around larger bubbles (Figure 4: 2a-2c).
- Methane saturated water migrates into the hydrate stability zone where it cools down and hydrate crystals nucleate and grow from the excess methane and water since the methane solubility decreases with temperature (Figure 4: 3a-3c).

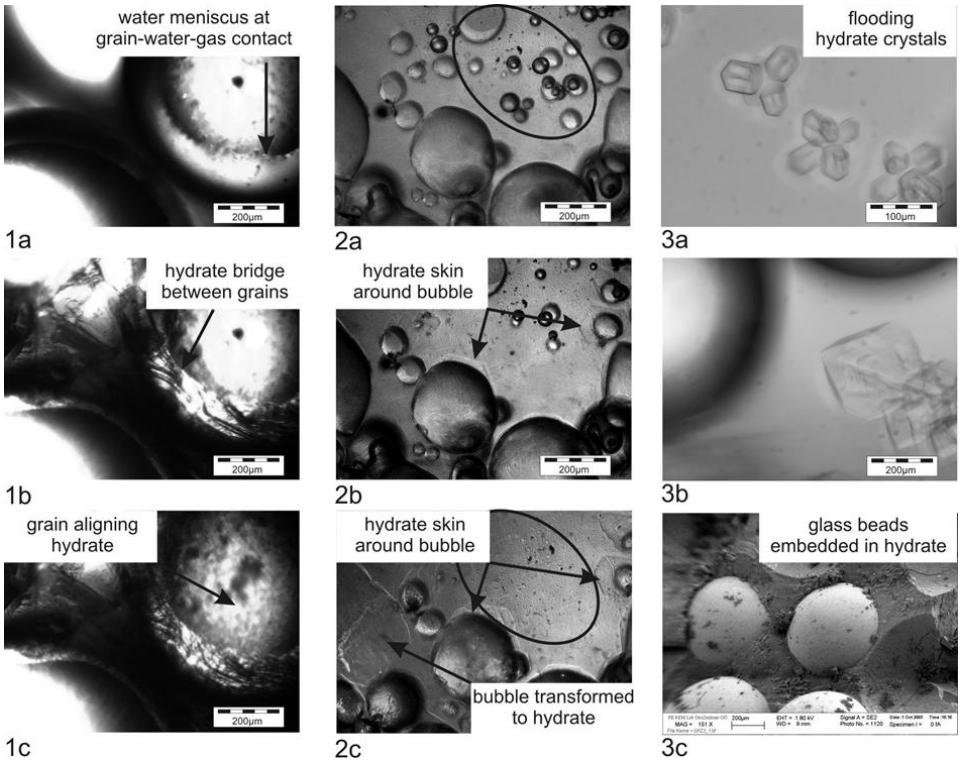

Figure 4. Images of hydrate growing from water and free methane gas (1-2) and from methane dissolved in water (3). The procedure to gain these photographs is described in detail in Spangenberg et al.[47] 1a) Glass beads, water, and methane situated outside the hydrate stability. 1b) Hydrate growing at the gas-water interface forming a bridge between neighboring grains. 1c) Water, wetting the glass beads is finally transformed into hydrate and the grain surface is covered with grain aligning hydrate. 2a) Methane bubbles in water outside the hydrate stability field. 2b) Within the hydrate stability field hydrate starts to form around the bubbles. 2c) Large bubbles are transformed to hydrate (some with a gas inclusion inside), whereas smaller bubbles disappear due to dissolution and hydrate formation (see ellipse in 2a and 2b). 3a) Hydrate formed from methane dissolved in water without a free gas phase crystallizes in the pore water. 3b) To date there is no evidence that hydrate crystals grow at grain surfaces. We could only observe hydrate flooding in the pore water. 3c) An SEM-image of glass beads embedded in a matrix of almost pure methane hydrate (ice to hydrate ratio is 17% : 83%).[15]

The grain-bridging and grain-coating hydrate habit shown in Figure 4: 1b and 1c result, if hydrate is formed with sufficient gas to consume the available pore water completely. Transforming the water into hydrate by continuous gas supply to partially water saturated sediment samples is used in a number of laboratory experimental studies.[48,49,50] This method, called “excess gas method”, forms grain-cementing hydrate.[51] Laboratory formed hydrate-bearing sediment samples of this type very likely reflect physical properties similar to hydrate-bearing sediments directly at the BGHS with underlying gas (scenario 2) and gas saturated areas within the MHZ (scenario 3).

Measurements show that only 5 % to 10 % hydrate saturation with cementing hydrate increases the seismic p-wave velocity as about 40 % of pore-filling hydrate.[51] Transferring this

finding to scenario 2 would explain that strong BSR's could exist at a gas underlain BGHS even if the hydrate saturation is low.

Figure 4: 2a to 2c show that microscopic gas bubbles are transformed into hydrate with time, if sufficient water is supplied. This is probably the way hydrates form in the "excess water method".[51] In this method, a known value of methane gas is injected into the specimen before water is injected until the target pore pressure is reached. The sample is cooled into the stability field and the pore pressure is held constant during hydrate formation by water injection.[51] This method results in a load-bearing or grain-supporting and pore-filling hydrate habit. This is probably what we can expect in scenarios 2 and 3, if the gas saturation in the sediments is low and the gas occurs as small bubbles in pores rather than as continuous phase throughout the pore network before entering the hydrate stability field.

Figure 4: 3 shows non-cementing pore-filling hydrate formed from methane dissolved in water. Because methane solubility is low, hydrate formation from dissolved-phase methane in the laboratory is a slow and long-lasting process.[15,52,53] However, because it is assumed that this process forms the high hydrate concentrations in sands and coarse silts,[31,20] the method should be improved in order to provide information and data that are valuable for the interpretation of geophysical field and borehole measurements and the general understanding of this type of hydrate-bearing reservoirs. This formation process corresponds to scenario 1.

3.2. Formation of laboratory hydrate-bearing samples from dissolved-phase methane:

Experimental System and Hydrate Formation Procedure: A major drawback of the experimental system used for the generation of hydrate bearing samples in the studies of 2005 – 2007[15,47] was the small sample size. The sediment sample cell of this system was 50 mm in both,

diameter and length. In this small setup, it was difficult to exactly control the temperature right at the fluid inlet which made the system very susceptible to hydraulic clogging. Based on this methodological concept, a large reservoir simulator (LARS) was developed. Because great importance was placed on the temperature control directly at the fluid inlet, clogging can be avoided and hydrate can form in porous sediments from dissolved phase methane on a routine base.[52] The main 5 components of LARS are shown in Figure 5. Here we will focus on the formation mechanism rather than on the technical details which can be found in Schicks et al.[52] and Priegnitz et al.[54]

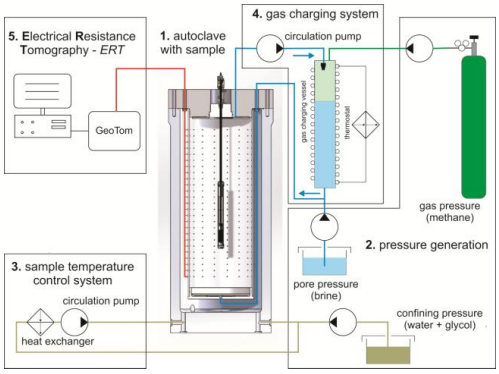

Figure 5. The 5 components of LARS. 1) Temperature controlled pressure vessel with sediment sample; 2) Pressure generation system with the pumps for the confining pressure and gas and water pore fluid pressure pumps; 3) Temperature control system for the pressure vessel with chiller, heat exchanger and circulation pump for the confining pressure transfer fluid; 4) Temperature controlled gas charging pressure vessel with pore water circulation pump; 5) Electrical resistivity tomography system

The sediment sample with a diameter of 460 mm and a length of about 1300 mm can be set under simulated *in situ* conditions in the pressure vessel (1). The pore fluid pressure and confining pressure simulating the overburden is provided by syringe pumps (2). The sample temperature is controlled by tempering and circulating the confining pressure fluid through a head exchanger (3). A crucial component is the gas charging vessel (4). This is a temperature controlled pressure vessel containing a methane headspace over pore water which is circulated through the sediment sample. The water is pumped from the sediment sample through a spray nozzle into the gas charging vessel. To avoid hydrate formation at the nozzle, the water is heated to a temperature slightly above hydrate stability (about 2 °C above the stability temperature for a given pressure) before it enters the gas charging vessel. The mist dissolves methane from the methane headspace and precipitates at the water surface. The methane-charged water flows back to the pressure vessel and enters the sediment sample with a temperature of about 1°C to 2 °C above the hydrate stability. In the sediment sample, the water cools down to temperature conditions within the hydrate stability field and hydrate starts to form. Because the density of hydrate is lower than that of water, hydrate formation leads to a volume increase and therefore, a decrease of the methane headspace in the gas charging vessel. To account for that, water is withdrawn at certain time intervals from the system. Since dissolved salt ions are not incorporated into the hydrate structure during hydrate formation, the salt (NaCl) concentration of the remaining pore fluid increases with increasing hydrate saturation. From the corresponding electrical conductivity increase of withdrawn fluid samples, the amount of water fixed in the hydrate structure and the overall hydrate saturation can be determined.[15,22] The pore pressure is kept constant by continuous methane supply from methane cylinder via the methane pump.

The temperature measurements of the circulating fluid directly at the fluid inlet, outlet, and a number of different positions within the sample give an idea of the temperature field and its changes with increasing hydrate content. The assumption that the hydrate saturations in the sample are higher where the temperatures are the lowest and, thus, the driving force for hydrate growth is the highest, has not been supported by the first hydrate destabilization and methane production test carried out in this system.

The initial hydrate nucleation will very likely occur where the driving force or methane super-saturation respectively is highest and, therefore, the induction time is lowest.[55,56,57,58] But the subsequent hydrate growth process obviously is shifted along the gradient in methane concentration, against the flow direction, towards the stability boundary in the sediment sample. This hypothesis would explain that we observed high hydrate concentrations in the warmer parts of the sample and not as expected in the coldest areas.

In order to prove this hypothesis and to get a better understanding of the hydrate distribution within the sample the electrical resistivity tomography system (ERT) (5) with 375 electrodes was installed and used.[54] ERT does not provide the high spatial resolution of X-ray and NMR tomography, but these highly resolving methods are not practicable for a pressure system with a sample volume of more than 200 l. Ultrasonic velocity tomography would have been another alternative but for technical and budget reasons it could not realized in our system yet.

3.3. Controls on hydrate saturation distribution

The ERT provides images of the resistivity distribution inside the sediment sample, which can be transferred into a hydrate distribution using Archie's equation.[23] The ERT has been proved to be a very useful tool in an experiment aimed to simulate the 2008 depressurization experiment at Mallik.[16] In order to provide conditions close to that of the tested hydrate zone at Mallik, a

hydrate saturation of about 90 % had to be produced in the sediment sample prior to the production test.[16] To realize such high hydrate saturation within a short time, it is important to maintain fluid circulation on high flow rates and low pressure gradients. Based on the ERT measurements we were able to assess where areas of high hydrate saturation start to form permeability barriers and could adjust the experimental conditions to avoid blockage. Figure 6 shows that we changed flow direction at a total hydrate saturation of about 40 % because hydrate was only accumulating in the upper third of the sample, which could be seen from the increasing resistivity.

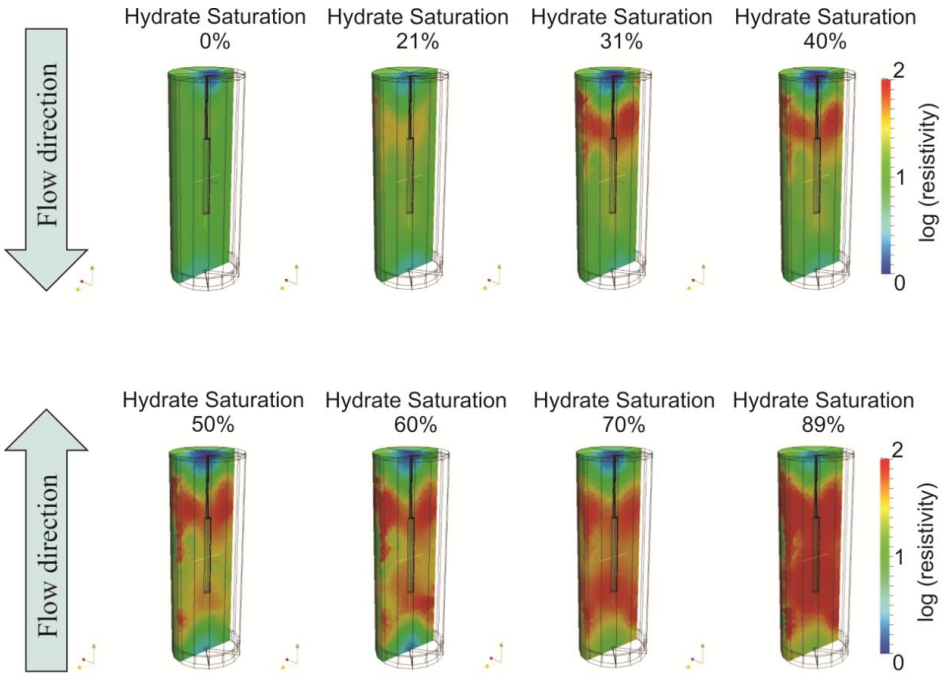

Figure 6. Evolution of the electrical resistivity distribution in the sediment sample during the hydrate formation phase. Areas with orange to red color represent high resistivity due to high concentration of pore space hydrate. At an overall hydrate concentration of 40 % the flow

direction was changed from downwards to upwards in order to maintain fluid circulation with a low pore pressure gradient over the sample.

The methane supply is another important issue producing high hydrate concentrations within a reasonable time. However, the performance of these hydrate formation systems mainly depends on the reached level of dissolved methane concentration.[53] In order to assess the performance of the system during this test, a commercial methane sensor was installed to measure the concentration of dissolved methane at the out- and inlet of the gas charging vessel. Figure 7 shows that the dissolved methane concentration is close to saturation when leaving the gas charging vessel, which is held at a temperature of 18 °C. The pore fluid is slightly oversaturated with respect to the lowest temperature in the sample when leaving the sediment at the fluid outlet.

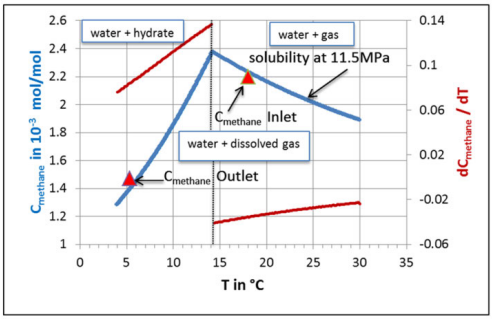

Figure 7. Methane solubility and change of methane solubility ($dC_{methane}/dT$) with temperature at constant pressure of 11.5 MPa (calculations are based on equations published by Duan & Mao)[36]. The red triangles represent methane concentration measurements of the water when it leaves the gas water charging vessel before it enters the sample (inlet) and after leaving the sample (outlet).

The change of methane concentration with temperature ($dC_{methane}/dT$) is highest directly when the water reaches the hydrate stability and decreases with decreasing temperatures in the hydrate stability field. For flow velocities low enough for the hydrate formation process to consume all the available dissolved methane for the corresponding temperature, the highest hydrate concentrations should be observed directly in those areas of the sample where the water reaches the hydrate stability temperature. Almost all of the available, dissolved methane was consumed via hydrate formation within the time span the water percolates through the sediment. This information together with the observed saturation distribution from ERT and the temperature measurements inside the sediment sample (see Figure 8) proved that the hydrate concentration in the sediment is the highest where the change of methane concentration with temperature is the strongest. This is as one would expect, if the hydrate growth kinetics is not limiting the process but methane supply is the restricting factor.[53] Figure 8 shows that during the downwards fluid flow about 60 % of the available methane should be consumed before reaching the temperature level of T4 in the upper third of the sample. About 30 % of the methane will be consumed in the remaining two thirds of the sample. The ERT image at about 40 % total hydrate saturation supports the fact that the highest hydrate concentrations occur directly where the water enters the hydrate stability field slightly below temperature sensor T2. The bottom up flow changed the temperature field inside the sample because the warm water from the gas charging vessel now entered the system from the bottom. As a consequence this area was outside the hydrate stability field. At the position of T12, however, the pore water was already deep in the stability field and at the position of T6 more than 70 % of the available methane should be consumed due to hydrate formation. The ERT image taken at a hydrate saturation of about 89 % shows that we

have the highest resistivities in the lower part of the upper third from the downwards flow phase and in the upper part of the lower third from the upwards flow phase. The resistivities in the middle part of the sample are a little bit lower.

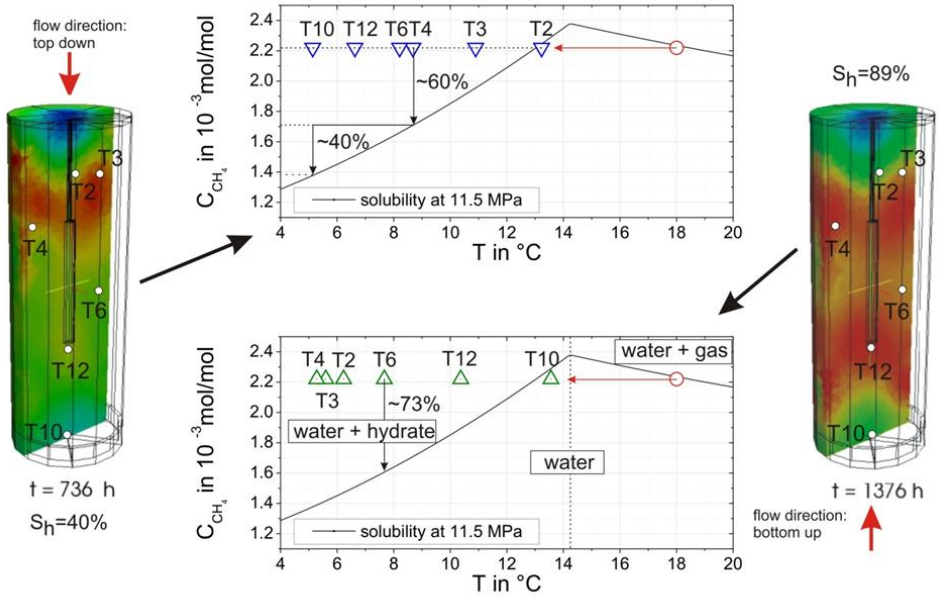

Figure 8. ERT images when flow direction was changed from top down to bottom up at an overall hydrate saturation of 40 % (left) and when the hydrate production phase was stopped at an overall hydrate saturation of 89 % (right). Switching the pore fluid flow direction changes the temperature field inside the sample which is shown in the diagrams for some selected temperature sensors. The upper diagram shows that about 60 % of the available methane should be consumed when reaching the temperature measured at position T4 in the lower part of the

upper third. The lower diagram shows that about 70 % of the available methane is consumed before the temperature of T6 in the middle of the sample is reached.

The experiment shows clearly, that even on a short "lab-time-scale" hydrate forms with respect to the methane concentration along the stability curve as one would expect on a geological time scale in a natural hydrate system. Certainly, the nucleation starts somewhere deeper in the stability field. Since the water circulation causes high temperature gradients in the sample the initial super-saturation will vary depending on the location. Figure 8 reveals the possible level of super-saturation in relation to the temperature at different positions in the sample. Depending on the super-saturation and the corresponding induction time it is very likely that multiple nucleation occurs in the large sample volume. In a highly resolving NMR system such as NESSI used by Kossel et al.[59] the hydrate growth from the location of nucleation towards the direction of methane supply can be visualized.[60] However, we cannot resolve locations of nucleation with ERT in our experiment. Hydrate forms already according to the equilibrium stability conditions, when its concentration is high enough to produce a clear resistivity signature in the ERT-images. The hydrate growth along the concentration gradient towards the stability boundary is even on a lab-time-scale not a "slow" process.

3.4. Recrystallization and aging

The extremely fast growth of pore space hydrate in the lab experiments compared to the natural scenarios very likely results in different crystal sizes and specific surfaces between the hydrate phase and the remaining pore water. Investigations on ice cores[61] showed that a clear correlation exists between crystal size and the age of the ice core, indicating that even under natural conditions recrystallization is a process that needs to be considered. Klapp et al.[62]

presented a study on the hydrate crystallite size distribution determined at six samples from the Gulf of Mexico and Hydrate Ridge. They report an increase of mean crystallite size with depth, possibly indicating a difference in the formation age. However, in our early experiments[15] we have clear evidence that recrystallization occurs as a time dependent process. Figure 9 shows, for water saturations below 10 %, a slight but clear decrease of the electrical resistivity or the resistivity index with time and decreasing hydrate formation rate. The resistivity index here is simply the ratio of the electrical resistivites of the sample at certain hydrate saturation $\rho(S_h)$ and complete water saturation ρ_0 ($I = \rho(S_h) / \rho_0$). At very high hydrate saturations ($S_h > 90$ %), the hydrate formation rate strongly slows down due to the decline of methane supply by water circulation. At this stage the resistivity index starts to decrease, although there still is a slight increase in hydrate saturation. We interpret this decrease as the result of a recrystallization due to Oswald ripening and a general equilibration of methane concentration gradients in the sample. The recrystallization process results in a "smoothing" of the fluid hydrate interface. The expression "smoothing" is used here as synonym for the reduction of the specific surface of the hydrate structure, the amount of micro pores between hydrate crystals, the tortuosity, and the constrictions in the remaining fluid pathways. This, in turn, decreases the resistance to hydrated ion transport and so the electrical resistivity of the hydrate bearing sediment.

The change of resistivity index from the maximum value of I = 72.6 to the last measured value of I = 67 is about 8 % in 13 days.

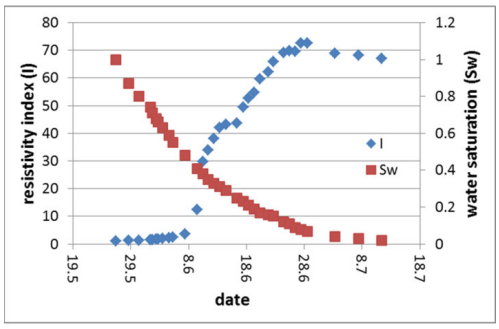

Figure 9. Increase of resistivity index and hydrate saturation (S_h = 1 - S_w) with time. The decrease of resistivity index with time for water saturations below 10% is due to recrystallization processes of the pore filling hydrate.

Figure 10 shows that such a resistivity decrease due to recrystallization after hydrate formation was stopped could be confirmed in the LARS sample which has a volume that is 2200 times larger than the sample in the old system. Furthermore, the tomographic image shows that the effect is strongest where the resistivity and, therefore, the hydrate concentration is highest.

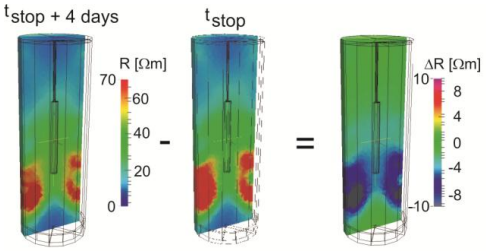

Figure 10. Tomographic resistivity images of a sample with 50 % hydrate saturation when the formation process was finished (t_{stop}) , 4 days later ($t_{stop\ +\ 4\ days}$) and the resulting differences in resistivity.

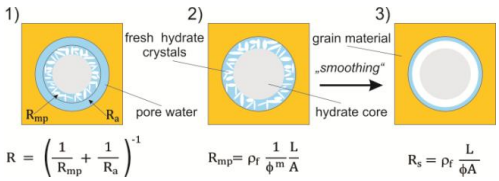

Figure 11. Pore models to explain the influence of recrystallization of fast grown hydrate crystallites on electrical resistivity. A detailed explanation is given in the text.

Figure 11 shows very simplified models of a cylindrical pores containing pore filling hydrate in a coaxial arrangement to explain the observations and support our interpretation. The first of the three models shows a cylindrical pore containing a cylindrical hydrate core in the center. The hydrate core already underwent recrystallization. It is overgrown by small hydrate crystals forming a micro-porous layer that increases the surface of the water-hydrate interface. This micro-porous layer has the resistance R_{mp}. The free pore water annulus around the micro-porous hydrate layer has the resistance R_a. Since both resisters are in parallel, the resistance of the pore channel is mainly determined by the lower resistance of the fluid annulus at low hydrate saturation. For increasing hydrate saturation the influence of R_{mp} increases. The second model shows the situation at very high hydrate saturation where the free fluid annulus is vanished. The resistance of the pore channel is then R_{mp} which can be described by the Archie-equation as

$$R_{mp} = \rho_f \frac{1}{\Phi^m} \frac{L}{A}. \qquad (1)$$

A is the cross sectional area of micro-porous layer, L is the length of the pore channel, Φ is the porosity of the micro-porous layer, and ρ_f is the fluid resistivity. In the third model we consider that recrystallization results in a smooth pore-free hydrate layer on the hydrate core. The resistance of the pore channel is

$$R_s = \rho_f \frac{L}{\Phi A}. \qquad (2)$$

If we assume a micro-porosity of 0.5 and a standard cementation exponent of m = 2 the recrystallization from model 2 to model 3 would result in a resistance Rs of the smoothed system, which is the half of the original system with the resistance R_{mp}.

These models explain that "smoothing" can significantly decrease resistivity and support the observation that the effect is as stronger as higher the hydrate saturation is.

4. CONCLUSION

The presented conceptual models for hydrate formation in sandy reservoirs suggest that all hydrate habits that we know from laboratory investigations on artificial hydrate-bearing samples occur in nature. However, the occurrence of cementing hydrate is probably restricted to:

1) the BGHS in settings which are underlain by formations containing high methane gas concentrations and

2) reservoirs that contain free gas within the hydrate stability field, e.g. in areas with very high methane fluxes.

The main mechanism forming high concentrations of methane hydrate in sandy reservoirs is most likely from dissolved phase methane. The study of this hydrate formation process in the laboratory reveals that even under the very high formation rates compared to nature, this process is limited by methane supply rather than reaction kinetics.

The main differences to the natural systems result from the following facts:

1) The hydrate formation rate is speeded up from about 1 % hydrate saturation increase in about 10^5 years according to the assumptions made in Rempel and Buffett[34] for natural scenarios to 1 to 2 % per day in the lab. This means that the time scale in nature is up to 5 10^7 times larger than that in the lab. The high hydrate formation rate is a result of the fast methane supply by fluid

circulation. The Darcy-velocity of the circulating water is in the order of 1 mm/min (0.5 km/yr) compared to 0.3 mm/yr to 2 mm/yr for natural systems.[35]

2) Temperature gradients in laboratory systems are orders of magnitude higher than that in natural systems. During the Mallik-2008 simulation in LARS, the fluid enters the sample at a temperature of about 13 °C and leaves it at about 5 °C. This corresponds to a temperature gradient of about 6 °C/m, which is more than 220 times higher than that in, e.g., Mallik[63] (27 °C/km). In other words, the decrease in methane concentration that we observe over our sample occurs in Mallik at a depth interval of about 220 m within the hydrate stability field.

3) The high temperature and methane concentration gradients in the lab sample result in high local hydrate growth rates, very likely producing a large number of small sized hydrate crystallites that tend to recrystallize with time. From the observation of decreasing resistivities close to the end of the hydrate formation process we conclude a "smoothing" of the fluid-hydrate interface reducing the amount of pores between hydrate crystals, the tortuosity, and the constrictions of the charge carrier transport path ways. However, when the circulation is stopped at the end of an experiment, the system starts to equilibrate and the temperature and concentration gradients will decrease with time. Under equilibrated conditions Oswald ripening, driven by the concentration differences around crystals of different size, will be the main process of recrystallization in our lab-system. If Oswald ripening would finally result in patchy hydrate saturation as proposed by Dai et al.,[13] with patches containing 100 % hydrate in the pores embedded in hydrate-free water saturated sand, we can neither confirm nor refute based on our observations.

The recrystallization or "aging" effect requires more attention in future lab studies in order to assess its influence on the relationships between hydrate saturation and petrophysical sediment

properties. Highly resolving visualization methods could be useful tools to study the recrystallization of pore filling hydrate. Kuhs et al.[64] report on a study based on Synchrotron Radiation X-ray Cryo-Tomography Microscopy (SRXCTM) by which the nucleation and growth process of gas hydrate were observed in the presence of quartz grains and glass beads. SRXCTM under in-situ conditions allow for the study of hydrate formation with a resolution, sufficient to observe details of the interfaces involved in the recrystallization processes.

AUTHOR INFORMATION

Corresponding Author

*E-mail. erik@gfz-potsdam.de Tel: ++49 (0)331 1276Fax: ++49 (0)331 288 1450

Funding Sources

The Federal Ministry of Economic Affairs and Energy provided funding for this work through Research Grant 03SX320E.

ACKNOWLEDGMENT

We are very grateful to Ronny Giese and Alexander Reichardt for their support during the preparation and execution of the experiments. The authors thank the staff of the GFZ workshops for their invaluable technical support.

REFERENCES

(1) Sloan Jr, E. D.; Koh, C. Clathrate hydrates of natural gases. CRC press: 2007.

(2) Kvenvolden, K. A. Methane hydrate—a major reservoir of carbon in the shallow geosphere? Chem. Geol. 1988, 71 (1), 41-51.

(3) Kvenvolden, K. A. A review of the geochemistry of methane in natural gas hydrate. Org. Geochem. 1995, 23 (11), 997-1008.

(4) Milkov, A. V. Global estimates of hydrate-bound gas in marine sediments: how much is really out there? Earth-Sci. Rev. 2004, 66 (3), 183-197.

(5) Archer, D.; Buffett, B.; Brovkin, V. Ocean methane hydrates as a slow tipping point in the global carbon cycle. Proc. Int. Acad. Ecol. Environ. Sci. 2009, 106 (49), 20596-20601.

(6) Collett, T. S. Energy resource potential of natural gas hydrates. AAPG bulletin 2002, 86 (11), 1971-1992.

(7) Makogon, Y. F.; Holditch, S. A.; Makogon, T. Y. Natural gas-hydrates — A potential energy source for the 21st Century. J. Pet. Sci. Eng. 2007, 56 (1–3), 14-31.

(8) Boswell, R.; Collett, T. S. Current perspectives on gas hydrate resources. Energy Environ. Sci. 2011, 4, 1206-1215.

(9) Haeckel, M.; Suess, E.; Wallmann, K.; Rickert, D. Rising methane gas bubbles form massive hydrate layers at the seafloor. Geochim. Cosmochim. Acta 2004, 68 (21), 4335-4345.

(10) Tréhu, A. M.; Long, P. E.; Torres, M. E.; Bohrmann, G.; Rack, F. R.; Collett, T. S.; Goldberg, D. S.; Milkov, A. V.; Riedel, M.; Schultheiss, P.; Bangs, N. L.; Barr, S. R.; Borowski, W. S.; Claypool, G. E.; Delwiche, M. E.; Dickens, G. R.; Gracia, E.; Guerin, G.; Holland, M.; Johnson, J. E.; Lee, Y. J.; Liu, C. S.; Su, X.; Teichert, B.; Tomaru, H.; Vanneste, M.; Watanabe, M.; Weinberger, J. L. Three-dimensional distribution of gas hydrate beneath southern Hydrate Ridge: constraints from ODP Leg 204. Earth Planet. Sci. Lett. 2004, 222 (3–4), 845-862.

(11) Bahk, J. J.; Kim, D. H.; Chun, J. H.; Son, B. K.; Kim, J. H.; Ryu, B. J.; Torres, M. E.; Riedel, M.; Schultheiss, P. Gas hydrate occurrences and their relation to host sediment

properties: Results from Second Ulleung Basin Gas Hydrate Drilling Expedition, East Sea. Mar. Pet. Geol. 2013, 47 (0), 21-29.

(12) Boswell, R.; Collett, T. S.; Frye, M.; Shedd, W.; McConnell, D. R.; Shelander, D. Subsurface gas hydrates in the northern Gulf of Mexico. Mar. Pet. Geol. 2012, 34 (1), 4-30.

(13) Dai, S.; Santamarina, J. C.; Waite, W. F.; Kneafsey, T. J. Hydrate morphology: Physical properties of sands with patchy hydrate saturation. Journal of Geophysical Research: Solid Earth, 2012, 117(B11).

(14) Boswell, R. Is gas hydrate energy within reach? Science 2009, 325 (5943), 957-958.

(15) Spangenberg, E.; Kulenkampff, J.; Naumann, R.; Erzinger, J. Pore space hydrate formation in a glass bead sample from methane dissolved in water. Geophys. Res. Lett. 2005, 32

(16) Uddin, M.; Wright, J. F.; Dallimore, S. R.; Coombe, D. Gas hydrate production from the Mallik reservoir: numerical history matching and long-term production forecasting. In Scientific results from the JOGMEC/NRCan/Aurora Mallik 2007-2008 Gas Hydrate Production Research Well Program, Mackenzie Delta, Northwest Territories, Canada; Dallimore, S. R.; Yamamoto, K.; Wright, J. F.; Bellefleur, G., Eds. Geological Survey of Canada, Bulletin 601; Geological Survey of Canada: Ottawa, 2012; pp 261-289.

(17) Dai, J.; Snyder, F.; Gillespie, D.; Koesoemadinata, A.; Dutta, N. Exploration for gas hydrates in the deepwater, northern Gulf of Mexico: Part I. A seismic approach based on geologic model, inversion, and rock physics principles. Marine and Pet. Geol. 2008, 25 (9), 830-844.

(18) Weitemeyer, K.; Constable, S. Mapping shallow geology and gas hydrate with marine CSEM surveys. First Break 2010, 28 (6).

(19) Schwalenberg, K.; Haeckel, M.; Poort, J.; Jegen, M. Evaluation of gas hydrate deposits in an active seep area using marine controlled source electromagnetics: Results from Opouawe Bank, Hikurangi Margin, New Zealand. Marine Geology 2010, 272(1), 79-88.

(20) Waite, W. F.; Santamarina, J. C.; Cortes, D. D.; Dugan, B.; Espinoza, D.; Germaine, J.; Jang, J.; Jung, J.; Kneafsey, T. J.; Shin, H. Physical properties of hydrate-bearing sediments. Rev. Geophys. 2009, 47 (4).

(21) Spangenberg, E. Modeling of the influence of gas hydrate content on the electrical properties of porous sediments. Journal of Geophysical Research: Solid Earth 2001, 106(B4), 6535-6548.

(22) Spangenberg, E.; Kulenkampff, J. Influence of methane hydrate content on electrical sediment properties. Geophysical research letters 2006, 33(24).

(23) Archie, G. E. The electrical resistivity log as an aid in determining some reservoir characteristics. Trans. AIMe 1942, 146(1), 54-62.

(24) Schön, J. H. *Physical properties of rocks: fundamentals and principles of petrophysics*. Oxford, UK: Pergamon 1996

(25) Berge, L. I.; Jacobsen, K. A.; Solstad, A. Measured acoustic wave velocities of R11 (CCl3F) hydrate samples with and without sand as a function of hydrate concentration. Journal of Geophysical Research: Solid Earth 1999, (1978–2012), 104(B7), 15415-15424.

(26) Yun, T. S.; Francisca, F. M.; Santamarina, J. C.; Ruppel, C. Compressional and shear wave velocities in uncemented sediment containing gas hydrate. Geophysical Research Letters 2005, 32(10).

(27) Dvorkin, J.; Nur, A. Acoustic signatures of patchy saturation. International Journal of Solids and Structures, 1998, 35(34), 4803-4810.

(28) Voorhees, P. W. The theory of Ostwald ripening. Journal of Statistical Physics, 1985, 38(1-2), 231-252.

(29) Dvorkin, J.; Prasad, M.; Sakai, A.; Lavoie, D. Elasticity of marine sediments: Rock physics modeling. Geophysical Research Letters 1999, 26(12), 1781-1784.

(30) Chand, S.; Minshull, T. A.; Gei, D.; Carcione, J. M. Elastic velocity models for gas-hydrate-bearing sediments—a comparison. Geophysical Journal International 2004, 159(2), 573-590.

(31) Haacke, R. R.; Westbrook, G. K.; Hyndman, R. D. Gas hydrate, fluid flow and free gas: Formation of the bottom-simulating reflector. Earth and Planetary Science Letters 2007, 261(3), 407-420.

(32) Fujii, T.; Noguchi, S.; Murray, D. R.; Takayama, T.; Fujii, K.; Yamamoto, K.; Dallimore, S. R.; Al-Jubori, A. Overview of wireline-logging analysis in the Aurora/JOGMEC/NRCCan Mallik 2L38 gas hydrate production research well. In Scientific results from the JOGMEC/NRCan/Aurora Mallik 2007-2008 Gas Hydrate Production Research Well Program, Mackenzie Delta, Northwest Territories, Canada; Dallimore, S. R.; Yamamoto, K.; Wright, J. F.;

Bellefleur, G., Eds. Geological Survey of Canada, Bulletin 601; Geological Survey of Canada: Ottawa, 2012; pp 125-140.

(33) Ryu, B.-J.; Riedel, M.; Kim, J.-H.; Hyndman, R. D.; Lee, Y.-J.; Chung, B.-H.; Kim, I.-S. Gas hydrates in the western deep-water Ulleung Basin, East Sea of Korea. Mar. Pet. Geol. 2009, 26 (8), 1483-1498.

(34) Rempel, A. W.; Buffett, B. A. Formation and accumulation of gas hydrate in porous media. Journal of Geophysical Research: Solid Earth (1978–2012) 1997, 102(B5), 10151-10164.

(35) Xu, W.; Ruppel, C. Predicting the occurrence, distribution, and evolution of methane gas hydrate in porous marine sediments. J. Geophys. Res.: Solid Earth 1999, 104 (B3), 5081-5095.

(36) Duan, Z.; Mao, S. A thermodynamic model for calculating methane solubility, density and gas phase composition of methane-bearing aqueous fluids from 273 to 523°K and from 1 to 2000 bar. Geochim. Cosmochim. Acta 2006, 70 (13), 3369-3386.

(37) Osadetz, K. G.; Morrell, G. R.; Dixon, J.; Dietrich, J. R.; Snowdon, L. R.; Dallimore, S. R.; Majorowicz, J. A. Beaufort-Mackenzie Basin: a review of conventional and nonconventional (gas hydrate) petroleum reserves and undiscovered resources. Geol.Surv. Can. Bull. 2005, 585, 81.

(38) Hildenbrand, A.; Schlömer, S.; Krooss, B., Gas breakthrough experiments on fine-grained sedimentary rocks. Geofluids 2002, 2 (1), 3-23.

(39) Geistlinger, H.; Krauss, G.; Lazik, D.; Luckner, L. Direct gas injection into saturated glass beads: Transition from incoherent to coherent gas flow pattern. Water resources research 2006, 42(7).

(40) Fauria, K. E.; Rempel, A. W. Gas invasion into water-saturated, unconsolidated porous media: Implications for gas hydrate reservoirs. Earth Planet. Sci. Lett. 2011, 312 (1), 188-193.

(41) Donoghue, J. F. Sea level history of the northern Gulf of Mexico coast and sea level rise scenarios for the near future. Clim. Change 2011, 107 (1-2), 17-33.

(42) Galushkin, Y. Numerical simulation of permafrost evolution as a part of sedimentary basin modeling: permafrost in the Pliocene-Holocene climate history of the Urengoy field in the West Siberian basin. Canadian Journal of Earth Sciences 1997, 34(7), 935-948.

(43) Liu, X.; Flemings, P. B. Passing gas through the hydrate stability zone at southern Hydrate Ridge, offshore Oregon. Earth Planet. Sci. Lett. 2006, 241 (1), 211-226.

(44) Henry, P.; Thomas, M.; Clennell, M. B. Formation of natural gas hydrates in marine sediments: 2. Thermodynamic calculations of stability conditions in porous sediments. J. Geophys. Res.: Solid Earth 1999, 104 (B10), 23005-23022.

(45) Malinverno, A. Marine gas hydrates in thin sand layers that soak up microbial methane. Earth Planet. Sci. Lett. 2010, 292 (3), 399-408.

(46) Freer, E. M.; Sami Selim, M. Methane hydrate film growth kinetics. Fluid Phase Equilib 2001, 185 (1), 65-75.

(47) Spangenberg, E.; Beeskow-Strauch, B.; Luzi, M., Naumann, R.; Schicks, J. M.; Rydzy, M. The process of hydrate formation in clastic sediments and its impact on their physical properties. In Proceedings of the 6th International Conference on Gas Hydrates 2008

(48) Stoll, R. D.; Bryan, G. M., Physical properties of sediments containing gas hydrates. Journal of Geophysical Research: Solid Earth (1978–2012) 1979, 84(B4), 1629-1634.

(49) Waite, W. F.; Winters, W. J.; Mason, D. H., Methane hydrate formation in partially water-saturated Ottawa sand. American Mineralogist 2004, 89(8-9), 1202-1207.

(50) Priest, J. A.; Best, A. I.; Clayton, C. R., A laboratory investigation into the seismic velocities of methane gas hydrate-bearing sand. Journal of Geophysical Research: Solid Earth (1978–2012) 2005, 110(B4).

(51) Priest, J. A.; Rees, E. V.; Clayton, C. R. (2009). Influence of gas hydrate morphology on the seismic velocities of sands. Journal of Geophysical Research: Solid Earth (1978–2012) 2009, 114(B11).

(52) Schicks, J. M.; Spangenberg, E.; Giese, R.; Steinhauer, B.; Klump, J.; Luzi, M., New approaches for the production of hydrocarbons from hydrate bearing sediments. Energies 2011, 4(1), 151-172.

(53) Waite, W. F.; Spangenberg, E. Gas hydrate formation rates from dissolved-phase methane in porous laboratory specimens. Geophysical Research Letters 2013, 40(16), 4310-4315.

(54) Priegnitz, M.; Thaler, J.; Spangenberg, E.; Rücker, C.; Schicks, J. M. A cylindrical electrical resistivity tomography array for three-dimensional monitoring of hydrate formation and dissociation. Rev. Sci. Instrum. 2013, 84 (10), 104502.

(55) Kashchiev, D.; Verdoes, D.; Van Rosmalen, G. M. (1991). Induction time and metastability limit in new phase formation. Journal of crystal growth, 110(3), 373-380.

(56) Kashchiev, D.; Firoozabadi, A. (2002). Driving force for crystallization of gas hydrates. Journal of crystal growth, 241(1), 220-230.

(57) Kashchiev, D.; Firoozabadi, A. (2002). Nucleation of gas hydrates. Journal of crystal growth, 243(3), 476-489.

(58) Kashchiev, D.; Firoozabadi, A. (2003). Induction time in crystallization of gas hydrates. Journal of crystal growth, 250(3), 499-515.

(59) Kossel, E.; Deusner, C.; Bigalke, N.; Haeckel, M. (2013). Magnetic Resonance Imaging of Gas Hydrate Formation and Conversion at Sub-Seafloor Conditions. Diffusion Fundamentals, 18(15), 1-4.

(60) Kossel, E. GEOMAR, Helmholtz Centre for Ocean Research Kiel, Germany, personal communication, 2014

(61) Gow, A. J.; Williamson, T., Rheological implications of the internal structure and crystal fabrics of the West Antarctic ice sheet as revealed by deep core drilling at Byrd Station. Geological Society of America Bulletin 1979, 87(12), 1665-1677.

(62) Klapp, S. A.; Klein, H.; Kuhs, W. F., First determination of gas hydrate crystallite size distributions using high-energy synchrotron radiation. Geophysical research letters 2007, 34(13).

(63) Collett, T. S.; Dallimore, S. R. Quantitative assessment of gas hydrates in the Mallik L-38 Well, Mackenzie Delta, NWT, Canada. In Proceedings of the 7th International Conference on Permafrost, Yellowknife, Canada 1998.

(64) Werner F. KUHS, W.F.; Chaouachi,M.; Falenty, A.; Sell, K.; Schwarz, J.O.; Wolf, M.; Enzmann, F.; Kersten, M.; Haberthüer, D. In-situ micro-structural studies of gas hydrate formation in sedimentary matrices, Proceedings of the 8th International Conference on Gas Hydrates (ICGH8-2014), Beijing, China, 28 July - 1 August, 2014

5. Publication IV: Gas production from methane hydrate - simulating the multistage depressurization test in Mallik, Canada

Authors:

Katja U. Heeschen, Sven Abendroth, Mike Priegnitz, Erik Spangenberg, Jan Thaler, and Judith M. Schicks

Submitted to:

Environmental Science & Technology

Contribution

The research was planned in collaboration by all authors. Dr. Katja Heeschen and Sven Abendroth analysed the gas and water flow patterns during depressurization. I provided the processed ERT and temperature data. Dr. Erik Spangenberg controlled and analysed the pressure stages applied during the experiments. Dr. Judith Schicks, Jan Thaler, and Sven Abendroth identified the temporal changes of gas hydrate stability inside the sediment sample. Data interpretation was done by all authors. Finally, Dr. Katja Heeschen wrote the manuscript.

Gas production from methane hydrate – simulating the multistage depressurization test in Mallik, Canada

Katja U. Heeschen[1]*, Sven Abendroth [1], Mike Priegnitz[1], Erik Spangenberg[1] , Jan Thaler[1], Judith M. Schicks [1] ,

[1] GFZ German Research Centre for Geosciences, 14473 Potsdam, Germany;

Methane production from natural gas hydrate deposits is in the test phase, models are developed to describe the data, and laboratory experiments are carried out to test the rationale of the conceptual models. The experimental challenges include: I) the simulation of a natural three-phase system of sand-hydrate-liquid with known and high hydrate saturations and II) the simulation of transport behavior as deduced from field data. The GFZ's large scale reservoir simulator (LARS; 210 L sample) allowed for the first simulation of the gas production test from permafrost hydrates at the Mallik drill site (Canada) via multistage depressurization. At the starting position hydrate saturation was as high as 90% formed from dissolved methane only. While gas hydrate dissociation determined the flow patterns in the early pressure stages, the importance of different transport behaviors increased at lower pressure stages and increasing water content. Flow patterns as observed in Mallik were recorded. While the conceptual model in LARS is different at high gas production, it does agree with the model proposed for Mallik at moderate and low gas production showing the value but also the limits of pilot scale tests.

Keywords: gas hydrates; depressurization; methane production, Mallik, pressure vessel, gas flow

1. Introduction

Gas hydrates are ice-like crystalline solids that form from water and guest molecules such as methane (CH_4), the dominant guest molecule in natural gas hydrates.[1-3]. They form at elevated pressure, low temperatures and in the presence of sufficient amounts of water and gas within the sediment package forming nodes, veins, layers or filling the pores.[4-7] The major occurrences are to be found in sediments along the continental margins and permafrost regions.[1,8]

Despite the large variation in the total estimate of carbon bound in gas hydrates of 100 Gt to 400000 Gt [9-12] there is a consensus that this natural gas reservoir is a large source of energy and worthwhile exploring.[13] The permafrost gas hydrates only account for only about 3% of this inventory. [14] However, they are easily accessible and were the target of the first field tests for methane production from gas hydrates at the Mallik site, North West Territories, Canada.[15-17] The tests used thermal stimulation (2001) and depressurization via hydraulic stimulations technics (2002, 2007/08). A very recent test took place in the Nankai Trough, Japan (March 2013) applying depressurization over 6 days and producing a total of 120.000 m³ of gas. [18] In the gas hydrate field trail at Igik Sikumi on the Alaska North Slope carbon dioxide was injected to exchange methane hydrates by carbon dioxide hydrates and subsequent depressurization.[19]

The gas and water flow patterns observed at Mallik in 2008 were described and modelled, e.g., by Uddin et al.[20-22] As their history match using the original version of the numerical reservoir simulator CMG-STARS failed to fit the data, Uddin et al. [21, 22] developed a new set of equations to model the unconventional flow observed during the Mallik production test 2008. Tunable parameters for gas hydrate dissociation and different gas bubble transport models were added. They led to reasonable fits of the gas flow rates and to a lesser extend with the water production. This conceptual and numerical model is inspired by the "foamy oil flow" [21] developed in oil industry for solution gas drive reservoirs without an initial continuous gas phase. [23, 24] During depressurization early and small gas bubbles are transported within the oil/water in a "two-phase" or rather "pseudo-single" flow before the size of the single bubbles due to pressure decrease or coalescence exceeds those of the pore throats. At that point bubbles get trapped and gas production declines rapidly before progressive growth forms a continuous gas phase that allows increasing gas transport.

While a number of one stage depressurization tests have been carried out in smaller (< 10 L) [25-27] or larger pressure vessels (70 – 120 L) [28, 29], the above mentioned model has not been examined experimentally. In the named experiments the formation of gas hydrates was from a gas phase and water producing ≤30% of cementing gas hydrates and residual free gas. In Mallik gas hydrate saturated roughly 80% of the pore volume, was likely of porefilling character with little free gas been present. [15, 30] Uddin et al.[22] themselves cited micromodel studies on bubble formation [31] or degassing experiments using CT-scans [32] to support parts of their proposed process chain.

Based on its large volume and the possibility to form gas hydrate saturations up to 90%, the GFZ's LArge scale Reservoir Simulator, LARS, allows for the simulation of the 2008 Mallik gas

production test via a number of depressurization steps and review the foamy oil approach on laboratory scale under controlled conditions.

2. Geological Setting: Gas production test from gas hydrates at the Mallik test site

The Mallik gas hydrate field in the Canadian Arctic (Beaufort Mackenzie Delta) is characterized by 640 m of permafrost in deltaic sediments deposited since the Mesozoic Era. [15, 33] They are composed of interlayers of sandstone and shale. Gas hydrates occur in three discrete zones below the permafrost at 892 – 930 m (D), 942 – 993 m (B), and 1070 – 1107 m (A) with the deepest gas hydrates coinciding with the lower boundary of the gas hydrate stability zone. Zone A includes two gas hydrate occurrences with saturations of 80 – 90% in unconsolidated to weakly cemented Oligocene sandstones separated by gas hydrate-free siltstones and terminated by a clay layer at the upper boundary. The gas hydrates are underlain with water (class II gas hydrates).[34] See Table 1 for details.

Zone A was the target area for the gas production test at the Mallik drill site 2L-38 in 2007/2008.[16] Over a period of 6.75 days gas was produced from gas hydrates via depressurization in three pressure stages (I – III): 7.1 MPa – 5.0 MPa – 4.2 MPa. The pore pressure was reduced by pumping water and the perforated zone was at 1093-1105 m just above the lower boarder of gas hydrate layer A.[35] During the first pressure stage technical issues frequently interrupted gas flow patterns. Therefore, the interpretation of the observed gas flow pattern is based on pressure stages 4.2 and 5.0 MPa. It was characterized by a strong decrease shortly after the onset of a vigorous gas production followed by a renewed and moderate rise. A conventional two-phase flow would decrease in a moderate fashion after the initial rise. The total production amounted to 12278 m^3 of gas and 66.9 m^3 of water.

3. Methods

To simulate the depressurization procedure of the Mallik field test two repeated experiments have been carried out in LARS. This section gives a short introduction to LARS and the experimental procedure. For details on LARS see Schicks et al.[36] and Priegnitz et al. [37].

3.1. Large Scale Reservoir Simulator (LARS)

LARS was developed to investigate the formation and dissociation of gas hydrates in sediments under simulated *in situ* conditions. It holds a sample at pressures up to 25 MPa and temperatures of -40 to 20°C. There are five core elements to LARS (Fig. 1).

In LARS, confining pressure and temperature are controlled via a confining fluid, which is present in the interspace between the pressure vessel and the neoprene jacket sealing the sample (Fig. 1, right panel). While during formation it acts as a cooling agent (4°C), heat is transported into the sample from the surrounding confining fluid during depressurization to simulate field conditions (11.0°C). This results in the largest heat transport along the sample's boarders.

In experiment A the spatial temperature measurements in LARS have been carried out using 13 spatially distributed Pt100 temperature sensors (platinum resistance thermometers, PRTs; nominal resistance: 100 ohm at 0°C). The sensors were mounted on a plastic mesh within the sample (Fig. 1). In experiment B a fibre-optic distributed temperature sensing (DTS) cable was installed on the plastic mesh as were two additional temperature sensors. The DTS-cable recorded an average temperature over a given distance of 0.5 m with an accuracy of 0.3°C.[38] In total 12 m of this cable were installed.

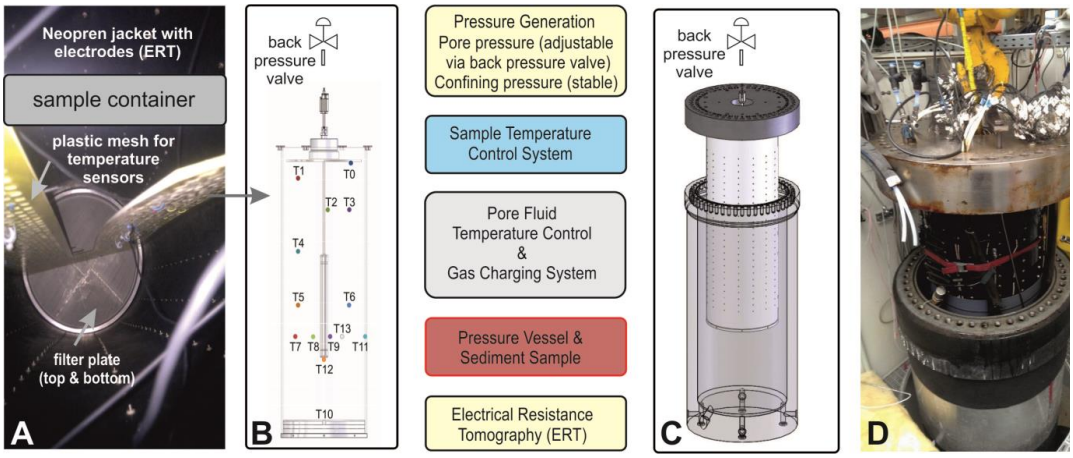

Figure 1: Major components of LARS as listed in the middle: 1) pressure generation system: high-precision pressure syringe pumps (TELEDYNE ISCO) controlling the confining fluid (glycol-water mixture) and the CH_4 pressure for the gas charging system; the porewater pressure was controlled by an additional back pressure valve mounted at the upper outlet of the pressure vessel (B,D); 2) Sample temperature control system: tempers the circulating confining pressure fluid; a heat exchanger is connected to a UNISTAT 510 W circulation thermostat; cooling power: 5kW at 0°C; 3) temperature controlled gas charging system: in a closed loop CH_4 saturated brine enters the sample via a filter plate (A). CH_4 is consumed in hydrate formation. The CH_4-depleted brine exits the sample and re-enters the gas charging vessel; 4) temperature controlled pressure vessel holds with a sediment sample 460 mm in diameter and 1300 mm long (210 L) surrounded by a neoprene jacket (D); a plastic mesh allows for the positioning of temperature sensors in the sample (A, B); 5) Electrical Resistance Tomography (ERT) (375 electrodes mounted in the neoprene jacket; 25 rings; A, C); monitors the resistivity distribution in the specimen, which is altered in the presence of gas hydrate or free gas.

While confining and pore pressure were controlled using TELEDYNE ISCO pumps during the hydrate formation process, the pore pressure was regulated via a backpressure valve during depressurization. The valve was mounted at the top outlet of LARS and allowed for high flow rates at constant pressure. In experiment A the back-pressure valve broke due to the large and short-term changes in fluid flow and pressure had to be controlled by hand. This led to significant pressure variations of up to 0.5 MPa, which in turn led to repeated transitions between gas hydrate stability and instability. All pressure data in this paper originate from recordings of the ISCO Pump's pressure sensor with an error of 3 – 4 bar throughout the duration of the experiment because of drift.

A circulating methane-saturated brine allows for gas hydrate formation from dissolved CH_4, which is supposed to be the gas hydrate formation process in natural sediments.[39, 40] No free gas is present. To avoid early hydrate formation and plugging, the temperature within the charging system is just above the equilibrium temperature at given pressure while conditions in LARS are within the stability field, thus, cooling the brine in the sediment. The bulk hydrate saturations can reach up to 90% of the pore space and can be determined by two methods: a) repeated water sampling and measuring of the electrical conductivity (WTW LF 340; error: 0.5%) as an measurement for the hydrate saturation [41, 42]; b) the ERT data, which can be transferred into a spatial hydrate distribution using a processing routine based on Archie's equations.[37, 43]

The decomposition of the hydrate phase in LARS can be initialized by different production scenarios: depressurization, thermal stimulation using a counter current heat exchange reactor[44], or by introducing chemical substances such as CO_2.[45] During hydrate dissociation, water and gas are produced and separated using a water trap. While the water quantity is irregularly measured by weighing discrete samples, the gas flow is continually quantified using an OMEGA mass flowmeter with a measuring range of 0 - 75 L/min calibrated for methane at 2.5 MPa (FMA 1842-CH4-25BAR).

Currently LARS is getting equipped with a "model-borehole" allowing for different flow pathways and fracking tests in gas hydrate saturated sands.

3.2. Experimental Parameters

The production of gas from methane hydrates was carried out via depressurization with pressure stages similar to those of the Mallik production field test: 7.0 - 5.0 - 4.2 MPa with additional pressure stages at 9.0 and 3.0 MPa in experiment B. These pressure stages are termed 7.0, 5.0, 4.2, and 3.0. The duration of each pressure stage was 2 - 3 hours with a total of 9 hours for the Mallik simulation test.

Subsequently, the backpressure valve was closed and later set to atmospheric conditions (see Priegnitz et al.[43] for details). For details on the experimental parameters see Table 1.

The starting hydrate saturation was formed within 3 month time and determined to be in the range of 90% (conductivity) and 80% (ERT), respectively [43], which is in good agreement considering the error of both methods to be roughly ±10%. The actual volume of gas hydrate was slightly different in the two experiments caused by variations in porosity. The void permeabilities were determined by applying Darcy flow experiments at ambient conditions. Due to the compaction in LARS the permeability will be slightly smaller and was estimated to be 500 D and 1500 D, respectively. The effective permeability at maximum hydrate saturation was measured *in situ* using the fluid flow at the inlet and outlet at given pressure. They were 2 and 5 mD, respectively.

Table 1 Parameter of the Mallik production test and the two experiments mimicking the production test via depressurization in LARS

	Mallik Test site*	**Experiment A**	**Experiment B**
Sediment	Quartz with ~ 10 % clay	Quartz sand	Quartz sand
Grain size		0.01 – 2mm	0.2 – 1 mm
Gas hydrate saturation (Conductivity)	80 – 90%	89.5%	90%
Gas hydrate saturation (ERT-System)		80%	80%
Initial NaCl load		4 g/L	4.5 g/L
Salinity at 90% saturation	3.5 g/L	9.25 g/L	10.5 g/L
Porosity	0.32 – 0.45	0.35	0.392
Total pore volume	does not apply	73.5 L	82.3 L
Pore fluid volume		7.7 L	8.2 L
Initial permeability (0%Sh)*[1]		673±11 D (500 D)*[2]	2030±28 D (1500 D) *[2]
Effective permeability (measured)	2 mD [80 - 90%Sh]	2 mD [90%Sh]	5 mD [90%Sh]
Effective permeability (calculated) ***(Carmen-Kozeny equation)***		0.2 mD [90%Sh] 15 mD [80% Sh] (ck6)	0.7 mD [90%Sh] 47 mD [80%] (ck6)
Pore pressure (initial)	10.9 MPa	11.5 MPa	11.5 MPa
Temperature	12.2 °C	11 °C	11 °C
Depressurization stages [MPa]	7.1 - 5.0 - 4.2	7.0 - 5.0 - 4.2	9.0 - 7.0 - 5.0 - 4.2 – 3.0
Volume gas hydrate [dm^3]		65.78	74.09
Gas in gas hydrate [m^3] *[2]		10.79	12.15
Volume of pore fluid at 90% hydrate saturation [dm^3] *[3]		7.71	8.23

*data from [16]
*[1] Sh = hydrate saturation
*[2] 164 m^3 gas/ 1m^3 gas hydrate sl [3]
*[3] Numbers in brackets are estimates based on the assumption, that the compaction decreased permeability

The initial porewater salinity (A: 4 g NaCl/L (A), B: 4.5 g NaCl/L) in LARS was only slightly higher than in the Mallik drill site but rose during hydrate formation to concentrations of 9.25 g/L (A) and

10.5 g/L (B), respectively. Due to the inhibiting effect of inorganic salts on the hydrate formation, the stability field decreased slightly in accordance with the increasing salt content.[3]

3.3. Gas flow measurements

Whereas the qualitative gas flow pattern was resolved by the gas flow meter, the quantitative measurements were insufficient. In experiment A the flow rate repeatedly exceeded the upper detection limit of 4.5 m^3/h during gas surges. In experiment B the temporal resolution of the recorded data of 60 s (5 s in experiment A) was insufficient especially during short gas surges. Thus, in the discussion we will focus on the gas flow patterns.

4. Results and Discussion

The main goal of this paper is to compare gas flow patterns in LARS experiments with observations during the Mallik production test. To do so, we first present and discuss the temperature evolution and effects on the gas hydrate stability within the specimen at given pressure conditions. Here we focus on experiment A. In the second part we present the observed gas and water flow and discuss drivers in the laboratory tests compared to the Mallik field test mainly based on experiment B. For a detailed discussion on the gas hydrate distribution as interpreted from the ERT dataset see Priegnitz et al.[43]

4.1 Temperature

During the depressurization the temperature is controlled by a) heat transport from the confining fluid (11°C) and b) the endothermic gas hydrate dissociation.

Experiment A

Strong changes in temperature throughout the specimen followed the onset of each of the three depressurization stages (Fig. 2a). Whereas the first drop from 11°C to 9.3°C was smallest (7 MPa), the second drop of 3.1°C was largest (5 MPa). These temperature decreases were immediate for those sensors located in the upper quarter of the specimen (T0, T1, T2, T3) while the signal of other sensors was slightly delayed (T7, T9, T12), expressed in a slight curvature in Fig. 2a. This differentiation also appeared during stage 7.0 when the upper sensors only showed variations in accordance to pressure changes. In stage 5.0 the topmost temperature (T0; Fig. 2) rose right after the initial decrease. While at all other sites the temperature decreased after an intermittent pressure drop, temperatures at T0 increased. This increase was shortly interrupted at the next pressure drop (4.2. MPa) but not changed. At all other sensors this pressure drop induced an immediate temperature decrease of 2.3°C.

Subsequently, the temperature rose throughout the specimen with the largest increase at sensors T0, T1, and T11 at the top and the border of the sample.

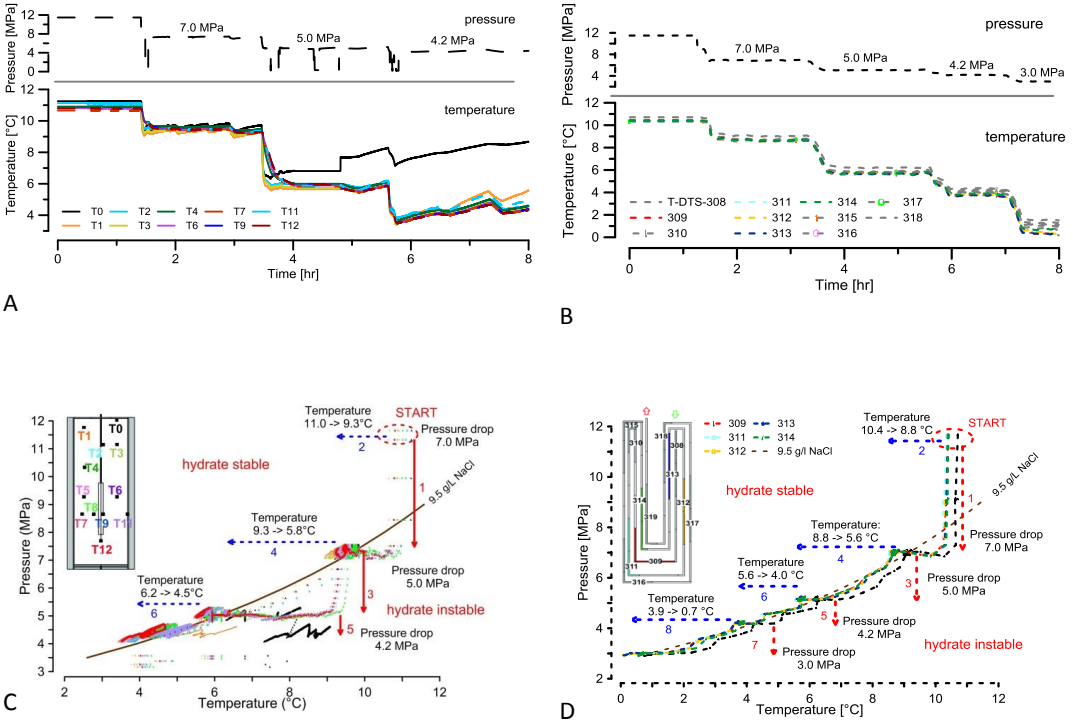

Figure 2 A) Progress of pressure (upper panel) and temperature (lower panel) during experiment A. For the location of the temperature sensors see upper left corner of figure 2c; B) likewise for experiment B with sensor distribution in figure 2d); C) P-T-paths as recorded during experiment A in comparison to calculated methane hydrate stability curves at 9.5g/L NaCl (using CSMGem software)[3]. The red arrows indicate the induced pressure steps and the dashed blue lines the accompanying average temperature changes. The processes are numbered consecutive; D) likewise for experiment B. The spacing of the data is 5 s and 60 s in experiment A and B, respectively.

Experiment B

While the overall courses were similar to experiment A, both, pressure and temperature developments had a smoother outline (Fig. 2b). The variations during pressure stages were significantly smaller and pressure gradients less steep as were the accompanying temperature changes. In addition, the data points using a DTS cable were averages over a length of 50 cm. This likely caused slight differences in temperatures between experiment A and B. In test B the average temperatures were: 8.8°C during stage 7.0, 5.6°C in stage 5.0, and 4.0°C in stage 4.2. The pressure drop 5.0 to 4.2 MPa was executed in two steps as was reflected in the temperature profile. An increase in temperature only occurred at stage

3.0 after the three "Mallik pressure stages". Here the temperature differences within the specimen became significant (0 – 2°C).

4.2 Evaluation of the pressure-temperature development

The temperature profile is closely coupled with the pressure development via the stability field of methane hydrate (Fig. 2c-d). External pore pressure reductions leading to conditions outside the stability field are followed by subsequent endothermic gas hydrate dissociation until reestablishment of pressure-temperature (p-T) stability conditions. Subsequently, minor gas hydrate dissociation compensates for heat transfer from the confining fluid (11°C) allowing p-T conditions in the sample to remain at the hydrate phase equilibrium (Fig. 2c-d). The height of any temperature drop is determined by the deviation from the p-T stability curve. Whether or not stability conditions can be regained depends on the local amount of gas hydrate. The periods of comparably stable p-T conditions throughout the pressure stages are represented by a large number of data at the stability curve in Figures 2 c-d with a slight offset due to the drift in pressure measurements by the ISCO pump. The stronger (external) pressure regulations in experiment A are clearly visible in the greater variance of the data. This effect is enhanced by the reduced spatial resolution of the measurements in experiment B.

The short delay in temperature changes in the lower half of the sample (Fig. 2a) is caused by short-termed pressure gradients between the upper and central area of the specimen occurring during the fast pressure drops of stages 7.0 and 5.0 (experiment A) when effective permeabilities are low in the center. Since in LARS there is only one recorded pressure measurement at the outlet valve, the pressure gradient is expressed as a strong deviation from the hydrate equilibrium curve for T4-T12, whereas paths T0-T3 in the upper part follow the equilibrium curve as expected (Fig. 2c; arrows 1 - 4).

Data from the ERT at the beginning of the experiment showed a comparably even distribution of gas hydrate in the center of the sample (Fig. 3). Next to the enhanced heat transfer at all boundaries, this explains the earlier temperature increase at sensors T0 and T1 located at the top, where p-T conditions are constantly outside the stability conditions early in stages 5.0 and 4.2. This is followed by an increase in T11 situated close to the sample's border (Fig. 2a, 2c). Likewise observations on heat transfer and resistivity changes were reported by Li et al.[27] in a one stage degassing experiment using a 6 L pressure vessel.

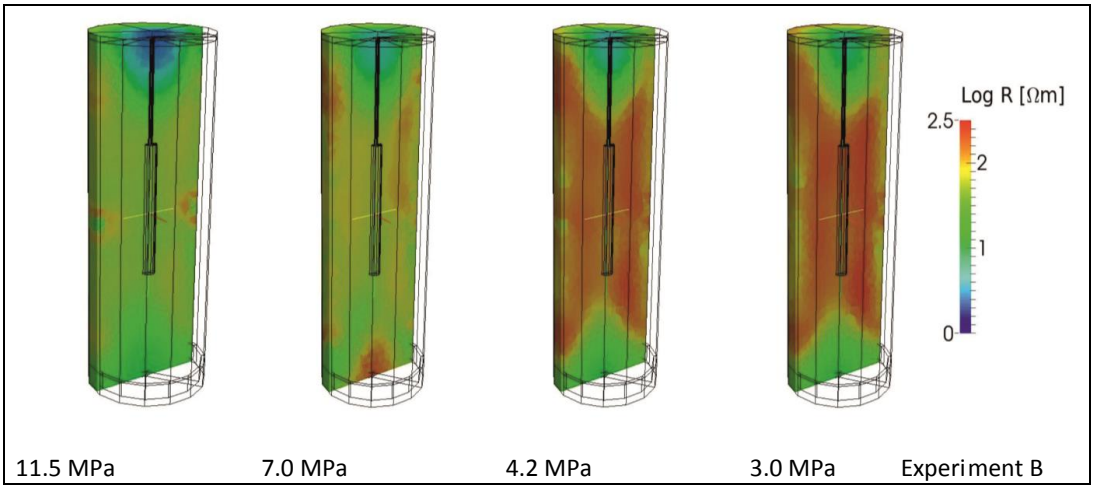

Figure 3 Resistivity distributions in LARS from ERT measurements before and during Mallik pressure stages 7.0, 4.2, and 3.0. Please note that the upper and lower 15 cm of the 137 cm long column are interpolated as there are no electrodes.[37] In addition, the steal lid at bottom and top of the specimen act as good conductors, thus, altering the resistivity in these areas. Before the production the central area shows a uniform and increased resistivity caused by homogenous gas hydrate distribution. In the following, gas production increases the resistivity, whereas water decreases the resistivity. Water pathways along the border are well represented in these ERT measurements.

4.3 Gas and Water Flow

Figure 4 gives an overview of the observed gas and water flow rates and budgets in LARS. While the accuracy of the total gas budgets was insufficient in both experiments (see methods), the gas flow patterns could be resolved. Both, gas and water flow rates had an intermittent and irregular pattern with higher short-termed water flow rates commonly bound to the pressure drops. The production of water was high in stages 7.0 and 5.0 but decreased significantly after this. The spikes in gas flow rates were irregular in timing and duration. While they always occurred just after the increased water production at the pressure drops, they also occur irregularly during the pressure stages particularly of experiment A.

Figure 5 compares the gas flow rates with the concurrent temperature deviation from the methane hydrate equilibrium curve throughout the specimen. There is a close linkage between gas flow and conditions of hydrate instability. While for a short time after each pressure drop gas hydrates are unstable throughout the specimen, the stability conditions are often quick to be re-established by endothermal hydrate dissociation. Flow rates decrease. The areas of maximum deviation, i.e., regions

with higher heat transfer and less gas hydrate volumes take about twice as long to regain equilibrium. These are areas close to the top and boundaries of the specimen (T0, T1, T11) where gas hydrate volumes decrease faster and permeability increases.

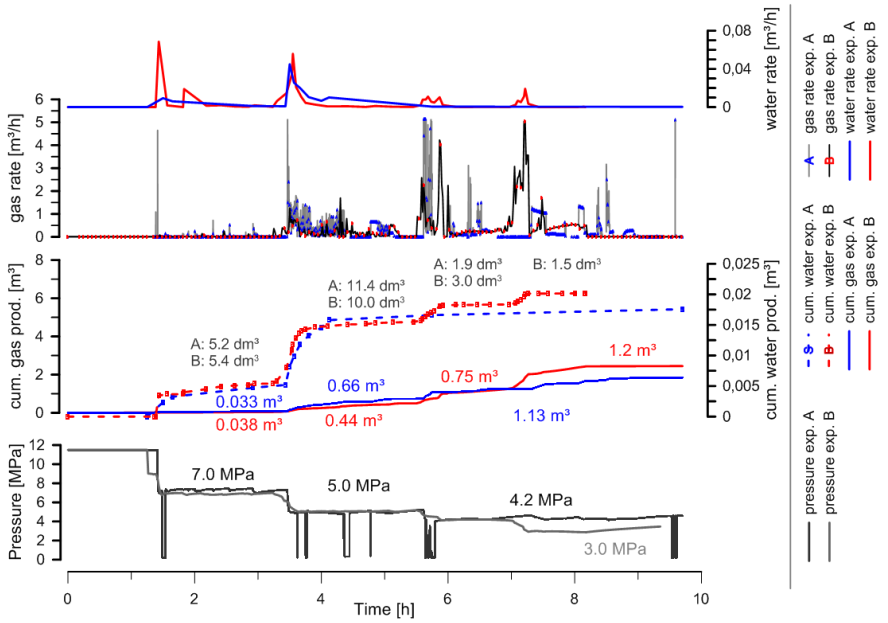

Figure 4 Production rates of gas and water (top panel), cumulative (cum.) gas and water productions (middle panel) and the pressure change over time (lower panel) of the experiments A and B. The numbers in the middle panel name the amount of cumulative gas (A: blue, B: red) and water (grey) per pressure stage

Once equilibrium is regained additional short-term peaks in gas production are induced by pressure variations within the accuracy range of the back pressure valve, which was significantly larger in experiment A as was the gas production during the "constant" pressure stages. Here flow patterns are continuously disturbed by short periods of hydrate dissociastion in regions with maximum deviation (Fig. 5). In experiment B continuous changes in gas flow occur in stage 5.0 despite equilibrium conditions. The interrupted gas flow can result from local gas blockage and accumulation inducing local pressure build-up, which causes subsequent fracturing due to the limited permeability for gas released in areas of high gas hydrate saturation. This process is detected as a sudden pressure release by the pressure sensor located in the outlet tubing. Pressure variations are significantly smaller in later stages when permeability has increased. On a small scale the steady progression of hydrate dissociation and the corresponding gas flow in periods of constant pressure is further altered by the changes in the chemical potential that opposes other drivers if the brine is oversaturated with methane

and gas transport is blogged. In experiment A these processes are masked by external pressure changes.

During the early stages of the experiment (7.0 and 5.0) small gas release rates are compensated by higher water flow rates (Fig. 4). This is especially true for experiment B where pressure drops where more gradual and gas supply for the formation of a continuous gas phase less vigorous. At these low permeabilities gas bubbles rather are attached to the gas hydrate or blogged at pore throats where they expand. They replace the pore-filling water until a continuous gas phase is formed.

In stages 4.2 and 3.0 the water flow is reduced and gas flow patterns in experiment B are different. Here pressure is stable after the actual pressure drop and a small minimum occurs after the early gas surge and before the continuous gas flow increases again in a moderate fashion (Fig. 5).

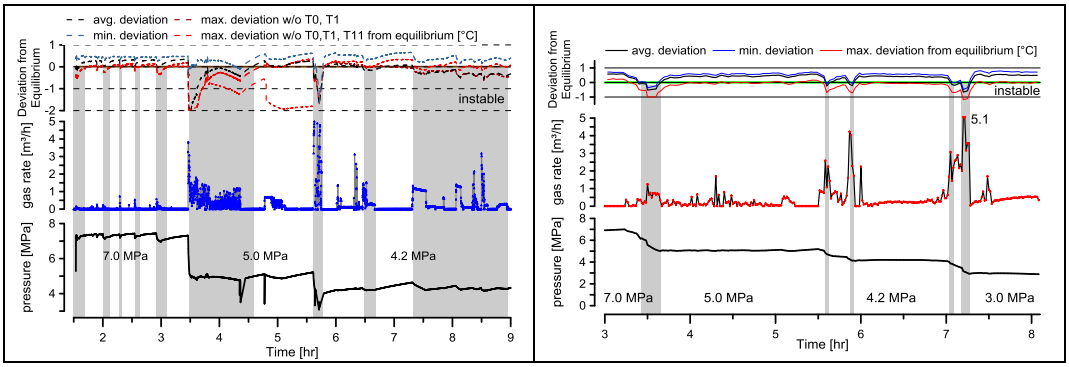

Figure 5 Deviations from the gas hydrate stability calculated by the subtraction of calculated data using CSMGem[3] and those deduced from p-T measurements in LARS (upper panels), measured gas production rates (middle panels) and reservoir pressure (lower panel) over time in LARS during experiment A (left) and B (right). The figure shows minimum, maximum and average deviations in °C using all temperature data enclosed in Fig. 6. For experiment A the maximum deviation (red dashed line) is subdivided further by excluding those sensors that show an early increase in temperature due to the absence of gas hydrates. No gas flow occurred during stage 7.0 in experiment B (see Fig. 4).

4.4 Lessons learned: Comparison with gas flow patterns of the Mallik production test

In the 2008 Mallik production test gas flow patterns were investigated for stages 5.0 and 4.2.[20-22,46] The observed unconventional gas flow behavior was characterized by an initial peak followed by a rapid decline and a subsequent modest rise (Fig. 6)[46]. As pointed out in the introduction this pattern was explained referring to the "foamy oil flow".[20-22,46]

Like solution gas drive reservoirs, gas hydrate reservoirs do not contain a free gas phase but gas bubbles need to nucleate, grow and coalesce before it is being established. Referring to Uddin et al.[21], the initial gas surges at the pressure drop of the Mallik production test are based on the transport of microbubbles within the water once they nucleated and until they get trapped due to their increasing size. As a consequence the gas flow decreases and a consecutive delay in gas production is expressed as a minimum in the time-flow plot (Fig. 6). The following increase occurs once a continuous gas phase has developed due to coalescing bubbles. The absence of free gas and gas hydrate saturations up to 90% in LARS allow for an experimental representation of the Mallik field test unlike other small [26, 27] and larger scale one-stage laboratory production tests[28, 29], which contain a free gas phase to start with.

The gas flow behavior in the LARS tests was unconventional showing two patterns: 1) a pattern with an early gas surge followed by an irregular pattern of spikes in gas flow 2) a pattern similar to the Mallik test with a large gas surge at the beginning followed by a fast decline and a subsequent moderate increase. While the first pattern prevailed throughout all of test A and stage 5.0 of test B, the latter was observed in stages 4.2 and 3.0 of test B. Once equilibrium is reached, the difference in basic flow patterns is based on the length of the gas transport, the permeability/gas hydrate saturation, and the amount of water present in the reservoir, i.e., the importance of transport behavior over hydrate dissociation.

Both stages 7.0 and 5.0 have a high water production despite the differences in gas flow. Up to this point the gas hydrate saturation is particularly high and blocking the specimen's center but is less profound in the upper part of the specimen (Fig. 3). Here, pathways to the perforated upper boundary are short but filled with porewater. Growing gas bubbles need to form a continuous gas phase before being produced. They displace pore-filling water before coalescing and forming pathways for gas flow. The volume of water produced early in stages 7.0 and 5.0 accounts for as much as 20% of the total initial pore space in LARS. Thus, most porewater is lost from the upper part of the specimen where areas of gas-filled pore spaces develop next to residual water. This process might be supported by the migration of water into areas of higher gas hydrate occupancy where capillary pressures are higher owing to the smaller pores. [32] Once gas pathways are established the transport behavior is of minor importance for the gas production compared to gas hydrate dissociation – a phenomena pointed out earlier [26, 27, 29] for depressurization experiments using a four-phase system of gas-brine-hydrate-sediment. However, in the proposed “foamy oil effect” model for Mallik gas transport behavior is an

essential parameter[21]; particularly the change in transport behavior during the course of a pressure stage including the pressure decrease and the period of stable pressure conditions.

While in experiment A the equilibrium could not be accomplished and rapid gas supply has overprinted patterns based on gas transport behavior, the pressure regulation was successful in experiment B. Here gas flow patterns in stages 3.0 and 4.2 are similar to Mallik pressure stages 5.0 and 4.2. In both cases the flow behavior has a significant influence; however, the transport mechanisms are different during times of deviation from the equilibrium. While Uddin and coworkers [21, 46] developed a model of microbubble transport to cause the early gas surges, it is the immediate formation of a continuous gas phase that causes the large gas surges in LARS. See Figure 6 for the conceptual model.

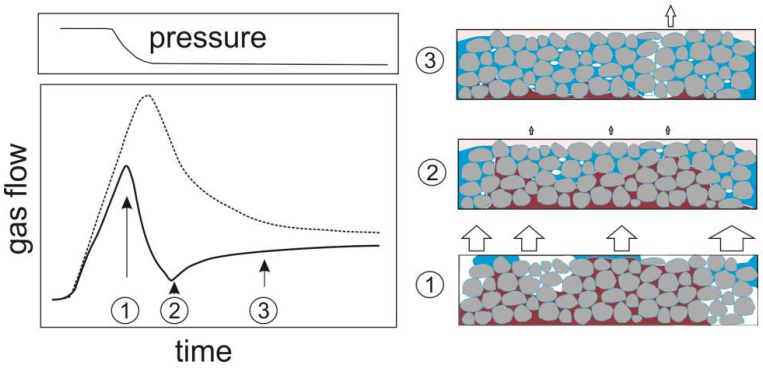

Figure 6 left: Sketch of the hydraulic signal of classical (dotted line) and unconventional reservoir response (solid line) after Wright et al [46]; right: conceptual model of the degassing in LARS during the depressurization stages 4.0 and 3.0 in experiment B; water: blue, sediment: light gray; gas: white; gas hydrate: red.

The reason for both, similarities and differences, lies in the amount of water being present and being produced, respectively. In the Mallik stages 5.0 and 4.2 water flow rates before and after the early gas surge were high but gas:water ratios settled at roughly 150 – 250 (5.0) and 100 – 170 (4.2) once gas flow started to settle. In LARS water production was high only before the gas surge and the trend of the gas:water ratio was reversed: water production lessened severely while gas production continued to be high in stages 4.2 and 3.0. The total production ratios of gas:water were below 60 during stages 7.0 and 5.0 and increased to 250 – 800. Water from the dissociating gas hydrate remained in the reservoir. In LARS there is no external water supply as there is in Mallik where gas hydrates are underlain by free water and water production is the means by which the pressure is reduced within the borehole. If not the sediment, the borehole is filled with water or a water-gas mixture rather than a free gas phase.

In LARS test B a total of 15 L water was produced in the early pressure stages and only 4.5 L in the later. A total of 54 L remained in the sample, an equivalent of 2/3 of the total pore space. While there is not enough water to produce a gas surge from a microbubble-water phase, there is enough remaining water to interfere with the gas transport in the sediment.

In stages 4.2 and 3.0 water is accumulating and filling pore spaces. Once gas hydrate dissociation is reduced due to the re-establishment of hydrate stability conditions in large parts of the sample, gas production decreases and single rising bubbles formed by the residual dissociation grow until they are too large to pass the pore throats (Fig.6); just as proposed for the Mallik production test. With time bubbles coalesce to form a continuous gas phase allowing for moderate increase in gas flow. A slight difference between lab and field data is expressed in the depth of the gas flow minimum (Fig. 6) that is less pronounced in the lab data. This is due to part of the remaining gas hydrate being closer to the top of the specimen where transport pathways are short. The major dissociation in stages 4.2 and 3.0, however, is happening at the center and bottom of the reservoir, where water is accumulating due to gravity and higher capillary forces. [32] The permeability is less of a factor compared to stages 7.0 and 5.0 where gas hydrate volumes are still very high.

Experiments in LARS, where there is no free gas at the beginning, initial gas hydrate concentrations are high, and volumes are large allows for the simulation of a multistage methane production scenario from class II gas hydrates with no free gas being present. Some limitations still apply including a possible shift in pressure levels (Mallik 5.0 and 4.2 relate to LARS 4.2 and 3.0), the different amounts of water being present or delivered from deeper layers, and the different length of the pathways including the water-filled borehole. These differences in water households may lead to a buffering effect in Mallik that we do not see in LARS. However, the importance of the transport mechanism is accounted for in both tests. Whether or not microbubbles account for the gas surge during the pressure drops in Mallik could neither be declined nor supported. In LARS the model does not apply despite the gas flow patterns being similar; unlike the water flow.

Acknowledgments

We are very thankful to Ronny Giese and Alexander Reichardt as well as the team from the workshop for their indispensable help. The German Federal Ministry of Economy and Technology provided funding for this work through Research Grant 03SX320E.

References

1. Kvenvolden, K. A.; Lorenson, T. D., The Global Occurrence of Natural Gas Hydrate. In *Natural Gas Hydrates: Occurrence, Distribution, and Detection*, American Geophysical Union: 2001; pp 3-18.
2. Sloan, E. D., Fundamental principles and applications of natural gas hydrates. *Nature* **2003,** *426*, (6964), 353-363.
3. Sloan Jr, E. D.; Koh, C. A., *Chlathrate Hydrates of Natural Gases*. 3rd ed.; CRC Press: Boca Raton, 2008; p 721.
4. Kvenvolden, K. A., A review of the geochemistry of methane in natural gas hydrate. *Organic Geochemistry* **1995,** *23*, (11), 997-1008.
5. Trehu, A. M.; Long, P. E.; Torres, M.; Bohrmann, G.; Rack, F.; Collett, T.; Goldberg, D.; Milkov, A.; Riedel, M.; Schultheiss, P., Three-dimensional distribution of gas hydrate beneath southern Hydrate Ridge: constraints from ODP Leg 204. *Earth and Planetary Science Letters* **2004,** *222*, (3), 845-862.
6. Bahk, J.-J.; Kim, D.-H.; Chun, J.-H.; Son, B.-K.; Kim, J.-H.; Ryu, B.-J.; Torres, M.; Riedel, M.; Schultheiss, P., Gas hydrate occurrences and their relation to host sediment properties: results from second Ulleung Basin Gas hydrate drilling expedition, east sea. *Marine and Petroleum Geology* **2013,** *47*, 21-29.
7. Boswell, R.; Collett, T. S.; Frye, M.; Shedd, W.; McConnell, D. R.; Shelander, D., Subsurface gas hydrates in the northern Gulf of Mexico. *Marine and Petroleum Geology* **2012,** *34*, (1), 4-30.
8. Kvenvolden, K. A.; Claypool, G. E. *Gas hydrates in oceanic sediment*; 2331-1258; US Geological Survey: 1988.
9. Archer, D.; Buffett, B.; Brovkin, V., Ocean methane hydrates as a slow tipping point in the global carbon cycle. *Proceedings of the National Academy of Sciences* **2009,** *106*, (49), 20596-20601.
10. Burwicz, E. B.; Rüpke, L.; Wallmann, K., Estimation of the global amount of submarine gas hydrates formed via microbial methane formation based on numerical reaction-transport modeling and a novel parameterization of Holocene sedimentation. *Geochimica et Cosmochimica Acta* **2011,** *75*, (16), 4562-4576.
11. Wallmann, K.; Pinero, E.; Burwicz, E.; Haeckel, M.; Hensen, C.; Dale, A.; Ruepke, L., The global inventory of methane hydrate in marine sediments: A theoretical approach. *Energies* **2012,** *5*, (7), 2449-2498.
12. Pinero, E.; Marquardt, M.; Hensen, C.; Haeckel, M.; Wallmann, K., Estimation of the global inventory of methane hydrates in marine sediments using transfer functions. *Biogeosciences* **2013,** *10*, (2), 959-975.
13. Boswell, R., Is gas hydrate energy within reach? *Science* **2009,** *325*, (5943), 957-958.
14. Makogon, Y. F., Natural gas hydrates – A promising source of energy. *Journal of Natural Gas Science and Engineering* **2010,** *2*, (1), 49-59.
15. Dallimore, S. R.; Collett, T. S., Summary and implications of the Mallik 2002 Gas Hydrate Production Research Well Program. In *Scientific Results from Mallik 2002 Gas Hydrate Production Research Well Program, Mackenzie Delta Northwest Territories, Canada*; Geological Survey of Canada: Ottawa, Canada, 2005.
16. Dallimore, S. R.; Yamamoto, K.; Wright, F.; Bellefleur, G. *Scientific results from the JOGMEC/NRCan/Aurora Mallik 2007-2008 gas hydrate production research well program, Mackenzie Delta, Northwest Territories, Canada*; Geological Survey of Canada: Ottawa, Canada, 2012.
17. Yamamoto, K.; Dallimore, S., Aurora-JOGMEC-NRCan Mallik 2006-2008 gas hydrate research project progress. *Natural Gas & Oil* **2008,** *304*, 285-4541.
18. Yamamoto, K.; Terao, Y.; Fujii, T.; Ikawa, T.; Seki, M.; Matsuzawa, M.; Kanno, T. In *Operational overview of the first offshore production test of methane hydrates in the Eastern Nankai Trough*, Offshore Technology Conference; Houston, TX, USA, 2014.
19. Lee, W. S.; White, M. In *Guestmolecule exchange kinetics for the 2012 Ignik SikumiGas Hydrate Field Trial;* Offshore TechnologyConference, Houston, TX, USA; 2014.
20. Uddin, M.; Coombe, D.; Law, D.; Gunter, B., Numerical Studies of Gas Hydrate Formation and Decomposition in a Geological Reservoir. *Journal of Energy Resources Technology* **2008,** *130*, (3), 032501-032501.
21. Uddin, M.; Wright, F.; Coombe, D., Numerical Study of Gas Evolution and Transport Behaviours in Natural Gas-Hydrate Reservoirs. *Journal of Canadian Petroleum Technology* **2011,** *50*, (1), 70-89.
22. Uddin, M.; Wright, J. F.; Dallimore, S. R.; Coombe, D., Gas hydrate production from the Mallik reservoir: numerical history matching and long-term production forecasting. In *Scientific results from the JOGMEC/NRCan/Aurora Mallik 2007-2008 Gas Hydrate Production Research Well Program, Mackenzie Delta, Northwest Territories, Canada*, Dallimore, S. R.; Yamamoto, K.; Wright, J. F.; Bellefleur, G., Eds. Geological Survey of Canada, Bulletin: 2012; Vol. 601, pp 261-289.
23. Sheng, J. J.; Maini, B. B.; Hayes, R. E.; Tortike, W. S., Critical Review of Foamy Oil Flow. *Transport in Porous Media* **1999,** *35*, 157–187.
24. Maini, B. B., Foamy-oil flow. *Journal of petroleum technology* **2001,** *53*, (10), 54-64.
25. Yousif, M. H.; Abass, H. H.; Selim, M. S.; Sloan, E. D., Experimental and Theoretical Investigation of Methane-Gas-Hydrate Dissociation in Porous Media. **1991**.
26. Tang, L.-G.; Li, X.-S.; Feng, Z.-P.; Li, G.; Fan, S.-S., Control Mechanisms for Gas Hydrate Production by Depressurization in Different Scale Hydrate Reservoirs. *Energy & Fuels* **2007,** *21*, (1), 227-233.

27. Li, X.-S.; Zhang, Y.; Li, G.; Chen, Z.-Y.; Wu, H.-J., Experimental Investigation into the Production Behavior of Methane Hydrate in Porous Sediment by Depressurization with a Novel Three-Dimensional Cubic Hydrate Simulator. *Energy & Fuels* **2011,** *25*, (10), 4497-4505.
28. Zhou, Y.; Castaldi, M. J.; Yegulalp, T. M., Experimental Investigation of Methane Gas Production from Methane Hydrate. *Industrial & Engineering Chemistry Research* **2009,** *48*, (6), 3142-3149.
29. Li, G.; Li, B.; Li, X.-S.; Zhang, Y.; Wang, Y., Experimental and Numerical Studies on Gas Production from Methane Hydrate in Porous Media by Depressurization in Pilot-Scale Hydrate Simulator. *Energy & Fuels* **2012,** *26*, (10), 6300-6310.
30. Spangenberg, E.; Priegnitz, M.; Heeschen, K.; Schicks, J. M., Are Laboratory-Formed Hydrate-Bearing Systems Analogous to Those in Nature? *Journal of Chemical & Engineering Data* **2014,** *60*, (2), 258-268.
31. Katsuki, D.; Ohmura, R.; Ebinuma, T.; Narita, H., Methane hydrate crystal growth in a porous medium filled with methane-saturated liquid water. *Philosophical Magazine* **2007,** *87*, (7), 1057-1069.
32. Kneafsey, T. J.; Tomutsa, L.; Moridis, G. J.; Seol, Y.; Freifeld, B. M.; Taylor, C. E.; Gupta, A., Methane hydrate formation and dissociation in a partially saturated core-scale sand sample. *Journal of Petroleum Science and Engineering* **2007,** *56*, (1–3), 108-126.
33. Dallimore, S. R.; Uchida, T.; Collett, T., *Scientific Results from the JAPEX/JNOC/GSC Mallik 2L-38 Gas Hydrate ResearchWell, Mackenzie Delta, Northwest Territories, Canada.* Geological Survey of Canada: Ottawa, 1999; Vol. Bulletin 544.
34. Moridis, G. J.; Collett, T.; Boswell, R.; Kurihara, M.; Reagan, M.; Koh, C. A.; Sloan Jr, E. D., Towards production from gas hydrates: current status, assessment of resources, and simulation-base evaluation of technology and potential. *SPE Reservoir Evaluation & Engeneering* **2009,** *12*, (5), 745-770.
35. Rojas, M.; Martin, C.; Hernandez-Johnson, L.; Ashford, D.; Wright, J.; Yamamoto, K.; Numasawa, M.; Dallimore, S.; Isted, R., Electric submersible pump as an effective artificial lift method to control bottom-hole pressure in a producing gas hydrate well, JOGMEC/NRCan/Aurora 2007–2008 Mallik Gas Hydrate Production Research Well Program. In *Scientific results from the JOGMEC/NRCan/Aurora Mallik 2007-2008 Gas Hydrate Production Research Well Program, Mackenzie Delta, Northwest Territories, Canada*, Dallimore, S. R.; Yamamoto, K.; Wright, J. F.; Bellefleur, G. G. S. o. C., Bulletin: 2012; Vol. 601, Eds. Geological Survey of Canada: Ottawa, 2012; Vol. Bulletin 601, pp 67-76.
36. Schicks, J. M.; Spangenberg, E.; Giese, R.; Steinhauer, B.; Klump, J.; Luzi, M., New Approaches for the Production of Hydrocarbons from Hydrate Bearing Sediments. *Energies* **2011,** *4*, 151-172.
37. Priegnitz, M.; Thaler, J.; Spangenberg, E.; Rücker, C.; Schicks, J. M., A cylindrical electrical resistivity tomography array for three-dimensional monitoring of hydrate formation and dissociation. *Review of Scientific Instruments* **2013,** *84*, (10), 104502.
38. Henninges, J.; Huenges, E.; Burkhardt, H., In situ thermal conductivity of gas-hydrate-bearing sediments of the Mallik 5L-38 well. *Journal of Geophysical Research: Solid Earth* **2005,** *110*, (B11206).
39. Waite, W. F.; Santamarina, J. C.; Cortes, D. D.; Dugan, B.; Espinoza, D.; Germaine, J.; Jang, J.; Jung, J.; Kneafsey, T. J.; Shin, H., Physical properties of hydrate-bearing sediments. *Reviews of Geophysics* **2009,** *47*, (4).
40. Haacke, R. R.; Westbrook, G. K.; Hyndman, R. D., Gas hydrate, fluid flow and free gas: Formation of the bottom-simulating reflector. *Earth and Planetary Science Letters* **2007,** *261*, (3), 407-420.
41. Spangenberg, E.; Kulenkampff, J., Influence of methane hydrate content on electrical sediment properties. *Geophysical research letters* **2006,** *33*, (24).
42. Spangenberg, E.; Kulenkampff, J.; Naumann, R.; Erzinger, J., Pore space hydrate formation in a glass bead sample from methane dissolved in water. *Geophysical Research Letters* **2005,** *32*, (24).
43. Priegnitz, M.; Thaler, J.; Spangenberg, E.; Schicks, J. M.; Schrötter, J.; Abendroth, S., Characterizing electrical properties and permeability changes of hydrate bearing sediments using ERT data. *Geophysical Journal International* **2015,** *202*, (3), 1599-1612.
44. Schicks, J. M.; Spangenberg, E.; Giese, R.; Luzi-Helbing, M.; Priegnitz, M.; Beeskow-Strauch, B., A counter-current heat-exchange reactor for the thermal stimulation of hydrate-bearing sediments. *Energies* **2013,** *6*, (6), 3002-3016.
45. Bigalke, N.; Deusner, C.; Kossel, E.; Schicks, J.; Spangenberg, E.; Priegnitz, M.; Heeschen, K.; Abendroth, S.; Thaler, J.; Haeckel, M. In *Hydraulic and Mechanical Effects from Gas Hydrate Conversion and Secondary Gas Hydrate Formation during Injection of CO2 into CH4-Hydrate-Bearing Sediments*, AGU Fall Meeting Abstracts; 2014; p 0028.
46. Wright, F.; Uddin, M.; Dallimore, S. R.; Coombe, D. In *Mechanism of gas evolution and transport in a producing gas hydrate reservoir: an unconventional basis for successful history matching of observed production flow data*, Proceedings of the 7th International Conference on Gas Hydrates. Edinburgh, Scotland, United Kingdom; 2011.

6. Conclusion

With this study I contribute to the general scientific understanding of the physical properties of hydrate bearing sediments during hydrate formation and dissociation cycles. In order to answer the research questions formulated in section 1.4, this chapter intends to summarize and discuss the main conclusions which can be drawn from the studies presented in chapters 2-5.

6.1. Discussion

To form pore filling hydrates from methane dissolved in water, methane-loaded brine is circulated through a sediment sample. To avoid hydrate-plugging within the fluid flow capillaries it is necessary to keep the temperature within the tubings above the hydrate stability temperature at given pressure. The temperature inside the sediment sample, however, has to be within the gas hydrate stability field to permit hydrate formation to initiate. This procedure requires a significant size of any experimental setup to allow for the establishment of temperature gradients from the inlet fluid flow capillaries into the sediment.
The experimental setup LARS is a worldwide unique setup to investigate formation and production scenarios on a large laboratory scale. Unlike in smaller experimental devices (e.g. Spangenberg et al. [2005]) the size of LARS enables to establish and control temperature gradients on a regular and reliable basis. In early LARS experiments those features were already used to create pore filling hydrate saturated sediment samples [Schicks et al. 2011, 2013]. In order to properly analyse hydrate formation and dissociation experiments, those experiments lacked of information on the spatial hydrate distribution resulting in the first important research question:

- Can the spatial hydrate distribution within LARS be resolved using remote sensing methods?

A self-made electrical resistivity tomography (ERT) array composed of 375 electrodes was successfully developed. With 93.1% of the measured data satisfying the required data quality, the developed instrumentation yields very good data quality. For the very first time it became possible to monitor and visualize the spatial hydrate distribution during hydrate formation experiments. To assess the spatial resolution of the developed ERT array, a smaller scale replica setup was designed. A sewer pipe was equipped with 375 electrodes simulating the LARS ERT in a scale of 1:2 (Fig. 6.1, left). This setup allowed for ERT measurements at ambient conditions and offered the opportunity to place test bodies in the sediment sample. Conductive

aluminium and isolating plexiglass plugs having a dimater of 2.5 cm and lengths of 3, 5, and 10 cm, respectively, were used as test bodies (Fig. 6.1, middle). ERT measurements were performed for the conductive and for the isolating case. The resulting ERT results were upscaled to estimate the spatial resistivity of the ERT array installed in LARS (Fig. 6.1, right). Given the inversion parameters chosen throughout all applications in this thesis, the spatial resolution was found to be in the order of 5 - 10 cm. Though the spatial resolution of the ERT cannot resolve processes on a microscopical scale, it resolves heterogeneous hydrate distribution on a reliable basis. Due to the significant contrast of brine and hydrate conductivity,

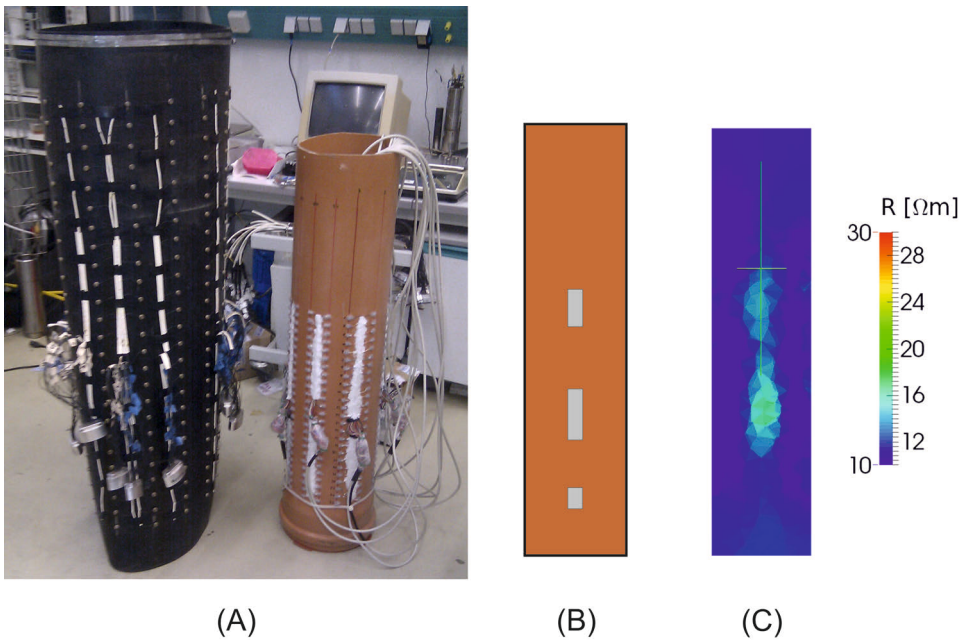

Figure 6.1.: Replica ERT setup to estimate the spatial resolution of the LARS ERT array. A: Photograph of LARS and replica ERT setups. B: Scetch of the cylindrical test bodies placed in the sediment sample. Size of the test bodies from the top to the bottom [cm]: 2.5 x 6, 2.5 x 10, 2.5 x 3. C: Resulting ERT image for isolating plexiglass plugs.

the changes in electrical resistivity caused by the presence of hydrates permit the detection of even small amounts of gas hydrate. The used measurement unit allowed a maximum measurement frequency of 25 Hz, resulting in an overall duration of ≈35 minutes for one complete measurement run. This measurement duration is sufficient in order to monitor the changes of electrical resistivity during hydrate formation experiments. With hydrate formation rates of ≈2% per day the hydrate formation process in LARS is sufficiently slow to permit very good temporal resolution. On the contrary, changes due to hydrate decomposition processes can occur very fast (in the order of seconds to minutes). Hydrate dissociation experiments can thus not be monitored with a satisfying temporal resolution. However, constant pressure stages in depressurization experiments can be recorded to obtain a qualitative impression of the resistivity distribution within the sediment sample.

Though the monitored changes of electrical resistivity already provide a great qualitative impression on the changing hydrate content within the sediment sample, the second research question arose from the previous findings:

- Can the spatial resistivity distribution be used to estimate and quantify the spatial hydrate distribution?

I created a data processing routine that transfers the electrical resistivity distribution into the spatial distribution of hydrate saturation. As a result, this routine not only gives a qualitative impression of the spatial hydrate distribution, but allows to follow the local changes of hydrate saturation throughout the sediment sample. This kind of data is extremely useful as it can subsequently serve as input data for numeric modelling approaches in order to history-match the experiments in LARS. The data processing routine is based on Archie's equations. The best results were obtained using the Archie$_{var-phi}$ approach which interprets the increasing hydrate phase as part of the sediment grain framework, ultimately reducing the sample's porosity. Applying this routine to the recorded ERT data provided valuable insights on where and how hydrate formation initiated and progressed (see chapter 3). As the required methane supply depends on mass transport, the spatial hydrate distribution inside the sample is controlled by the hydrologic flow in addition to the host sediment [Weinberger et al. 2005]. To learn more about the fluid flow changes during hydrate formation I extended the data processing routine in order to provide estimates of local permeability changes throughout the sediment sample. To do so, the prior determined values of local hydrate saturation were used as input data for the pore filling Carman-Kozeny equation [Carman 1956; Kleinberg et al. 2003]. It turned out that the results of this calculation only provide a very rough estimate of the permeability distribution inside the sediment. Nevertheless, those results give a good qualitative impression of the hydraulic changes which can subsequently be used to design specific decomposition experiments.

Compared to smaller scale, high resolution measurement systems (e.g. Kossel et al. [2013]), sites of hydrate nucleation cannot be resolved using the ERT array in LARS. However, the changes of electrical resistivity throughout the sediment sample provide an indication where hydrate formation initiates. Figure 6.2 visualizes the resistivity changes in the first 24 hours of the formation experiment inside the specimen (methane loaded brine was injected from the top). Even though the changes are only in the order of several Ωm, it can be seen that resistivity changes occur in discrete areas. Generally, not one but several areas displayed increased resistivities due to hydrate formation and seem to be randomly distributed. This is in good agreement with the studies of Linga et al. [2009] who observed several hydrate nucleation events in their small scale apparatus. The majority of the resistivity changes was observed in the boundary regions of the specimen where the driving forces were biggest due to active cooling from the surrounding. Figure 6.3 shows the spatial resistivity distribution as hydrate formation continues. The ERT images revealed that with increasing hydrate saturation, however, methane hydrate started to accumulate in the upper parts of the sample. In order to assess the position of the observed hydrate

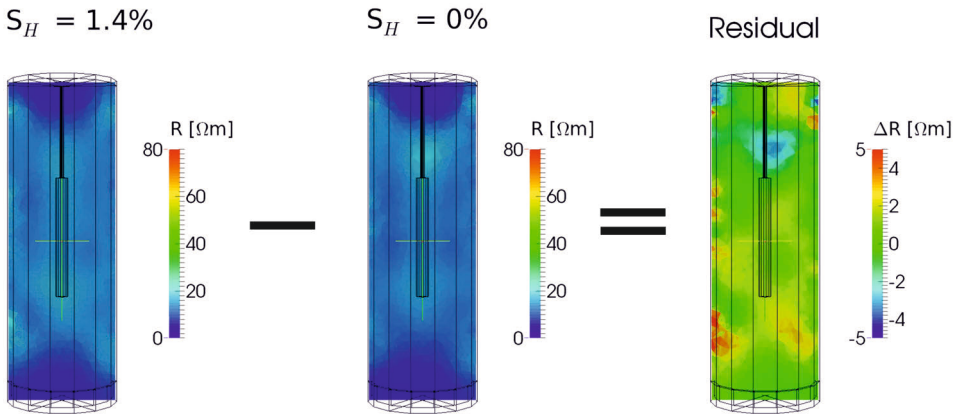

Figure 6.2.: Electrical resistivity changes during the first 24 hours of the hydrate formation experiment. Methane loaded brine is injected from the top. Areas of increased resistivity indicate sites of initiating hydrate formation.

accumulations compared to the spatial extent of the GHSZ, the temperature inside the sample got modelled based on the fluid flow velocities and temperatures applied in the experiments. The boundary of the GHSZ is marked by the 13.3°C isotherm at given pressure in figure 6.3 (right), showing that the areas of increased resistivity correspond to the boundary of the gas hydrate stability field. While initial hydrate formation was observed at a number of randomly distributed sites within the sample, the specific accumulation close to the boundary of the GHSZ is suggested to be due to two reasons: the limited amounts of methane available in the lower parts of the reservoir and the decreased methane solubility in the presence of hydrate. While the methane loaded brine was circulated from the top to the bottom of the specimen, methane was consumed in hydrate formation. Thus, the methane concentration in the pore fluid was significantly lower in the lower parts of the reservoir compared to areas close to the fluid inlet [Waite and Spangenberg 2013]. Furthermore, the solubility of methane decreases in the presence of hydrate [Waite et al. 2009]. Therefore, the methane concentration in the liquid phase decreased as soon as first hydrates formed in the upper parts of the reservoir. The released gas got incorporated in further hydrate formation, suggesting increasing hydrate accumulations along the concentration gradient towards the boundary of the GHSZ.

Because the theoretical boundary of the spatial hydrate stability field corresponded very well to the areas of increased hydrate saturation, the ERT results suggest that we have great control on the vertical position where hydrates accumulate within the sediment sample. This is a valuable finding because it shows that future experiments can be adjusted in order to mimic specific scenarios properly.

Up to this point, it was possible to visualize and quantify the artificially formed hydrate phase within our experimental setup LARS. However, the following research question remained in order to evaluate the obtained results:

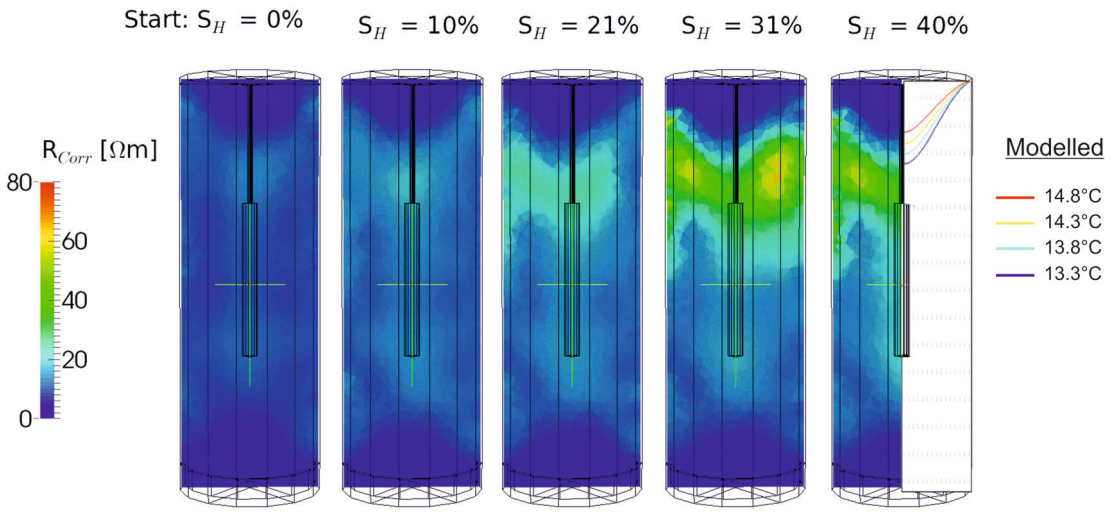

Figure 6.3.: ERT results monitoring ongoing hydrate formation. The electrical resistivity increased in the upper parts of the reservoir indicating severe hydrate accumulations. For a bulk hydrate saturation of 40%, the resistivity distribution is compared to modelled temperature data (right), showing that the hydrate distribution corresponds to the upper boundary of the GHSZ. The hydrate stability temperature at given pressure is 13.3°C.

- Are the results obtained in LARS comparable and transferable to natural gas hydrate deposits?

Chapter 4 presented conceptual models of hydrate formation which suggest that the different kinds of hydrate growth habits (see section 1.3) can be found in natural hydrate deposits. The occurrence of a specific growth habit, however, is controlled by the state of methane. If the methane concentration exceeds the methane solubility of the pore water during its migration towards the GHSZ, or for gas hydrate deposits underlain by mobile gas, both a methane gas phase and water are present in the GHSZ. If sufficient amounts of gas are present within the GHSZ, the available pore water can be consumed in hydrate formation, creating partially water-saturated layers. As a result, hydrate would form in a grain-coating/cementing manner [Waite et al. 2004].
However, it is assumed that most natural hydrate deposits form from methane dissolved in water in the absence of free methane gas [Buffett and Zatsepina 2000]. For such scenarios, methane loaded pore water is undersaturated until it enters the GHSZ. Inside the GHSZ, the methane concentration exceeds the methane solubility resulting in pore filling hydrate formation (e.g. Spangenberg et al. [2005]).
Because the experiments performed in LARS aimed on simulating natural hydrate deposits, pore filling hydrate from methane dissolved in water was generated in all experiments throughout this thesis. In addition, medium to coarse quartz sand was used in all LARS experiments. Hence, the artificially created sediment sample showed permeabilities of several hundreds of Darcys [Priegnitz et al. 2015] which

is up to two orders of magnitude higher than permeabilities observed in natural hydrate bearing sediments. As a consequence, the fluid flow rates inside the LARS sediment are very high, resulting in unrealistic rates of methane supply. The increased mass transport directly affects the observed hydrate formation rates. The hydrate formation rates of 1-2% per day in LARS are $\approx 5 \times 10^7$ times faster than the formation rates assumed to occur in nature Rempel and Buffett [1997]. Those high growth rates in hydrate formation experiments are suggested to produce small crystallites, as Klapp et al. [2007] showed that the grain size distribution of synthetic hydrate can be up to one order of magnitude smaller compared to naturally formed hydrate crystallites. Furthermore, they indicated that crystallite sizes of natural hydrates possibly increase with depth, which would suggest a correlation between crystallite size and age. Since evidences of hydrate recrystallization were observed in earlier experiments [Spangenberg et al. 2005], the ERT data was used in order to assess the influence of hydrate recrystallization on the electrical properties of the sediment. After the hydrate formation experiment was finished, the fluid circulation was stopped and the specimen was held at a constant temperature. The ERT measurements were subsequently continued for 4 days to monitor the resistivity changes throughout the specimen. The ERT results revealed that the resistivity decreased by several Ωm in the areas of significant hydrate saturation. This finding demonstrates that results of hydrate decomposition experiments might become blurred if they were started right after finishing the hydrate formation process. To avoid any blurring effects in the following dissociation experiments, the entire LARS was shut at given PT conditions for at least one week after finishing the hydrate formation process.

After that period it was possible to perform depressurization experiments to answer the following research question:

- How do gas flow patterns of hydrate dissociation experiments in LARS compare to field data?

The results investigating the production behaviour of a hydrate saturated sediment sample in two hydrate dissociation experiments were presented in chapter 5. In both experiments hydrate decomposition was initiated by pressure reduction following the pressure levels applied in the 2007/2008 Mallik field test [Dallimore et al. 2012]. Each pressure drop was accompanied by an immediate temperature drop throughout the entire sample due to the physical temperature-pressure relationship and the endothermic nature of gas hydrate dissociation. Furthermore, each pressure drop induced a massive peak in gas flow, which tended to decline with increasing time. The first two pressure stages also caused significant amounts of water to be produced: As long as very limited hydrate free pore space was available, the released amounts of free gas pushed water towards the pressure gradient to the production site. As hydrate decomposition continued, hydrate free and partly gas filled pore space became available and allowed the remaining water to migrate into lower parts of the reservoir following gravity.
As the produced amounts of water were not re-injected in the performed experiments, the fully water saturated sample turned into a partially water saturated

sample with an increase of gas saturation from the bottom to the top. For the simulation of hydrate deposits underlain with water (class II, according to the hydrate deposit classification of Moridis and Collett [2003]) this aspect constitutes a limitation because the flow patterns might become blurred as soon as the sediment sample turns water partially saturated. During the 2007/2008 Mallik (class II reservoir) field test some unconventional gas flow patterns were observed, which Wright et al. [2011a] suggested to originate from microbubble transport in the liquid phase. Even though flow patterns were identified in the LARS experiments which appeared very similar to the patterns observed in the 2007/2008 Mallik field test, the microbubble - hypothesis could neither be confirmed nor declined throughout the entire production experiment in LARS. Even if microbubble transport mechanisms affect the gas flow rate in the fully water saturated parts of the sample, the resulting effects might have become buffered in the gas saturated parts of the hydrate-free pore space.
I therefore suggest the performed production experiments to rather simulate class III hydrate deposits, which are characterized by the absence of an underlying zone of mobile fluids. However, the production of class III hydrate deposits is little studied and strongly depends on the effective permeability of the hydrate bearing layer. The absence of hydrate free (permeable) zones underneath or inside the hydrate bearing layer of class III deposits may reduce the attractiveness of depressurization [Moridis 2008]. In contrast, thermal stimulation is considered to be much more promising in class III deposits compared to other deposit classes [Moridis and Collett 2003]. Complementary to the performed dissociation experiments, studies using the counter-current heat-exchange reactor developed by Schicks et al. [2013] could provide a deeper understanding on the performance of gas production from class III deposits. The re-injection of produced water would allow to mimic class II deposits in LARS and to investigate the performance of depressurization, thermal stimulation, or a combination of both of them. The experimental setup LARS can therefore provide valuable data in order to understand the mechanisms for safe gas production from different classes of hydrate deposits.

6.2. Outlook

In collaboration with colleagues from the GEOMAR Helmholtz Centre for Ocean Research Kiel, Germany, we performed two experiments in LARS to investigate the feasibility and performance of CO_2 - CH_4 hydrate exchange reactions. To do so, a bulk CH_4 hydrate saturation of $S_H = 50\%$ was initially generated. The formed hydrate phase was predominantly distributed in the lower parts of the sediment sample. A channel of low hydrate saturation was left in the centre among massive hydrate blocks to maintain flow paths and avoid clogging of the sample (Fig. 6.4, left). Subsequently, liquid CO_2 was injected stepwise from the bottom of the specimen in 10 kg/day steps over 5 days. After ≈4h of continuous CO_2 injection, the pumps were stopped for ≈20h to give the exchange process time and to let the system equilibrate.
Because solid hydrates, gaseous CH_4, gaseous CO_2, and the injected liquid CO_2

constitute an electrical isolator, the ERT fails to identify the present phases inside the sediment sample. However, the increase of electrical resistivity caused by the injected CO_2 overprints the high resistivity areas due to hydrates in the pore space. Thus, monitoring the resistivity changes during the exchange experiment allows to follow the CO_2 migration front inside the sample (Fig. 6.4, right). First preliminary results suggest that the ERT results match other data sets like gas flow rates and gas chromatography very well as the moment of CO_2 breakthrough at the production site (top) are in good accordance with each other. Nevertheless, data processing is still under progress and a publication presenting the results of the CO_2 - CH_4 hydrate exchange experiments is currently in preparation.

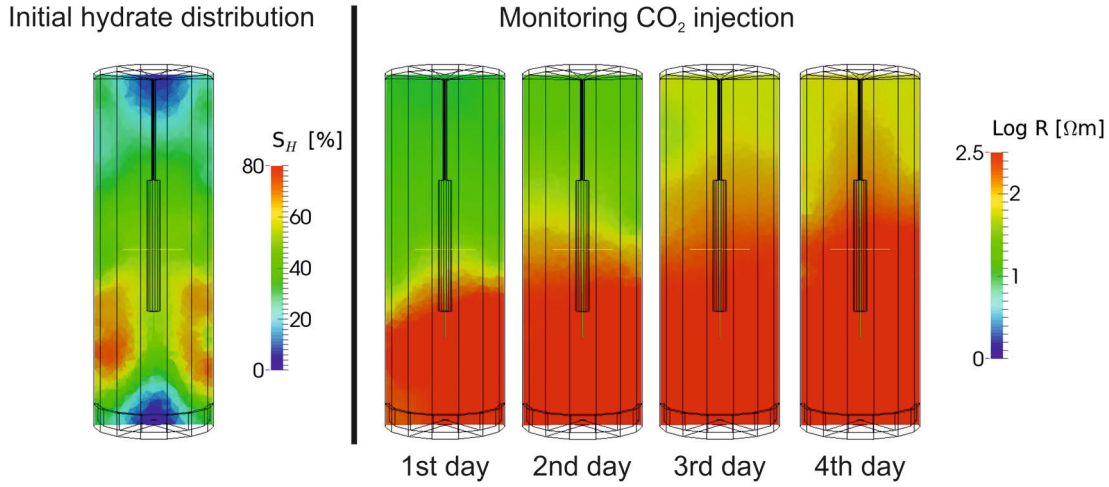

Figure 6.4.: ERT monitoring of CO_2 - CH_4 hydrate exchange reaction in LARS. A bulk hydrate saturation of $S_H = 50\%$ was generated prior to the CO_2 injection (left). The resistivity increase caused by the injected CO_2 overprints high resistivity areas due to hydrates in the pore space, allowing to follow the CO_2 migration front throughout the experiment (right).

The studies presented in chapter 3 demonstrated that the developed ERT array provides deep insights into the hydrate formation process in LARS. Not only the spatial distribution of formed hydrate could be monitored, but the local changes of hydrate saturation could get quantified as well. However, it was evident that the ERT array only provides a proper data basis during hydrate formation experiments. During hydrate dissociation experiments the ERT could only identify areas of elevated resistivity. Because gas hydrate, the released gas phase, and ice formed due to cooling as a result of hydrate decomposition constitute an electrical resistor, the ERT array failed to identify the present phases within the reservoir. Nevertheless, this kind of information would be very helpful in terms of getting in visual impression of the progress of hydrate decomposition as well as on the creation of specific flow paths for either gas or water. To solve this problem the next step is to add a seismic tomography array to the LARS setup. The contrast of the elastic properties of the present phases (Tab. 1.2) should allow to subsequently identify the present

phases within the sediment.

Due to the limited solubility of methane in water, the formation of pore filling hydrate from methane dissolved in water is a very slow process. Within the LARS setup hydrate formation rates of ≈2% per day were achieved. Because natural gas hydrate reservoirs can reach hydrate saturations up to S_H≈90% [Dallimore et al. 2005], laboratory hydrate synthesization from methane dissolved in water can last for several months until characteristic saturation stages are achieved.
We currently study an alternative approach to assess the dependencies of rock physical sediment properties on the pore filling hydrate saturation in a significantly quicker way. This approach bases on the generation of well defined pore filling ice fractions using H_2O-KCl-NaCl solutions of different salinities. Based on the data of Hall et al. [1988], who studied the freezing point depression of H_2O-NaCl-KCl solutions, it is possible to create a dependency of the generated ice fraction on the surrounding temperature for a given salinity. In a first proof-of-concept, Seyberth [2015] could show that measured seismic velocities for ice fractions formed from salt solutions correspond to velocities of non-cementing hydrate. Optionally, the formed ice fraction could finally get converted into methane hydrate using the technique of Stern et al. [1996].
To create a data baseline for the planned seismic tomography array and the ERT array in LARS, I currently investigate the changes of the seismic and electrical properties of the LARS sediment with respect to the formed ice fraction. Whereas the measured P-wave velocities follow the modelled velocity changes of pore filling hydrate for ice saturation values smaller ≈35%, the velocities suggest the solid phase to become load bearing for higher saturation values (Fig. 6.5). This is in good agreement with the studies of Spangenberg and Kulenkampff [2006] and Priest et al. [2009], who reported that pore filling hydrate transforms into frame building/load bearing hydrate for pore space saturations above 40%. Thus, the preliminary results suggest that the generation of defined ice fractions using the freezing point depression of H_2O-NaCl-KCl solutions constitutes a good proxy to non-cementing hydrate formed from methane dissolved in water. However, experiments and data processing are still under progress and a publication is currently in preparation.

To deepen the general understanding of lab-based hydrate formation from methane dissolved in water, further attention has to be paid to the altering and recrystallization processes mentioned in chapter 4. High resolution studies on artificially formed hydrates are required to properly understand to what extend the physical properties of hydrate bearing sediments are subjected to effects caused by recrystallization and how the crystallite sizes of artificially formed hydrates compare to those of naturally formed hydrates [Klapp et al. 2010]. Microscopic changes could be investigated using synchrotron radiation X-ray cryo-tomography microscopy (SRXCTM) which is reported to resolve the nucleation and growth of hydrate [Kuhs et al. 2014]. On a macroscopic scale the changes of physical properties could be resolved by monitoring e.g. the electrical resistivity over time to gain an impression on the extent and the kinetic of recrystallization.

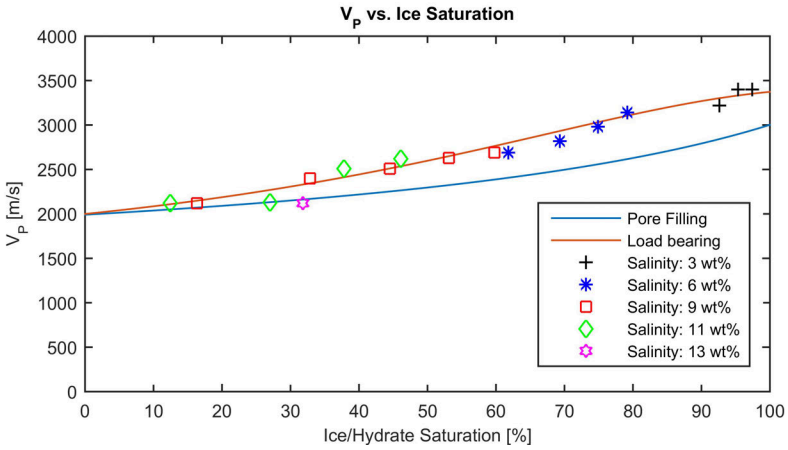

Figure 6.5.: Measured P-wave velocities vs. ice fractions formed from a set of KCl-H_2O solutions (symbols). Solid lines represent modelled data following the calculations of Dvorkin and Nur [1996] and Helgerud et al. [1999] for pore filling and load bearing hydrate, respectively.

Chapter 5 concluded that open questions remain in order to properly evaluate production rates of both water and gas during hydrate dissociation experiments. Even though it could be shown that valuable lessons can be learned from hydrate decomposition experiments in LARS, the applicability of the obtained results to field data can be improved. Producing water and gas over the entire area of the sediment's top lead to effects which not necessarily occur on a field scale (e.g. settlement of water in the bottom of the sediment, unrealistic migration of the hydrate decomposition front). To better mimic natural production scenarios it is therefore planned to install a model borehole into the top closure of LARS providing more realistic flow regimes within the sediment sample. Furthermore, efforts are required to properly balance the water and gas budgets. In order to evaluate the efficiency of different hydrate dissociation techniques it is of eminent importance to have accurate knowledge of the amounts of produced and remaining gas over time. This issue will be solved with improved production flow instrumentation attached to the new borehole.

References

Archie, G. E., 1942. The electrical resistivity log as an aid in determining some reservoir characteristics. Petroleum Transactions of AIME 146, 54–62.

Atanackovic, T., Guran, A., 2000. Theory of Elasticity for Scientists and Engineers. Birkhäuser.

Barrett, J., 2003. Inorganic Chemistry in Aqueous Solution. Tutorial chemistry texts. Royal Society of Chemistry.

Berndt, C., Bünz, S., Clayton, T., Mienert, J., Saunders, M., 2004. Seismic character of bottom simulating reflectors: examples from the mid-norwegian margin. Marine and Petroleum Geology 21 (6), 723 – 733.

Blanco, G., Gerlagh, R., Suh, S., Barrett, J., de Coninck, H., Morejon, C. D., Mathur, R., Nakicenovic, N., Ahenkora, A. O., Pan, J., Pathak, H., Rice, J., Richels, R., Smith, S., Stern, D., Toth, F., Zhou, P., 2014. Drivers, trends and mitigation. In: Edenhofer, O., Pichs-Madruga, R., Sokona, Y., Farahani, E., Kadner, S., Seyboth, K., Adler, A., Baum, I., Brunner, S., Eickemeier, P., Kriemann, B., Savolainen, J., Schlömer, S., von Stechow, C., Zwickel, T., Minx, J. (Eds.), Climate Change 2014: Mitigation of Climate Change. Contribution of Working Group III to the Fifth Assessment Report of the Intergovernmental Panel on Climate Change. Cambridge University Press, Cambridge, United Kingdom and New York, NY, USA.

Buffett, B., Zatsepina, O., 2000. Formation of gas hydrate from dissolved gas in natural porous media. Marine Geology 164 (1), 69 – 77.

Bünz, S., Mienert, J., Berndt, C., 2003. Geological controls on the storegga gas-hydrate system of the mid-norwegian continental margin. Earth and Planetary Science Letters 209 (3-4), 291 – 307.

Carman, P., 1956. Flow of Gases Through Porous Media. Academic Press.

Christiansen, R. L., Sloan, E. D., 1994. Mechanisms and kinetics of hydrate formation. Annals of the New York Academy of Sciences 715 (1), 283–305.

Dai, S., Santamarina, J. C., Waite, W. F., Kneafsey, T. J., 2012. Hydrate morphology: Physical properties of sands with patchy hydrate saturation. Journal of Geophysical Research: Solid Earth 117 (B11).

Dallimore, S., Yamamoto, K., Wright, J., Bellefleur, G., 2012. Scientific results from the JOGMEC/NRCan/Aurora mallik 2007-2008 gas hydrate production research well program, mackenzie delta, northwest territories, canada. In: Geological Survey of Canada, Bulletin 601.

Dallimore, S. R., et al., 2005. Scientific results from the Mallik 2002 gas hydrate production research well program, Mackenzie Delta, Northwest Territories, Canada. Geological Survey of Canada Ottawa, Ontario, Canada.

Demirbas, A., 2010. Methane Gas Hydrate. Green Energy and Technology. Springer London.

Du Frane, W. L., Stern, L. A., Weitemeyer, K. A., Constable, S., Roberts, J. J., 2011. Electrical properties of methane hydrate+ sediment mixtures. Fire in the Ice 11 (2), 10–13.

Dvorkin, J., Nur, A., 1996. Elasticity of high-porosity sandstones: Theory for two north sea data sets. GEOPHYSICS 61 (5), 1363–1370.

Faraday, M., 1859. Experimental Researches in Chemistry and Physics. R. Taylor and W. Francis.

Fricke, S., Schön, J., 1999. Praktische Bohrlochgeophysik. Enke im Georg Thieme Verlag.

Giavarini, C., Hester, K., 2011. Gas Hydrates: Immense Energy Potential and Environmental Challenges. Green Energy and Technology. Springer.

Guéguen, Y., Palciauskas, V., 1994. Introduction to the Physics of Rocks. Princeton University Press.

Hall, D. L., Sterner, S. M., Bodnar, R. J., 1988. Freezing point depression of nacl-kcl-h2o solutions. Economic Geology 83 (1), 197–202.

Hammerschmidt, E. G., 1934. Formation of gas hydrates in natural gas transmission lines. Industrial & Engineering Chemistry 26 (8), 851–855.

Hartmann, D., Tank, A. K., Rusticucci, M., Alexander, L., Brönnimann, S., Charabi, Y., Dentener, F., Dlugokencky, E., Easterling, D., Kaplan, A., Soden, B., Thorne, P., Wild, M., Zha, P., 2013. Observations: Atmosphere and surface. In: Stocker, T., Qin, D., Plattner, G.-K., Tignor, M., Allen, S., Boschung, J., Nauels, A., Xia, Y., Bex, V., Midgle, P. (Eds.), Climate Change 2013: The Physical Science Basis. Contribution of Working Group I to the Fifth Assessment Report of the Intergovernmental Panel on Climate Change. Cambridge University Press, Cambridge, United Kingdom and New York, NY, USA.

Heeschen, K., Schicks, J. M., Oeltzschner, G., 2014. The influence of sediment and fluid properties on methane hydrate formation. Proceedings of the 8th International Conference on Gas Hydrates ICGH 2014, T1–118.

Helgerud, M., Dvorkin, J., Nur, A., Sakai, A., Collett, T., 1999. Elastic-wave velocity in marine sediments with gas hydrates: Effective medium modeling. Geophysical Research Letters 26 (13), 2021–2024.

Helgerud, M. B., Waite, W. F., Kirby, S. H., Nur, A., 2009. Elastic wave speeds and moduli in polycrystalline ice ih, si methane hydrate, and sii methane-ethane hydrate. Journal of Geophysical Research: Solid Earth 114 (B2), B02212.

Hester, K. C., Brewer, P. G., 2009. Clathrate hydrates in nature. Annual Review of Marine Science 1 (1), 303–327, pMID: 21141039.

Kang, S.-P., Seo, Y., Jang, W., 2009. Kinetics of methane and carbon dioxide hydrate formation in silica gel pores. Energy & Fuels 23 (7), 3711–3715.

Kirsch, R., 2008. Groundwater Geophysics: A Tool for Hydrogeology. Springer Berlin Heidelberg.

Klapp, S. A., Hemes, S., Klein, H., Bohrmann, G., MacDonald, I., Kuhs, W. F., 2010. Grain size measurements of natural gas hydrates. Marine Geology 274 (1-4), 85 – 94.

Klapp, S. A., Klein, H., Kuhs, W. F., 2007. First determination of gas hydrate crystallite size distributions using high-energy synchrotron radiation. Geophysical Research Letters 34 (13), L13608.

Kleinberg, R. L., Flaum, C., Griffin, D. D., Brewer, P. G., Malby, G. E., Peltzer, E. T., Yesinowski, J. P., 2003. Deep sea nmr: Methane hydrate growth habit in porous media and its relationship to hydraulic permeability, deposit accumulation, and submarine slope stability. Journal of Geophysical Research: Solid Earth 108 (B10), 2508.

Koh, C. A., Sloan, E. D., Sum, A. K., Wu, D. T., 2011. Fundamentals and applications of gas hydrates. Annual Review of Chemical and Biomolecular Engineering 2 (1), 237–257, pMID: 22432618.

Kossel, E., Deusner, C., Bigalke, N., Haeckel, M., 2013. Magnetic resonance imaging of gas hydrate formation and conversion at sub-seafloor conditions. Diffusion Fundamentals 18 (15), 1–4.

Kuhs, W. F., Chaouachi, M., Falenty, A., Sell, K., Schwarz, J. O., Wolf, M., Enzmann, F., Kersten, M., Haberthüer, D., 2014. In-situ micro-structural studies of gas hydrate formation in sedimentary matrices. In: Proceedings of the 8th International Conference on Gas Hydrates (ICGH8-2014), Beijing, China, July 28-August 1,.

Kumar, A., Maini, B., Bishnoi, P., Clarke, M., Zatsepina, O., Srinivasan, S., 2010. Experimental determination of permeability in the presence of hydrates and its effect on the dissociation characteristics of gas hydrates in porous media. Journal of Petroleum Science and Engineering 70 (1-2), 114 – 122.

Kvamme, B., 1996. A new theory for the kinetics of hydrate formation. In: Proceedings of the Second International Conference on Natural Gas Hydrates, Toulouse, France. pp. 131–146.

Kvenvolden, K. A., 1993. Gas hydrates - geological perspective and global change. Reviews of Geophysics 31 (2), 173–187.

Kvenvolden, K. A., 1999. Potential effects of gas hydrate on human welfare. Proceedings of the National Academy of Sciences 96 (7), 3420–3426.

Lederhos, J., Long, J., Sum, A., Christiansen, R., Jr, E. S., 1996. Effective kinetic inhibitors for natural gas hydrates. Chemical Engineering Science 51 (8), 1221 – 1229.

Lee, W. S., White, M., 2014. Guest molecule exchange kinetics for the 2012 ignik sikumi gas hydrate field trial. In: Offshore Technology Conference.

Linga, P., Haligva, C., Nam, S. C., Ripmeester, J. A., Englezos, P., 2009. Gas hydrate formation in a variable volume bed of silica sand particles. Energy & Fuels 23 (11), 5496–5507.

Long, J., Sloan, E., 1996. Hydrates in the ocean and evidence for the location of hydrate formation. International Journal of Thermophysics 17 (1), 1–13.

Lowrie, W., 2007. Fundamentals of Geophysics. Cambridge University Press.

Luzi, M., 2012. Kinetic studies of mixed gas hydrates. Ph.D. thesis, Universität Potsdam.

Mak, T. C. W., McMullan, R. K., 1965. Polyhedral clathrate hydrates. x. structure of the double hydrate of tetrahydrofuran and hydrogen sulfide. The Journal of Chemical Physics 42 (8), 2732–2737.

Makholm, J. D., 2015. Regulation of natural gas in the united states, canada, and europe: Prospects for a low carbon fuel. Review of Environmental Economics and Policy 9 (1), 107–127.

Makogon, Y., 1966. Features of natural gas fields exploitation in permafrost zone. Gazovaya Promyshlennost 9, 1–17.

Mavko, G., Mukerji, T., Dvorkin, J., 2003. The Rock Physics Handbook: Tools for Seismic Analysis of Porous Media. Stanford-Cambridge Program. Cambridge University Press.

Max, M., Johnson, A., Dillon, W., 2006. Economic Geology of Natural Gas Hydrate. Coastal Systems and Continental Margins. Springer Netherlands.

McMullan, R. K., Jeffrey, G. A., 1965. Polyhedral clathrate hydrates. ix. structure of ethylene oxide hydrate. The Journal of Chemical Physics 42 (8), 2725–2732.

Mienert, J., Vanneste, M., Bünz, S., Andreassen, K., Haflidason, H., Sejrup, H. P., 2005. Ocean warming and gas hydrate stability on the mid-norwegian margin at the storegga slide. Marine and Petroleum Geology 22 (1-2), 233 – 244.

Milkov, A. V., 2004. Global estimates of hydrate-bound gas in marine sediments: how much is really out there? Earth-Science Reviews 66 (3 - 4), 183 – 197.

Milkov, A. V., Claypool, G. E., Lee, Y.-J., Sassen, R., 2005. Gas hydrate systems at hydrate ridge offshore oregon inferred from molecular and isotopic properties of hydrate-bound and void gases. Geochimica et Cosmochimica Acta 69 (4), 1007 – 1026.

Moridis, G., Collett, T., 2003. Strategies for gas production from hydrate accumulations under various geologic conditions. Lawrence Berkeley National Laboratory.

Moridis, G. J., 2008. Toward production from gas hydrates: current status, assessment of resources, and simulation-based evaluation of technology and potential. Lawrence Berkeley National Laboratory.

Piñero, E., Marquardt, M., Hensen, C., Haeckel, M., Wallmann, K., 2013. Estimation of the global inventory of methane hydrates in marine sediments using transfer functions. Biogeosciences 10 (2), 959–975.

Priegnitz, M., Thaler, J., Spangenberg, E., Rücker, C., Schicks, J. M., 2013. A cylindrical electrical resistivity tomography array for three-dimensional monitoring of hydrate formation and dissociation. Review of Scientific Instruments 84 (10), 104502.

Priegnitz, M., Thaler, J., Spangenberg, E., Schicks, J. M., Schrötter, J., Abendroth, S., 2015. Characterizing electrical properties and permeability changes of hydrate bearing sediments using ert data. Geophysical Journal International 202 (3), 1599–1612.

Priest, J. A., Rees, E. V. L., Clayton, C. R. I., 2009. Influence of gas hydrate morphology on the seismic velocities of sands. Journal of Geophysical Research 114.

Purkey, S. G., Johnson, G. C., 2010. Warming of global abyssal and deep southern ocean waters between the 1990s and 2000s: contributions to global heat and sea level rise budgets. Journal of Climate 23 (23), 6336–6351.

Rempel, A., Buffett, B., 1997. Formation and accumulation of gas hydrate in porous media. JOURNAL OF GEOPHYSICAL RESEARCH-ALL SERIES- 102, 10–151.

Ripmeester, J. A., John, S. T., Ratcliffe, C. I., Powell, B. M., 1987. A new clathrate hydrate structure. Nature 325 (6100), 135–136.

Schicks, J. M., Luzi-Helbing, M., 2015. Kinetic and thermodynamic aspects of clathrate hydrate nucleation and growth. Journal of Chemical & Engineering Data 60 (2), 269–277.

Schicks, J. M., Spangenberg, E., Giese, R., Luzi-Helbing, M., Priegnitz, M., Beeskow-Strauch, B., 2013. A counter-current heat-exchange reactor for the thermal stimulation of hydrate-bearing sediments. Energies 6 (6), 3002–3016.

Schicks, J. M., Spangenberg, E., Giese, R., Steinhauer, B., Klump, J., Luzi, M., 2011. New approaches for the production of hydrocarbons from hydrate bearing sediments. Energies 4 (1), 151–172.

Schön, J., 2004. Physical Properties of Rocks: Fundamentals and Principles of Petrophysics. Handbook of Geophysical Exploration: Seismic Exploration. Elsevier.

Schwalenberg, K., Haeckel, M., Poort, J., Jegen, M., 2010. Evaluation of gas hydrate deposits in an active seep area using marine controlled source electromagnetics: Results from opouawe bank, hikurangi margin, new zealand. Marine Geology 272 (1-4), 79 – 88, methane seeps at the Hikurangi Margin, New Zealand.

Schweizer, V., Grotzinger, J., Jordan, T., Press, F., Siever, R., 2007. Press/Siever - Allgemeine Geologie. Sav Geowissenschaften. Spektrum Akademischer Verlag.

Seyberth, K., 2015. Test einer neuen Methode zur Synthetisierung hydrathaltiger Sedimentproben und Charakterisierung des Hydrathabitus anhand seismischer Messungen. Bachelor thesis, Universität Potsdam, https://publishup.uni-potsdam.de/opus4-ubp/frontdoor/index/index/docId/8124.

Shankar, U., Riedel, M., 2011. Gas hydrate saturation in the krishna-godavari basin from p-wave velocity and electrical resistivity logs. Marine and Petroleum Geology 28 (10), 1768 – 1778.

Sloan, E., Koh, C., 2008. Clathrate Hydrates of Natural Gases. Chemical Industries. CRC Press.

Spangenberg, E., 2001. Modeling of the influence of gas hydrate content on the electrical properties of porous sediments. Journal of Geophysical Research: Solid Earth 106 (B4), 6535–6548.

Spangenberg, E., Kulenkampff, J., 2006. Influence of methane hydrate content on electrical sediment properties. Geophysical Research Letters 33.

Spangenberg, E., Kulenkampff, J., Naumann, R., Erzinger, J., 2005. Pore space hydrate formation in a glass bead sample from methane dissolved in water. Geophysical Research Letters 32 (24), L24301–L24303.

Stern, I., Kirky, S., Durham, W. B., 1996. Peculiarities of methane clathrate hydrate formation and solid-state deformation, including possible superheating of water ice. Science-AAAS-Weekly Paper Edition 273 (5283), 1843–1847.

Stern, J., 2014. International gas pricing in europe and asia: A crisis of fundamentals. Energy Policy 64 (0), 43 – 48.

Sun, S.-C., Liu, C.-L., Ye, Y.-G., Liu, Y.-F., 2014. Phase behavior of methane hydrate in silica sand. The Journal of Chemical Thermodynamics 69, 118 – 124.

Telford, W., Geldart, L., Sheriff, R., 1990. Applied Geophysics. Monograph series. Cambridge University Press.

Torres, M., Tréhu, A., Cespedes, N., Kastner, M., Wortmann, U., Kim, J.-H., Long, P., Malinverno, A., Pohlman, J., Riedel, M., Collett, T., 2008. Methane hydrate formation in turbidite sediments of northern cascadia, {IODP} expedition 311. Earth and Planetary Science Letters 271 (1), 170 – 180.

Trofimuk, A., Cherskiy, N., Tsarev, V., 1973. Accumulation of natural gases in zones of hydrate - formation in the hydrosphere. Doklady Akademii Nauk SSSR 212 (4), 931–934.

Tse, J. S., Powell, B. M., Sears, V. F., Handa, Y. P., 1993. The lattice dynamics of clathrate hydrates. an incoherent inelastic neutron scattering study. Chemical Physics Letters 215 (4), 383–387.

Uchida, T., Takeya, S., Chuvilin, E. M., Ohmura, R., Nagao, J., Yakushev, V. S., Istomin, V. A., Minagawa, H., Ebinuma, T., Narita, H., 2004. Decomposition of methane hydrates in sand, sandstone, clays, and glass beads. Journal of Geophysical Research: Solid Earth 109 (B5), B05206.

Von Stackelberg, M., Gotzen, O., Pietuchovsky, J., Wirtscher, O., Frühbuss, H., Meinhold, W., 1947. Struktur und Formel der Gashydrate. Fortschr. der Mineralogie 26, 122–124.

Waite, W. F., Santamarina, J. C., Cortes, D. D., Dugan, B., Espinoza, D. N., Germaine, J., Jang, J., Jung, J. W., Kneafsey, T. J., Shin, H., Soga, K., Winters, W. J., Yun, T.-S., 2009. Physical properties of hydrate-bearing sediments. Reviews of Geophysics 47 (4).

Waite, W. F., Spangenberg, E., 2013. Gas hydrate formation rates from dissolved-phase methane in porous laboratory specimens. Geophysical Research Letters 40 (16), 4310–4315.

Waite, W. F., Winters, W. J., Mason, D. H., 2004. Methane hydrate formation in partially water-saturated ottawa sand. American Mineralogist 89, 1202–1207.

Walsh, M. R., Hancock, S. H., Wilson, S. J., Patil, S. L., Moridis, G. J., Boswell, R., Collett, T. S., Koh, C. A., Sloan, E. D., 2009. Preliminary report on the commercial viability of gas production from natural gas hydrates. Energy Economics 31 (5), 815 – 823.

Weinberger, J. L., Brown, K. M., Long, P. E., 2005. Painting a picture of gas hydrate distribution with thermal images. Geophysical Research Letters 32 (4), L04609.

Wright, J., Uddin, M., Dallimore, S., Coombe, D., 2011a. Mechanisms of gas evolution and transport in a producing gas hydrate reservoir: an unconventional basis for successful history matching of observed production flow data. In: Proceedings of the 7th International Conference on Gas Hydrates (ICGH 2011), Edinburgh, Scotland, United Kingdom, July 17-21.

Wright, J. F., Uddin, M., Dallimore, S. R., Coombe, D., 2011b. Mechanisms of gas evolution and transport in a producing gas hydrate reservoir: An unconventional basis for successful history matching of observed production flow data. Proceedings of the 7th International Conference on Gas Hydrates ICGH 2011.

Xu, W., Ruppel, C., 1999. Predicting the occurrence, distribution, and evolution of methane gas hydrate in porous marine sediments. Journal of Geophysical Research: Solid Earth 104 (B3), 5081–5095.

Yamamoto, K., 2014. 2013 methane hydrate offshore production test in the eastern nankai trough; a milestone on the path to real energy resource. Proceedings of the 8th International Conference on Gas Hydrates ICGH 2014, T3–153.

A. Petrophysical background

This chapter intends to give an introduction on the most relevant petrophysical parameters stressed throughout this thesis.

A.1. Porosity and density

Porosity ϕ is defined as the fraction of rock volume V that is not occupied by solid matter [Guéguen and Palciauskas 1994] and can be expressed as:

$$\phi = \frac{V - V_m}{V} = \frac{V_p}{V} \tag{A.1}$$

where

ϕ - porosity

V - bulk/total volume

V_m - volume of solid material/matrix

V_p - pore volume.

Pores are local enlargements in a pore-space system that provides most of the volume available for fluid storage. Pore throats are the smaller connecting spaces linking pores and providing the more significant restrictions to fluid flow [Schön 2004]. However, one can observe two materials with identical porosities but to have completely different physical properties. Thus, the definition given in equation A.1 is not sufficient to describe the pore-space system of a material in practical terms. Subsequently, additional definitions of porosity are required:

Total porosity ϕ — As defined in equation A.1, the total porosity is related to the entire pore-space of the rock.

Interconnected porosity ϕ_{con} — Single pores can be isolated within the rock matrix or connected. The interconnected porosity only relates to pores which are connected to each other. Those pores constitute the basic requirement to permit fluid flow in rocks. It is:

$$\phi_{\text{con}} \leq \phi \tag{A.2}$$

Effective porosity ϕ_{eff}

The effective porosity is only related to the pore space which gives fluid the possibility to flow. Because the interconnected porosity can contain significant values of dead-end pores, which do not contribute to fluid flow, isolated and dead-end pores are not included in the effective porosity. It is:

$$\phi_{\text{eff}} \leq \phi_{\text{con}} \leq \phi \tag{A.3}$$

Those different kinds of porosity are the reason why materials of identical porosities can display significant differences in their physical properties.

The density ρ is defined as the quotient of the mass m and the volume V of a material [Schön 2004]:

$$\rho = \frac{m}{V} \tag{A.4}$$

Both porosity and density are strongly linked to each other, thus porosity can be expressed as:

$$\phi = \frac{\rho_m - \rho}{\rho_m - \rho_{fl}} \tag{A.5}$$

where

ρ_m - matrix density, only considering the solid components

ρ_{fl} - mean density of the pore filling fluids.

A.2. Electrical properties

The electrical properties are a common tool to classify rocks and sedimentary bodies. The electrical resistivity ρ and its inverse the electrical conductivity σ are quantities which are frequently used to characterize charge transport [Guéguen and Palciauskas 1994; Schön 2004].
The basis of electrical measurements in geophysics is given by Ohm's law. When a static electric field E is applied to an isotropic material, an electric current density J is established due to charge transport following the linear relation [Guéguen and Palciauskas 1994]:

$$J = \sigma E = \frac{1}{\rho} E \tag{A.6}$$

where

σ - electric conductivity

ρ - electrical resistivity of the material.

The electric resistivity ρ of the material is linked to the electrical resistance R. The electrical resistance depends on geometry and is given by:

$$R = \rho \frac{l}{A} \tag{A.7}$$

where

R - electric resistance

l - length of the conductor

A - cross sectional area of the conductor.

Furthermore, the electrical resistance R is defined by the ratio of applied potential to the resulting electrical current:

$$R = \frac{U}{I} \tag{A.8}$$

where

U - electric potential

I - electric current.

Combining equation A.8 and A.7 and rearranging it for ρ_s yields:

$$\rho_s = \frac{U}{I} \frac{A}{l} \tag{A.9}$$

It is important to realize that this equation is exclusively valid for cylindrical conductors. In this particular case the length l and the cross sectional area A are sufficient to describe the geometry of the conductor. Because in geophysics usually bodies of a more complex geometry are investigated, the more general geometry factor is introduced in equation A.9:

$$\rho_s = K \cdot R = K \frac{U}{I} \tag{A.10}$$

where

K - geometry factor.

Equation A.10 already presents the main principle of geo-electrical measurements on both field and lab scale: Two electrodes are used to inject an electrical current

I into a geological body and two electrodes are used to measure the corresponding potential difference U. The actual number of the electrodes and the respective geometry factor K hereby depend on the electrode layout.
For electrical conduction in rocks and minerals three different types of conduction are important [Guéguen and Palciauskas 1994; Lowrie 2007]:

electronical conduction — The charge transport is provided by free electrons following Ohm's law.

dielectrical conduction — Electric current propagation in isolators or very low conductive materials containing no free electrons.

electrolytical conduction — Ions in the water (electrolyte water) filling the pore space are the charge carriers.

Most rock forming minerals have very high resistivities ($< 10^9\ \Omega m$) and are classed as insulators [Schön 2004]. Thus, charge transport in natural sediments and rocks is predominantly provided by conductive pore water and a result of electrolytical conduction. The conductivity of the pore water mainly depends on ion concentration, ion mobility, ion charge number, and temperature.
For most geoelectrical applications detailed information on the pore microstructure are not present. For that reason, one usually relies on empirical relations. In 1942 Archie [1942] suggested that the resistivity of a water saturated rock is proportional to the water resistivity [Schön 2004], which lead to the expression:

$$\rho_0 = F \cdot \rho_w \tag{A.11}$$

where

ρ_0 - electrical resistivity of the water saturated rock

F - formation resistivity factor

ρ_w - electrical resistivity of the pore water.

The formation resistivity factor F thus links the electrical properties of the rock and the pore fill. In addition, F contains information on the pore space as it correlates with the porosity:

$$F = \frac{a}{\phi^m} \tag{A.12}$$

where

ϕ - porosity

a, m - empirical parameter.

Combining equations A.11 and A.12 yields the frequently used 1st Archie equation:

$$\rho_0 = \frac{a \cdot \rho_w}{\phi^m} \tag{A.13}$$

However, equations A.11 - A.13 are valid for scenarios featuring a fully water saturated pore space. In the case of partial water saturation, the degree of water saturation S_w has to be considered. The resulting relation is commonly referred to as the 2nd Archie equation:

$$\rho_t = \frac{a}{\phi^m S_w^n} \rho_w \tag{A.14}$$

where

ρ_t - true resistivity of the rock with saturation S_w

S_w - degree of fluid saturation

n - empirical parameter.

The parameters a and m are the fitting parameters which originate from relating the formation resistivity factor F with the porosity ϕ. The empirical parameter m as the porosity exponent can be understood as a weighting of the porosity. This parameter is mainly controlled by the pore space geometry and interconnectivity. Originally, values for m were thought to increase with increasing grain cementation which is the reason why m is sometimes also referred to as cementation factor. Commonly used values for unconsolidated sediments are $a \approx 1$ and m=1.3 - 1.4 [Fricke and Schön 1999]. The parameter n is frequently referred to as saturation exponent. Even though Spangenberg [2001] showed that values for n can vary from 0.5 to 4, a mean value of $n \approx 2$ is frequently used [Fricke and Schön 1999].
It is Archie's equations that are commonly used in petrophysics for well log interpretation in order to evaluate porosity or pore fill quantities.

A.3. Theory of elasticity and seismic velocities

The theory of elasticity is the fundamental basis for the description of elastic wave propagation [Schön 2004]. The basic parameters are stress σ and strain ϵ. Stress is the force per unit area that is applied to a body [Telford et al. 1990]. When an elastic body is subjected to stresses, changes is shape and dimensions will occur. These changes are called strains [Telford et al. 1990].

$$\sigma = \frac{F}{A} \qquad\qquad \varepsilon = \frac{\Delta l}{l} \tag{A.15}$$

where

σ - stress

F - applied force

A - area

ε - strain

Δl - change of shape

l - original shape.

For infinitesimal small deformations and a linear stress-strain relation, stress and strain can be related for ideal elastic three dimensional bodies using Hooke's Law:

$$\sigma_{ij} = C_{ijkl}\varepsilon_{kl} \tag{A.16}$$

where

i, j, k, l - x, y, z coordinates.

The proportionality factor C_{ijkl} introduced in equation A.16 provides a direct link of strain to stress. Mathematically spoken it is a tensor of rank four containing 81 components which is composed by the elastic moduli. However, assuming symmetry of stress and strain and the elastic body to be isotropic, the number of elastic constants in C_{ijkl} gets reduced to two (one specific strain results from one specific stress). To describe this dependence the two Lamé constants λ and μ are introduced, reducing the complexity of C_{ijkl} to [Atanackovic and Guran 2000]:

$$C_{ijkl} = \begin{bmatrix} \lambda+2\mu & \lambda & \lambda & 0 & 0 & 0 \\ \lambda & \lambda+2\mu & \lambda & 0 & 0 & 0 \\ \lambda & \lambda & \lambda+2\mu & 0 & 0 & 0 \\ 0 & 0 & 0 & \mu & 0 & 0 \\ 0 & 0 & 0 & 0 & \mu & 0 \\ 0 & 0 & 0 & 0 & 0 & \mu \end{bmatrix} \tag{A.17}$$

where

λ, μ - Lamé constants.

Introducing A.17 in A.16 yields:

$$\sigma_{ij} = \lambda\theta\delta_{ij} + 2\mu\varepsilon_{ij} \tag{A.18}$$

where

θ - $\sum_i \varepsilon_{\mathrm{ij}}$

$\delta_{\mathrm{ij}} - \begin{cases} 1, & \text{if } i = j \\ 0, & \text{if } i \neq j \end{cases}$

To find an expression for the corresponding strain, equation A.18 is rearranged to:

$$\varepsilon_{\mathrm{ij}} = \frac{\sigma_{\mathrm{ij}}}{2\mu} - \frac{\lambda\theta\delta_{\mathrm{ij}}}{2\mu(3\lambda + 2\mu)} \tag{A.19}$$

Typically one dimensional ratios of stress and strain ($ij = kl$) are considered[1]. In that case C_{ijkl} in equation A.16 equals the Young's modulus E (also referred to as modulus of elasticity):

$$C_{\mathrm{ijkl}} = \frac{\sigma_{\mathrm{ij}}}{\varepsilon_{\mathrm{kl}}} = \frac{\sigma_{11}}{\varepsilon_{11}} = \frac{\mu(3\lambda + 2\mu)}{\lambda + \mu} = E \tag{A.20}$$

where

E - Young's modulus.

However, two different states of stress can be distinguished [Guéguen and Palciauskas 1994]:

hydrostatic compression

Stress is applied equally from all directions ($\sigma_x = \sigma_y = \sigma_z = -p$) and the change of volume $\frac{\Delta V}{V} = \varepsilon_{\mathrm{ij}}$ is considered.

$$\sigma_{\mathrm{ij}} = \begin{bmatrix} -p & 0 & 0 \\ 0 & -p & 0 \\ 0 & 0 & -p \end{bmatrix} \qquad \frac{|\sigma|}{3} = -p \tag{A.21}$$

where

p - hydrostatic pressure.

According to equation A.19 and A.20, the modulus of elasticity thus becomes:

$$C_{\mathrm{ijkl}} = \frac{\sigma_{\mathrm{ij}}}{\varepsilon_{\mathrm{ij}}} = \lambda + \frac{2}{3}\mu = K \tag{A.22}$$

where

[1] It is convention to indicate the spatial direction of the biggest stress with 11. Hence, one dimensional stress and strain imply $\sigma_{22} = \sigma_{33} = 0$.

K - bulk modulus.

Hence, the bulk modulus K yields information about how much hydrostatic pressure is needed to obtain a specific change of volume.

shear deformation

The applied stress causes a shear deformation and the modulus of elasticity E becomes the shear modulus μ with

$$C_{\mathrm{ijkl}} = 2\mu \qquad \varepsilon_{\mathrm{ij}} = \frac{\sigma_{\mathrm{ij}}}{2\mu} \tag{A.23}$$

where

μ - shear modulus.

As direct result of stress and strain, particle motion will occur in a solid body. This particle motion is described with the one dimensional general dynamic equilibrium equation of motion [Lowrie 2007]:

$$\frac{\delta\sigma_{xx}}{\delta x} = \rho\frac{\delta^2 u_x}{\delta t^2} \tag{A.24}$$

where

$\frac{\delta\sigma_{xx}}{\delta x}$ - stress variation in x-direction

ρ - density of the body

$\frac{\delta^2 u_x}{\delta t^2}$ - particle acceleration.

For longitudinal (compressional) body waves particle motion occurs as a series of dilatations and compressions. In that particular case equation A.24 becomes:

$$\frac{\delta^2 u}{\delta t^2} = V_p^2\frac{\delta^2 u}{\delta x^2} \tag{A.25}$$

where

V_p - velocity of a compressional wave.

Rearranging equation A.25 for V_p yields the equation of the P-wave velocity:

$$V_p = \sqrt{\frac{\lambda + 2\mu}{\rho}} = \sqrt{\frac{K + \frac{4}{3}\mu}{\rho}} \tag{A.26}$$

For shear waves the particle motion is parallel to the wave front and transverse to the direction of propagation. For shear waves equation A.24 has to be adjusted and becomes [Lowrie 2007]:

$$\frac{\delta \sigma_{xz}}{\delta x} = \rho \frac{\delta^2 u_x}{\delta t^2} \tag{A.27}$$

Subsequently on finds for the shear wave velocity:

$$V_s = \sqrt{\frac{\mu}{\rho}} \tag{A.28}$$

where

V_s - velocity of a shear wave.

A.4. Permeability

The permeability characterizes the ability of a material to allow fluids to flow. Detailed knowledge of a rock's permeability is of eminent importance in order to evaluate any potential or proven reservoir rock. The permeability mainly depends on effective porosity, pore space geometry, and is generally a tensor [Schön 2004]. Laminar fluid of a viscous fluid through a porous medium is defined according to Darcy's law:

$$u = -\frac{k}{\eta} \cdot \nabla p \tag{A.29}$$

where

u - volume flow density

k - permeability

η - dynamic viscosity

∇p - fluid pressure gradient.

The volume flow density u can also be expressed as the flow rate per cross section area. Rearranging equation A.29 thus yields for the permeability:

$$k = -\frac{\eta \cdot Q}{\nabla p \cdot A} \tag{A.30}$$

where

Q - flow rate

A - cross section area.

The definition of the permeability given in equation A.30 describes the laminar flow of an incompressible viscous fluid and is valid for isotropic porous media.

Nomenclature

η	dynamic viscosity	[$\frac{kg}{m \cdot s}$]
λ, μ	Lamé constants	
μ	shear modulus	[Pa]
ϕ	porosity	[-]
ρ	density	[$\frac{kg}{m^3}$]
ρ	electrical resistivity	[Ωm]
σ	electric conductivity	[$\frac{S}{m}$]
σ	stress	[Pa]
ε	strain	[-]
A	area	[m^2]
E	Young's modulus	[Pa]
E	electric field strength	[$\frac{V}{m}$]
F	applied force	[N]
F	formation resistivity factor	[-]
I	electric current	[A]
J	electric current density	[$\frac{A}{m^2}$]
K	bulk modulus	[Pa]
K	geometry factor	[m]
k	permeability	[$D = 10^{12} m^2$]

l	length	[m]
m	mass	[kg]
R	electric resistance	[Ω]
S	degree of saturation	[-]
U	electric potential	[V]
V	volume	[m^3]
$V_{p/s}$	P-/S-wave velocity	[$\frac{m}{s}$]